NASA/TP–2018–220105

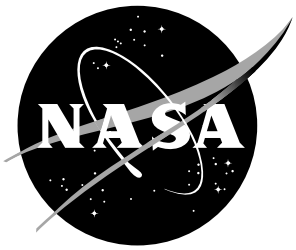

Modeling Fiber Kinking at the Microscale and Mesoscale

Miguel Herráez
IMDEA Materials, and Universidad Politécnica de Madrid, Madrid, Spain

Andrew C. Bergan
Langley Research Center, Hampton, Virginia

Carlos González
IMDEA Materials, and Universidad Politécnica de Madrid, Madrid, Spain

Claudio S. Lopes
IMDEA Materials, Madrid, Spain

October 2018

NASA STI Program. . . in Profile

Since its founding, NASA has been dedicated to the advancement of aeronautics and space science. The NASA scientific and technical information (STI) program plays a key part in helping NASA maintain this important role.

The NASA STI Program operates under the auspices of the Agency Chief Information Officer. It collects, organizes, provides for archiving, and disseminates NASA's STI. The NASA STI Program provides access to the NASA Aeronautics and Space Database and its public interface, the NASA Technical Report Server, thus providing one of the largest collection of aeronautical and space science STI in the world. Results are published in both non-NASA channels and by NASA in the NASA STI Report Series, which includes the following report types:

- TECHNICAL PUBLICATION. Reports of completed research or a major significant phase of research that present the results of NASA programs and include extensive data or theoretical analysis. Includes compilations of significant scientific and technical data and information deemed to be of continuing reference value. NASA counterpart of peer-reviewed formal professional papers, but having less stringent limitations on manuscript length and extent of graphic presentations.
- TECHNICAL MEMORANDUM. Scientific and technical findings that are preliminary or of specialized interest, e.g., quick release reports, working papers, and bibliographies that contain minimal annotation. Does not contain extensive analysis.
- CONTRACTOR REPORT. Scientific and technical findings by NASA-sponsored contractors and grantees.
- CONFERENCE PUBLICATION. Collected papers from scientific and technical conferences, symposia, seminars, or other meetings sponsored or co-sponsored by NASA.
- SPECIAL PUBLICATION. Scientific, technical, or historical information from NASA programs, projects, and missions, often concerned with subjects having substantial public interest.
- TECHNICAL TRANSLATION. English-language translations of foreign scientific and technical material pertinent to NASA's mission.

Specialized services also include organizing and publishing research results, distributing specialized research announcements and feeds, providing information desk and personal search support, and enabling data exchange services.

For more information about the NASA STI Program, see the following:

- Access the NASA STI program home page at `http://www.sti.nasa.gov`
- E-mail your question to `help@sti.nasa.gov`
- Phone the NASA STI Information Desk at 757-864-9658
- Write to:
  NASA STI Information Desk
  Mail Stop 148
  NASA Langley Research Center
  Hampton, VA 23681-2199

NASA/TP–2018–220105

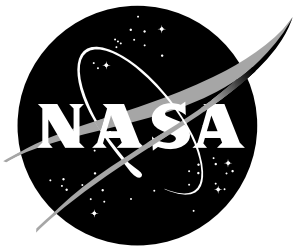

Modeling Fiber Kinking at the Microscale and Mesoscale

Miguel Herráez
IMDEA Materials, and Universidad Politécnica de Madrid, Madrid, Spain

Andrew C. Bergan
Langley Research Center, Hampton, Virginia

Carlos González
IMDEA Materials, and Universidad Politécnica de Madrid, Madrid, Spain

Claudio S. Lopes
IMDEA Materials, Madrid, Spain

National Aeronautics and
Space Administration

Langley Research Center
Hampton, Virginia 23681-2199

October 2018

Acknowledgments

The authors are grateful for the support provided by the Advanced Composites Project and the helpful comments from Frank Leone, Cheryl Rose, and Carlos Dávila of NASA Langley Research Center. M. Herráez acknowledges the financial support from IMDEA Materials for his three months stay at NASA Langley Research Center.

Available from:

NASA STI Program / Mail Stop 148
NASA Langley Research Center
Hampton, VA 23681-2199
Fax: 757-864-6500

Abstract

A computational micromechanics (CMM) model is employed to interrogate the assumptions of a recently developed mesoscale continuum damage mechanics (CDM) model for fiber kinking. The CMM model considers an individually discretized three dimensional fiber and surrounding matrix accounting for nonlinearity in the fiber, matrix plasticity, fiber/matrix interface debonding, and geometric nonlinearity. Key parameters of the CMM model were measured through experiments. In particular, a novel experimental technique to characterize the *in situ* longitudinal compressive strength of carbon fibers through indentation of micropillars is presented. The CDM model is formulated on the basis of Budiansky's fiber kinking theory (FKT) with a constitutive deformation-decomposition approach to alleviate mesh size sensitivity. In contrast to conventional mesoscale CDM models that prescribe a constitutive response directly, the response of the proposed model is an outcome of material nonlinearity and large rotations of the fiber direction following FKT. Comparison of the predictions from the CMM and CDM models shows remarkable correlation in strength, post-peak residual stress, and fiber rotation, with less than 10% difference between the two models in most cases. Additional comparisons are made with several fiber kinking models proposed in the literature to highlight the efficacy of the two models. Finally, the CMM model is exercised in parametric studies to explore opportunities to improve the longitudinal compression strength of a ply through the use of nonconventional microstructures.

List of Symbols

In general, the superscripts ^{f}, ^{m}, ^{c} are referred to quantities of the fiber, matrix, and fiber/matrix cohesive interface respectively. Whereas the subscripts $_{t}$, $_{c}$ indicate tensile and compressive quantities.

A^f	Cross sectional area of a fiber
b	Transverse length of fiber misalignment in a ply
c^f	Nonlinear parameter of the longitudinal elastic modulus, fiber
c^l	Nonlinear parameter of the longitudinal elastic modulus, ply
$\boldsymbol{C}$	Elastic stiffness tensor
$\mathbf{C}_T$	Tangent constitutive tensor
d	Fiber diameter
d_p	Micropillar diameter
d^v	Diameter of the channels or "islands" of hollow fibers
D	Damage variable for failure of the fiber
$\hat{\mathbf{e}}_f,\ \hat{\mathbf{e}}_n,\ \hat{\mathbf{e}}_t$	Unit vector for the current directions in the fiber-aligned reference frame
E_1^*	Longitudinal elastic modulus of the ply (nonlinear model)
E_1^{0f}	Initial longitudinal elastic modulus of the fiber for the nonlinear model
$E_1,\ E_2,\ E_3$	Elastic moduli of the ply
E^f	Elastic modulus of the fiber
$E_1^f,\ E_2^f$	Longitudinal and transverse elastic moduli of the fiber
E^m	Elastic modulus of the matrix
$\boldsymbol{E}$	Green-Lagrange strain tensor
f_{CL}	Constitutive law relating shear strain to shear stress
$F_{1+},\ F_{1-}$	Damage activation functions under longitudinal tension and compression
F_{TOL}	Maximum change in volume allowed
$\boldsymbol{F}$	Deformation gradient
$\boldsymbol{F_{\mathbf{kb}}}$	Deformation gradient for the kink band region
$\boldsymbol{F_m}$	Deformation gradient for the undamaged material region
$G_{12},\ G_{13},\ G_{23}$	Shear moduli of the ply
$G_{12}^f,\ G_{23}^f$	Longitudinal and transverse shear moduli of the fiber
$G_t^f,\ G_c^f$	Fracture energy of the fiber under longitudinal tension and compression
G^m	Shear modulus of the matrix
G_{2D}^m	Equivalent shear modulus in a 2-D micromechanical model
G_t^m	Fracture energy of the matrix under uniaxial tension
$G_n^c,\ G_s^c$	Interface Fracture energies for modes I and II
h_p	Micropillar height
$\boldsymbol{H}$	Compliance tensor of a ply
$\boldsymbol{I}$	Identity tensor
I_x^f	Second moment of inertia of the cross section of the fiber
I_x^{f0}	Second moment of inertia of the cross section of a circular fiber
k_0	Linear elastic stiffness during the micropillar compression test
$k_n^c,\ k_s^c$	Penalty stiffness in the normal and shear directions of the interface
$l_1,\ l_2,\ l_3$	Element edge lengths
L	Length of the fiber

$\mathbf{M}$	Damage evolution tensor
n_{NR}	Number of Newton-Raphson iterations
$n_{\max}$	Maximum number of Newton-Raphson iterations allowed
N^c	Normal tensile strength of the interface
$r_{1+},\ r_{1-}$	Elastic domain thresholds under longitudinal tension and compression
$\boldsymbol{R}$	Current misaligned reference frame
$\boldsymbol{R}_{\varphi_0}$	Rotation matrix for the initial fiber misalignment
$\boldsymbol{S}$	Second Piola-Kirchoff stress tensor
$\boldsymbol{S}'$	Second Piola-Kirchoff stress tensor in the fiber-aligned reference frame
S^c	Shear strength of the interface
$\mathbf{S}^f$	Compliance tensor of the fiber
$t_n,\ t_s,\ t_t$	Components of the traction vector
$\boldsymbol{t}_{\mathrm{kb}}$	Stress vector in the kink band region
$\boldsymbol{t}_{\mathrm{m}}$	Stress vector in the undamaged material region
t^m	Thickness of the matrix in a 2-D micromechanical model
$\boldsymbol{t}_{\mathrm{res}}$	Stress vector defining the residual to be minimized
u	Displacement
V^f	Fiber volume fraction
V^f_{2D}	Equivalent fiber volume fraction in a 2-D micromechanical model
V^m	Matrix volume fraction
V^v	Void volume fraction
w_{kb}	Width of the kink band
$\bar{w}_{\mathrm{kb}}$	Relative kink band size
x	Through-the-thickness direction
$x_1,\ x_2$	Longitudinal and transverse direction of a ply
$\boldsymbol{x}$	Current configuration
$\boldsymbol{x_{\mathrm{kb}}}$	Current configuration of the kink band region
$\boldsymbol{x_m}$	Current configuration of the undamaged material region
$\boldsymbol{X}$	Reference frame
$\boldsymbol{X}'$	Fiber-aligned reference frame
X_c	Compressive strength of a ply
$X^f_t,\ X^f_c$	Strength of the fiber under longitudinal tension and compression
y	Transverse direction
y_0	Initial transverse imperfection
$\bar{y}_0$	Parameter that defines the initial imperfection of the fiber
z	Longitudinal direction (parallel to the fibers)
α	Material parameter of a Ramberg-Osgood nonlinear curve
α^f_1	Coefficient of thermal expansion of the fiber in the longitudinal direction
α^f_2	Coefficient of thermal expansion of the fiber in the transverse direction
α^m	Coefficient of thermal expansion of the matrix
α_R	Coefficient of Rayleigh damping
β	Kink band inclination
γ	Shear strain
γ_{12}	Shear strain in the 1-2 plane
$\gamma^{EL}_{12},\ \gamma^{PL}_{12}$	Elastic and plastic shear strains in the 1-2 plane

γ^C	Critical shear strain
γ_Y	Shear yield strain
γ_{TOL}	Maximum shear strain allowed
ΔT	Change in temperature
$\Delta\varepsilon$	Strain increment tensor
ε	Strain tensor
$\dot{\varepsilon}$	Strain rate
ε_c	Compressive strain
η	Material parameter of a Ramberg-Osgood nonlinear curve
η_{BK}	Benzeggagh-Kenane mode-mixity parameter
θ_p	Taper angle of the micropillar
$\nu_{12},\ \nu_{13},\ \nu_{23}$	Poisson ratios of the ply
$\nu_{12}^f,\ \nu_{23}^f$	Longitudinal and transverse Poisson ratios of the fiber
ν^m	Poisson ratio of the matrix
ξ^c	Friction coefficient of the fiber/matrix interface
ρ	Density
$\tilde{\rho}$	Apparent density of hollow fiber composite
σ	Nominal stress tensor
$\tilde{\sigma}$	Effective stress tensor
σ_c	Compressive stress
σ_f	Stress in the fiber
σ_r	Residual crushing stress during fiber kinking
$\sigma_{t_0}^m$	Uniaxial tensile strength of the matrix
$\sigma_{c_0}^m$	Uniaxial compressive yield strength of the matrix
$\sigma_{c_u}^m$	Uniaxial ultimate compressive strength of the matrix
$\boldsymbol{\sigma}$	Cauchy stress tensor
$\boldsymbol{\sigma}_{\text{m}}$	Cauchy stress tensor in the undamaged material region
$\boldsymbol{\sigma}_{\text{kb}}$	Cauchy stress tensor in the kink band region
τ	Shear stress
τ_Y	Shear yield limit of a perfectly-plastic constitutive model
τ_{Y_m}	Shear yield limit of the matrix
τ_L	Shear stress at large fiber rotations
τ_u	Material parameter of a hyperbolic tangent nonlinear curve
τ_μ	Frictional shear stress
$\phi_{1+},\ \phi_{1-}$	Loading functions under longitudinal tension and compression
φ	Fiber rotation
φ_0	Initial fiber misalignment
φ_c	Critical initial fiber misalignment
$\tilde{\varphi}_0$	Standard deviation of the initial fiber misalignment distribution in a ply
$\varphi^{\max}$	Maximum fiber rotation, micromechanical model
φ^{avg}	Average fiber rotation, micromechanical model
φ_{ff}	Angle of fibers at fiber fracture
φ_k	Angle of kinked fibers
χ	Dimensionless constant that characterizes the compressive strength
ψ^m	Dilation angle of the matrix

$^\top$	Transpose operator

Abbreviations:

CDM	Continuum damage mechanics
CFRP	Carbon fiber reinforced plastic
CMM	Computational micromechanics
DGD	Deformation gradient decomposition
EPP	Elastic-perfectly plastic
FE	Finite element
FIB	Focused ion beam
FKT	Fiber kinking theory
PBC	Periodic boundary conditions
RVE	Representative volume element
SEM	Scanning electron microscopy
SFT	Single fiber test
VUMAT	Abaqus/Explicit user-defined material subroutine

1 Introduction

Fiber-reinforced polymers are often used in structural applications where high specific stiffness and strength properties are required. One of the main drawbacks of these materials is their complex mechanical behavior, due to their anisotropy and heterogeneity. At the same time, their high degree of customization makes their experimental characterization very costly. As such, computational mechanics appears as a promising tool to predict the structural response to complement experimental characterization.

The strong anisotropy and heterogeneity of unidirectional fiber-reinforced composites lead to very different failure mechanisms depending on the load state. In this work, the fiber kinking phenomenon, which is the primary failure mechanism when the fibers are loaded under longitudinal compression, is considered [1]. Numerous examples of the fiber kinking mechanism are found in the literature, e.g. [2–7]. Fiber kinking takes place in most high fiber volume fraction composite materials. As compressive stress, σ_c, increases, fibers rotate and the matrix undergoes shear deformation. At some load level, the matrix cannot support the shear stress, and the system becomes unstable and there is a drop in load. This shear instability is translated into a localized shear band (i.e. kink band) with fibers misaligned by an angle $\varphi = \varphi_0 + \gamma$ where φ_0 represents the initial misalignment and γ is the shear strain. The kink band has a width w_{kb} and propagates along the specimen at an angle, β, as shown in Fig. 1a. After the sudden drop of load, there is a plateau in stress at a residual stress level, σ_r, as shown in Fig. 1b for large compressive strains, ε_c. During this segment of the response, the kink band first propagates normal to the fiber direction (crack-like) and then under certain conditions grows wider in the fiber direction. The widening of the kink band along the fibers is referred to as band broadening [8, 9]. Typically carbon fibers break at the regions of highest bending stresses forming the characteristic kink bands observed postmortem.

Several reviews of analytical, numerical, and experimental investigations into fiber kinking are available in the literature [1, 6, 10, 11]. As such, only a few of the works most relevant to this report are reviewed here. The selected works that are discussed in the following review are relevant in that they are foundational to the models and approaches discussed herein or they are applied and compared in Section 4. A brief review of analytical models, finite element based mesoscale models, and finite element based micromechanical models are given in the following three sections, respectively. Following the review, the objective and outline of the present report are provided.

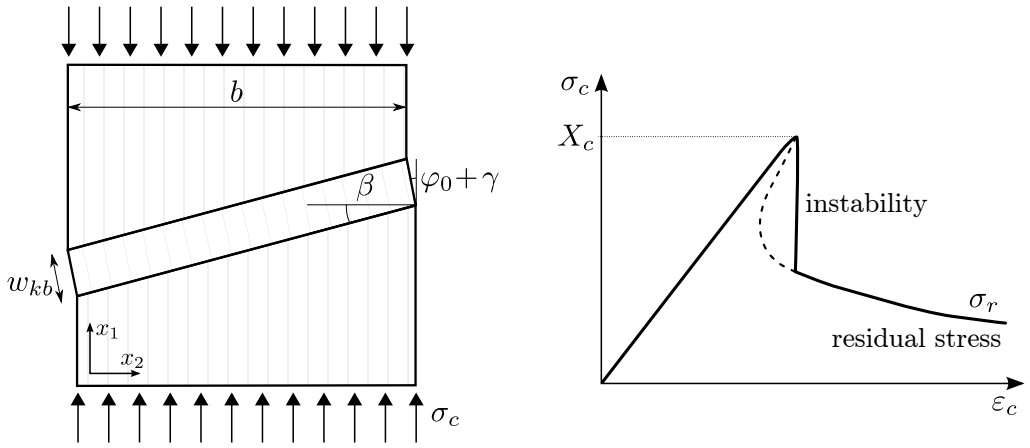

(a) Geometry idealization (b) Typical stress-strain curve

Figure 1. Illustration of the fiber kinking phenomenon.

1.1 Analytical models for fiber kinking

One of the earliest analytical expressions developed for longitudinal compressive strength X_c of fiber-reinforced composites is given by Rosen [12]

$$X_c = \frac{G^m}{1 - V^f} = G_{12} \tag{1}$$

where G^m is the shear modulus of the matrix, V^f is the fiber volume fraction, and G_{12} is the shear modulus of the composite lamina. This expression was derived assuming kinking is an elastic buckling phenomenon, the fibers are inextensible, $\beta = 0$, and $\varphi_0 = 0$. According to Budiansky [3], relaxing Rosen's analysis to account for $\beta \neq 0$ and $\varphi_0 \neq 0$ still overpredicts experimentally measured compressive strength. Initial fiber misalignment φ_0 of an infinitely long band of fibers ($b \to \infty$) was included by Argon [13] assuming rigid perfectly-plastic shear behavior

$$X_c = \frac{\tau_Y}{\varphi_0} \tag{2}$$

where τ_Y is the yield shear stress of the lamina. The influence of defects on the compressive failure of a fiber reinforced composite was experimentally observed by Chaplin [14] who noted that, for elastic microbuckling, failure should occur along the width of the lamina simultaneously. However, that was not the case in his experiments.

In the analytical expressions in eqs. (1) and (2), compressive failure was assumed to be triggered by fiber microbuckling. For typical high fiber volume fraction composites strength, these expressions overestimate 1.5 to 5 times the experimental values [1]. Budiansky [3] proposed combining the non-linear shear response of the matrix and fiber misalignment in an analytical model. In his initial work, he considered an elastic perfectly-plastic lamina with yield strain $\gamma_Y = \tau_Y / G_{12}$ under longitudinal shear and inextensible fibers. For $\beta = 0$, equilibrium considerations were used to derive

$$X_c = \frac{\tau_Y}{\gamma_Y + \varphi_0} = \frac{G_{12}}{1 + \varphi_0/\gamma_Y} \tag{3}$$

Wisnom [15] derived a similar expression using a micromechanical approach. Later, Budiansky [4] extended eq. (3) to consider strain hardening in the nonlinear shear response of the lamina using a Ramberg-Osgood law [16]

$$\gamma = \frac{1}{G_{12}} \cdot (\tau + \text{sign}(\tau) \cdot \alpha \cdot |\tau|^{\eta}) \tag{4}$$

where G_{12} is the elastic shear modulus of the lamina, and η and α are material parameters of the Ramberg-Osgood model. The closed-form solution for the longitudinal compressive strength using eq. (4) is [4]

$$X_c = \frac{G_{12}}{1 + \eta \cdot \alpha^{1/\eta} \cdot \left(\frac{G \cdot \varphi_0}{\eta - 1}\right)^{\frac{\eta - 1}{\eta}}} \tag{5}$$

The expressions proposed by Budiansky [3, 4] are referred to as fiber kinking theory (FKT). Pinho [17] generalized FKT to any nonlinear shear response and a 3-D stress state (See Appendix A). Hsu et al. [18] proposed an approximation for calculating the complete longitudinal compression stress-strain curve shown in Fig. 1b using FKT where the longitudinal compressive stress is

$$\sigma_c = \frac{\tau(\gamma)}{\gamma + \varphi_0} \tag{6}$$

and the corresponding compressive strain is

$$\varepsilon_c = \varphi_0 \gamma + \frac{\gamma^2}{2} + \frac{\sigma_c}{E_1} \tag{7}$$

Equation (7) is calculated for increments in γ given φ_0, $\tau(\gamma)$, and the longitudinal elastic modulus of the lamina, E_1. The stress-strain curve calculated using eqs. (6) and (7) includes the snapback response and thus follows the dotted line in Fig. 1b.

Barbero [19] derived an expression for strength using the principal of total potential energy. The result was a lengthy expression, so Barbero also proposed a numerical fit to arrive at

$$X_c = G_{12} \left(\frac{\chi}{0.21} + 1\right)^{-0.69} \tag{8}$$

where the constants are nondimensional factors that result from the numerical approximation. In eq. (8), $\chi = G_{12}\tilde{\varphi_0}/\tau_u$ is a dimensionless constant that characterizes the compressive strength, with $\tilde{\varphi_0}$ being the standard deviation of φ_0, and the nonlinear shear response is given by

$$\tau = \tau_u \tanh\left(\frac{G_{12}\gamma}{\tau_u}\right) \tag{9}$$

where G_{12} and τ_u are the material properties that define the shear response. It is emphasized that eq. (8) is not empirical; rather the numerical values are nondimensional and arise from the approximation used as a simplification for the exact solution.

Experimental investigations have reported variation in strength with specimen length [5,20], which is a trend that is not accounted for in eqs. (1) to (3), (5) and (8). Lagoudas and Saleh [21] introduced an energy based formulation considering both macroscale and microscale factors that accounts for the role of specimen length, L, on strength

$$X_c = w_{\text{kb}} \sqrt{\frac{2V^f E_1}{\pi d L} \tau_{Y_m} \varphi_k} \tag{10}$$

where V^f is the fiber volume fraction, E_1 is the laminate modulus, d is the fiber diameter, τ_{Y_m} is the shear yield stress for the matrix only, and φ_k is the angle of the kinked fibers. Wisnom suggested that strain gradient effects may also explain the variations in experimental measurements [22].

Fleck et al. [23] proposed the bending theory of fiber kinking, which uses couple stress theory to account for fiber bending and the wavelength of initial fiber misalignments while maintaining a ply-level homogenization. The couple stress approach includes a bending moment per unit area, which results in a stress tensor that is not symmetric. The analysis shows that fiber bending and imperfection wavelength have a negligible effect on strength prediction for large imperfection wavelengths and carbon fibers. However, consideration of fiber bending is required to predict the kink band width. The authors found that the kink band width is relatively insensitive to material properties and is in the range $10 < w_{\text{kb}}/d < 15$ for typical carbon/epoxy composites.

Budiansky et al. [8] extended his previous work and used couple-stress theory to derive expressions for the behavior of kink bands after they have formed. The angle of fibers at fracture φ_{ff} is found to be

$$\varphi_{\text{ff}} = \left(\frac{2\tau_Y}{E_1^f} \right)^{1/3} \tag{11}$$

An expression for the band broadening stress, which is referred to as the residual stress σ_r herein, is also given in [8]

$$\sigma_r = \frac{2\tau_L}{\sin 2\beta} \tag{12}$$

where τ_L is the shear stress associated with large rotations (the approximation $\tau_L = 2\tau_Y$ is suggested). The parameter β is left unspecified since no simple explanation for the range of experimentally reported values of $10^\circ < \beta < 30^\circ$ [24] was available.

Moran et al. [25] proposed an expression for the residual stress based on an energy balance and preservation of volume ($\varphi = 2\beta$)

$$\sigma_r = \frac{1}{2\sin^2\beta} \int_0^{2\tan\beta} \tau(\gamma) dx \tag{13}$$

where $\tau(\gamma)$ is the nonlinear stress-strain law in shear. Moran suggested a trilinear curve for $\tau(\gamma)$. The resulting expression for σ_r is minimized with respect to β. Moran demonstrated this approach yields reasonable values for both β and σ_r for ductile matrix composites. However, other authors have questioned the validity of the $\varphi = 2\beta$ assumption, e.g. [9]. It is noted that Moran's approach can be extended to strain hardening shear nonlinearity curves such as eq. (4) using numeric integration.

Moran's model is one of the very few analytical models that determine β; most models require β to be specified as an input parameter. Schapery [26] proposed that β is set by a balance between satisfying a matrix tensile failure criterion and shear instability. Despite these efforts, no consensus has been reached for predicting analytically σ_r or β.

In contrast to the aforementioned homogenized mesoscale models, a micromechanical approach has been taken by others. Hahn and Williams [27] derived a model based on equilibrium of an initially misaligned fiber in a matrix with a nonlinear shear response. Effendi [28] added considerations for fiber failure and showed that low strength fibers with small initial fiber misalignments fail by fiber compression, while composites with larger initial fiber misalignments failed by fiber kinking.

Pimenta et al. [29] built on the approach used in [27] to derive a closed-form expression for the longitudinal compression strength and predict the post-failure response of a unidirectional lamina. The model is based on the equilibrium of an imperfectly aligned fiber loaded in compression and bending, and supported in shear by an elastic perfectly-plastic matrix. An initial fiber misalignment given by $y_0(x) = \bar{y}_0 \cdot (1 - \cos(\pi x/L))$ is assumed where the fiber axis is along the x-direction and the parameters $\bar{y}_0$ and L define the initial imperfection. The expression for the compressive strength is

$$X_c = \tau_Y \frac{G^m_{2\mathrm{D}} d + \frac{\pi^2}{L^2} E^f_1 I^f_x}{\tau_Y + \pi \frac{\bar{y}_0}{L} G^m_{2\mathrm{D}}} \left(\frac{V^f_{2\mathrm{D}}}{A^f} \right) \tag{14}$$

where superscript ^{f} indicates quantities associated with the fibers and $G^m_{2\mathrm{D}} = G^m/(1 - V^f_{2\mathrm{D}})$ with $V^f_{2\mathrm{D}} = d/(d + t^m)$ where t^m is the thickness of the matrix in the 2-D approximation and d is the fiber diameter. Assuming that fiber failure is governed by maximum compressive stress, w_{kb} is obtained from the analysis by identifying the location along the fiber where the maximum stress criterion is satisfied. The trends predicted from this model were found to be consistent with the bending theory for fiber kinking [23].

While these analytical models provide great insight and utility, they lack the ability to analyze particular structural configurations and ignore many details of the kinking process. For these reasons, several numerical approaches have been proposed using the finite element (FE) method. FE modeling approaches that are relevant to the mesoscale and microscale models developed herein are reviewed in the following two sections.

1.2 Modeling fiber kinking at the mesoscale using FE

A variety of FE modeling approaches for fiber kinking in homogenized lamina (i.e. mesoscale) have been proposed. Wisnom [30] introduced superposing beam elements on a continuum mesh where the beam elements represent the fibers and the continuum mesh represents the matrix. The study showed the importance of considering fiber rotation, shear nonlinearity in the matrix, and bending of the fibers in order to make accurate predictions of fiber kinking. Wisnom pointed out that most commercial FE codes lack the ability to represent fiber rotation and fiber bending in a homogenized mesoscale model, and thus require techniques such as the beam superposition approach to predict fiber kinking. Other authors have used Wisnom's approach to study the effects of the distribution of fiber misalignments [31, 32] and fiber packing [33].

In order to account for fiber bending in homogenized mesoscale models, Fleck and Shu [34] used Cosserat theory (also termed micropolar theory), which is a higher order continuum theory that introduces stress couples into the constitutive law. The model was used to explore the FKT assumption of an infinitely long band ($b \to \infty$ in Fig. 1a) of misaligned fibers. Finite element simulations using the two-dimensional (2-D) couple stress based model showed the effect of the size of the initial imperfection where, as b increases from zero to infinity, the strength decreases from the value predicted by eq. (1) to the asymptote predicted by the one-dimensional (1-D) couple stress model in [23]. This model has been extended to study the effect of multiaxial loading [35], strain gradient effects [36], and random fiber waviness [37]. Hasanyan and Waas [38] proposed calibration procedures to define the unconventional material property inputs for their couple stress theory based model using micromechanical models. These higher order continuum approaches show tremendous promise, but their usage remains limited since they depart from standard conventions in structural analyses (e.g., using an unsymmetrical stress tensor), which makes implementation into commercial FE codes challenging.

In contrast to the efforts to model fiber kinking directly, some authors have used phenomenological constitutive laws that resemble the characteristic fiber kinking response (Fig. 1b). In these approaches, the constitutive laws are defined by model input parameters that define the residual stress σ_r and fracture toughness. Careful selection of model parameters enables accurate simulations of damage for complex structures, e.g. [39–43]. However, the predictive capability of these approaches is limited due to the requirement for calibration at the structural scale.

Approaches based on FKT where the fiber rotation and shear nonlinearity are carefully modeled provide an appealing alternative. Basu et al. [44] formulated one such model using Schapery theory [45] where the misaligned fiber direction was tracked by integrating the increment in shear strain. Good agreement for strength as predicted by a 2-D model similar to that of Kyriakides [5] was achieved. Feld et al. [46] proposed augmenting an existing continuum damage mechanics (CDM) model with an additional term based on a rheological model to account for fiber kinking. Davidson and Waas [47] used Hill's anisotropic plasticity to model out-of-plane kinking. By introducing thin regions representing resin-rich layers between the plies, predictions with $\beta > 0$ were obtained. Bergan and Leone [48] proposed

a CDM model based on fiber kinking theory that uses the deformation gradient decomposition (DGD) method [49] to account for the coupling between longitudinal splitting and fiber kinking. The model predictions show that large rotations and shear nonlinearity dominate the response. Likewise, Gutkin, Costa, and Olsson [50–52] introduced a model based on fiber kinking theory and a physically based constitutive law for shear nonlinearity. The authors demonstrated that the model is capable of predicting the compression strength and residual stress. These methods are attractive since they are physically based on the mechanics of fiber kinking, while, at the same time, they avoid the complications of high-order theories. The mesoscale model developed herein adopts this approach.

1.3 Microscale FE modeling of fiber kinking

Numerical micromechanical models of fiber kinking have offered important insights. By explicitly modeling the fiber and matrix individually in a representative volume element (RVE) and accounting for material and geometric nonlinearity, the fiber kinking process can be modeled numerically. Some of the first such models were developed by Kyriakides et al. [5] consisting of a 2-D representation with a layered composite of alternating elastic fibers and J_2 flow theory elasto-plastic matrix. The layers followed a sinusoidal curve representing the initial fiber misalignment (φ_0). These models were among the first to predict the sequence of events leading to the formation of kink bands and realistic values for the kink band angle, β, determined by fiber failure.

One of the first three-dimensional (3-D) micromechanical FE models for fiber kinking was developed by Hsu et al. [18] to assess the limitations of 2-D models. The model used a hexagonal fiber pattern with 60 elastic, isotropic fibers and J_2 flow theory elasto-plastic behavior for the matrix. The authors demonstrated that 2-D and 3-D models were in good agreement for predictions of X_c when separate 2-D and 3-D RVEs were used to calibrate the plasticity parameters to the same test data for the shear stress-strain response. The authors noted that the matrix shear response resulting from the calibration differed for the 2-D and 3-D models. Furthermore, the matrix shear response is not equivalent to measurements for neat resin. In contrast to the good agreement for strength, the post-peak predictions for the two models differ: the 3-D model predicts larger values for w_{kb} and β. In the same study, the FE models were compared with analytical FKT predictions. While the strength predictions were in good agreement, the FKT predicted larger values for the residual stress, σ_r. Thus the authors highlighted the complications of accurate prediction of the post-peak regime. The authors modified the 3-D model in a follow up study on the propagation behavior of already-formed kinks, where β was explicitly modeled [53]. Reasonable agreement was demonstrated with Budiansky's band broadening stress (i.e. residual stress), eq. (12). Fiber kinking initiation and kink band propagation transverse to the fibers was systematically tested and simulated by Vogler et al. [54, 55]. Experimental tests were carried out holding a constant longitudinal compressive load while applying a progressive shear load under displacement control. In this manner, kink band propagation along the width of the specimen was noticeably more stable. It was observed that kink band inclination,

β, was insensitive to the initial imperfection features. The numerical model considered a Drucker-Prager model for the matrix to account for inelastic dilatancy and sensitivity to hydrostatic pressure which were found to affect the post-peak regime of the composite, especially the β angle.

Yerramalli and Waas [56] developed a 3-D model with 37 fibers that accounted for fiber orthotropy and J_2 flow theory of plasticity for the matrix. An RVE with shear loads was used to calibrate the shear nonlinearity curve. By comparing the results obtained using isotropic fibers, consideration of fiber orthotropy was shown to reduce the post-peak residual stress σ_r. Examination of the stresses in the fibers showed that high shear strains in the fibers would likely lead to failure and that smaller diameter fibers may break before fiber kinking occurs.

A number of 2-D micromechanical models have been developed building on the foundational efforts described above to study different features and parameters affecting the fiber kinking phenomenon. Gutkin et al. [57] analyzed the failure envelopes for fiber reinforced composites under combined longitudinal compression and in-plane shear ($\sigma_{11} - \tau_{12}$) through a single-fiber 2-D model employing periodic boundary conditions (PBC). This study showed two types of failure mechanisms: shear-driven fiber failure and kink-band formation, which were confirmed in the complementary experimental work [58]. Interaction between fiber kinking and fiber-matrix debonding (splitting) was investigated by Prabhakar et al. [59] using a multiple-fiber 2-D model which incorporated a cohesive zone model between the fibers and the matrix. The results suggested that it may be important to consider both fiber kinking and matrix splitting for accurate prediction of compressive strength.

Modern computational resources have enabled massive multi-fiber 3-D micromechanical models. Bai et al. [60] developed one such model and subjected it to a triaxial stress state including longitudinal compression. The model results show the same sequence of events as shown by other authors, with plasticity in the matrix being the most dominant factor leading to kinking. A multiscale FE model of a 3-D cross-ply laminate section was developed by Bishara et al. [61] with the longitudinal plies represented through a single row of fibers as in [62], while the 90° plies were modeled by means of a homogeneous CDM model. This multiscale model was able to capture several failure mechanisms including fiber kinking formation in the 0° plies, subsequent delamination between adjacent plies and matrix cracking in the 90° plies.

Recently, Naya et al. [63] developed a 3-D micromechanical model generated by extruding a fiber distribution along a sinusoidal curve representing the initial fiber misalignment, φ_0. The model consists of fibers oriented in the extrusion direction, a pressure-dependent polymer matrix and a cohesive interaction in the fiber-matrix interface accounting for friction. The application of periodic boundary conditions, as in [57], permits the model to be simplified to a single-fiber system. The model predictions were found to be in good agreement with experimental measurements.

1.4 Objective and outline

The aim of this work is to compare and validate a mesoscale CDM model to capture fiber kinking with a high fidelity computational micromechanics (CMM) model based on the micromechanical model published in [63]. The CMM model is used to assess the relative significance of various model features and assumptions in order to improve the understanding of the mechanics of the fiber kinking process. While the CMM model is a powerful tool for analyzing the mechanics of the kinking process, its small scale precludes application to typical structures. Therefore, the CMM model is exploited to interrogate the assumptions of the mesoscale model for fiber kinking.

This report is organized as follows. In Section 2, the CDM model is described in detail including the phenomenological basis, constitutive equations, element decomposition, and model verification. The FE micromechanical models are presented in Section 3: the single-fiber kinking model, multi-fiber kinking model, and the in-plane shear model. The CMM models rely on several unconventional experimental measurements for input properties. A new micromechanical test procedure to obtain the compressive strength of carbon fibers through micropillars indentation is described in Section 3.3. Results from the CMM and CDM models are compared in Section 4. Two parametric studies taking advantage of the micromechanical model developed are shown in Section 5. Finally, concluding remarks are presented in Section 6.

2 Mesoscale Model

A mesoscale constitutive model is formulated in this section with the aim of representing the fiber kinking phenomenon using geometric nonlinearity and shear nonlinearity. The model is developed for the purpose of analyzing longitudinal compression failure at the structural scale. As a result of the objective to analyze structural failure, the model includes several simplifying assumptions. The formulation is based on Budiansky's fiber kinking theory [3,4,8] with the assumption that $\beta = 0$. The model includes the kinematics of the fiber kinking process by tracking fiber misalignment throughout loading. The characteristic constitutive response shown in Fig. 1b is not directly prescribed in the model. Instead, this characteristic response is a result of the shear nonlinearity and large rotation of the fiber. The model is formulated in the context of CDM and is integrated into the existing code CompDam [64]. CompDam is a NASA-developed open-source material model implemented as an Abaqus user subroutine for predicting damage in carbon fiber reinforced polymer laminates [65]. The deformation gradient decomposition (DGD) [49] method is used for accurate representation of the kinematics of the kink band and fiber misalignments. The following subsections describe the model formulation, implementation, and verification. This report focuses on the model development in CompDam and does not directly address application of the mesoscale model to analyze structural failure.

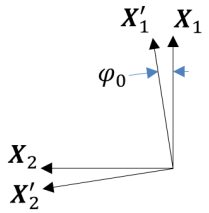

Figure 2. The two coordinate systems used in the CDM model shown in the reference configuration.

2.1 Constitutive model formulation

The material model computes the stress state given the current deformation, state variables, and material properties as follows. Consider a material point with a reference frame, $\boldsymbol{X}$. An initial fiber misalignment angle, φ_0, is assumed such that a fiber-aligned reference frame, $\boldsymbol{X}'$, is defined with rotation, $\boldsymbol{R}_{\varphi_0}$, as

$$\boldsymbol{X}' = \boldsymbol{R}_{\varphi_0}\boldsymbol{X} \tag{15}$$

where

$$\boldsymbol{R}_{\varphi_0} = \begin{bmatrix} \cos\varphi_0 & -\sin\varphi_0 & 0 \\ \sin\varphi_0 & \cos\varphi_0 & 0 \\ 0 & 0 & 1 \end{bmatrix} \tag{16}$$

The two reference frames are shown in Fig. 2. For a given deformation gradient, $\boldsymbol{F}$, the Green-Lagrange strain, $\boldsymbol{E}$, is calculated as

$$\boldsymbol{E} = \frac{1}{2}(\boldsymbol{F}^\top\boldsymbol{F} - \boldsymbol{I}) \tag{17}$$

Shear nonlinearity is accounted for in the $\boldsymbol{X}_1'$–$\boldsymbol{X}_2'$ plane using a one-dimensional plasticity model as follows

$$\boldsymbol{E}' = \boldsymbol{R}_{\varphi_0}^\top\boldsymbol{E}\boldsymbol{R}_{\varphi_0} - \frac{\gamma_{12}^{PL}}{2}\begin{bmatrix} 0 & 1 & 0 \\ 1 & 0 & 0 \\ 0 & 0 & 0 \end{bmatrix} \tag{18}$$

where the plastic portion of the shear strain is $\gamma_{12}^{PL} = \gamma_{12} - \gamma_{12}^{EL}$. The nonlinear shear behavior of the matrix is often modeled using a third-order polynomial [17], a hyperbolic tangent [66], or a power law such as the Ramberg-Osgood curve [16]. Herein, the Ramberg-Osgood expression is used

$$\gamma_{12} = \frac{1}{G_{12}}[\tau_{12} + \text{sign}(\tau_{12})\,\alpha\,|\tau_{12}|^\eta] \tag{19}$$

where γ_{12} is the shear strain, G_{12} is the shear modulus of the composite, and α and η are parameters that define the strain-hardening portion of the Ramberg-Osgood

curve. The second Piola-Kirchoff stress in the fiber-aligned reference frame, $\boldsymbol{S}^{'}$, is calculated using the elastic stiffness tensor, $\boldsymbol{C}$

$$\boldsymbol{S}^{'} = \boldsymbol{C} : \boldsymbol{E}^{'} \tag{20}$$

with

$$\boldsymbol{C} = \boldsymbol{H}^{-1} \tag{21}$$

and

$$\boldsymbol{H} = \begin{bmatrix} \frac{1}{E_1^*} & \frac{-\nu_{21}}{E_2} & \frac{-\nu_{31}}{E_3} & 0 & 0 & 0 \\ \frac{-\nu_{12}}{E_1^*} & \frac{1}{E_2} & \frac{-\nu_{32}}{E_3} & 0 & 0 & 0 \\ \frac{-\nu_{13}}{E_1^*} & \frac{-\nu_{23}}{E_2} & \frac{1}{E_3} & 0 & 0 & 0 \\ 0 & 0 & 0 & \frac{1}{G_{12}} & 0 & 0 \\ 0 & 0 & 0 & 0 & \frac{1}{G_{23}} & 0 \\ 0 & 0 & 0 & 0 & 0 & \frac{1}{G_{13}} \end{bmatrix} \tag{22}$$

using the typical elastic constants and the order of the shear terms follows the Abaqus/Explicit convention. Elastic nonlinearity in the longitudinal direction is considered with a linear dependence of stiffness on strain producing a quadratic stress vs. strain curve as in [67]

$$E_1^* = E_1(1 + c^l \varepsilon_{11}) \tag{23}$$

where c^l is the nonlinearity coefficient for the lamina and is an additional material property to be obtained from test data or micromechanics characterization of the fiber. In the reference frame, $\boldsymbol{X}$, the second Piola-Kirchoff stress is

$$\boldsymbol{S} = \boldsymbol{R}_{\varphi_0} \boldsymbol{S}^{'} \boldsymbol{R}_{\varphi_0}^{\top} \tag{24}$$

Finally, the Cauchy stress is calculated

$$\boldsymbol{\sigma} = \boldsymbol{F}\boldsymbol{S}\boldsymbol{F}^{\top} |\boldsymbol{F}|^{-1} \tag{25}$$

This model has been implemented in Abaqus/Explicit [65] as a VUMAT. The following subsections include practical considerations for implementation as a material model for finite element analysis.

2.2 Initial misalignment angle

The initial misalignment angle, φ_0, accounts for fiber misalignments and other manufacturing anomalies that may contribute to fiber kinking initiation. The initial fiber misalignment is calculated by rearranging eq. (5) as

$$\varphi_c = \frac{\eta - 1}{G_{12}} \cdot \left(\frac{G_{12} - X_c}{X_c \, \eta \, \alpha^{\frac{1}{\eta}}} \right)^{\frac{\eta}{\eta - 1}} \tag{26}$$

where φ_c is used instead of φ_0 to emphasize that the particular value for φ_0 obtained from eq. (26) corresponds to the strength, X_c. The fiber misalignment φ_c is fully defined in terms of material property inputs. Some authors have suggested that X_c is not a material property due to the variation in measured values for X_c with specimen size and test configuration [20,68]. The dependence of the present model on X_c as a material property input could be eliminated by considering experimentally measured fiber misalignments in place of eq. (26). A first step towards using experimentally measured fiber misalignments is investigated by considering the spatial variation of φ_0 in Section 2.7.

2.3 Mesh objectivity and decomposition

Material models that exhibit strain-softening behavior are mesh sensitive when strain localizes. In conventional CDM models, this deficiency is typically addressed with Bažant's crack band theory [69] in which the energy dissipated during failure of a material point is scaled by the element size. In the present model, there is no crack surface on which traction goes to zero and therefore the crack band theory is not applicable. Nonetheless, there is an inherent mesh sensitivity since the model includes a strain-softening response leading to strain localization in a band of elements after the strength is reached. Recently, Costa et al. [52] identified this mesh sensitivity as it relates to modeling fiber kinking and recommended two options for ensuring mesh objectivity. The method used herein is analogous to the strain decomposition method proposed by Costa et al. [52] and is an adaption following previous work by Bergan and Leone [48].

When the plastic strain in an element becomes non-negligible, an element decomposition is performed. The kink band width, w_{kb}, is assumed to be smaller than the element size in the X_1-direction, l_1. The relative kink band size is defined as $\overline{w}_{\text{kb}} = w_{\text{kb}}/l_1$. When $\overline{w}_{\text{kb}} \leq 0.95$, the element is decomposed into an undamaged material region and a kink band region, as shown in Fig. 3, in order to preserve mesh objectivity. In the decomposed element, shear nonlinearity is enabled in the kink band region, whereas in the undamaged material region the shear response is linear. When $\overline{w}_{\text{kb}} > 0.95$, the kink band width is close enough to the element size that the decomposition has a negligible effect on the constitutive response; as such, the material model described in Section 2.1 is applied directly without decomposition of the element. When the element is decomposed, the DGD approach [48, 49] is used to enforce continuity and equilibrium conditions between the undamaged and kink band regions as follows.

Consider a rectangular continuum of fiber-reinforced material where the fiber direction is initially aligned with the reference X_1-direction. The reference configuration is defined as

$$\boldsymbol{X} = \begin{bmatrix} l_1 & 0 & 0 \\ 0 & l_2 & 0 \\ 0 & 0 & l_3 \end{bmatrix} \tag{27}$$

where the nonzero diagonal components are the undeformed dimensions of the continuum. The current configuration, $\boldsymbol{x}$, is a function of $\boldsymbol{X}$ and the deformation

gradient, $\boldsymbol{F}$

$$\boldsymbol{x} = \boldsymbol{F}\boldsymbol{X} \tag{28}$$

$\boldsymbol{F}$ is decomposed into a deformation gradient for the undamaged material region, $\boldsymbol{F}_{\mathrm{m}}$, and a deformation gradient for the kink band region, $\boldsymbol{F}_{\mathrm{kb}}$. In the fiber direction, compatibility of the deformations requires

$$\boldsymbol{x}^{(1)} = (1 - \overline{w}_{\mathrm{kb}})\, \boldsymbol{x}_{\mathrm{m}}^{(1)} + \overline{w}_{\mathrm{kb}} \boldsymbol{x}_{\mathrm{kb}}^{(1)} \tag{29}$$

where the superscript $^{(1)}$ indicates the first column of $\boldsymbol{x}$. Substituting eqs. (27) and (28) into eq. (29)

$$\boldsymbol{F}\boldsymbol{X}^{(1)} = (1 - \overline{w}_{\mathrm{kb}})\, \boldsymbol{F}_{\mathrm{m}}\boldsymbol{X}^{(1)} + \overline{w}_{\mathrm{kb}} \boldsymbol{F}_{\mathrm{kb}}\boldsymbol{X}^{(1)} \tag{30}$$

then simplifying and rearranging yields an expression for $\boldsymbol{F}_{\mathrm{kb}}$ in the 1-direction

$$\boldsymbol{F}_{\mathrm{kb}}^{(1)} = \frac{1}{\overline{w}_{\mathrm{kb}}} \boldsymbol{F}^{(1)} + \left(1 - \frac{1}{\overline{w}_{\mathrm{kb}}}\right) \boldsymbol{F}_{\mathrm{m}}^{(1)} \tag{31}$$

In the X_2-direction, there is no decomposition, so compatibility of the deformation requires

$$\boldsymbol{x}_{\mathrm{kb}}^{(2)} = \boldsymbol{x}_{\mathrm{m}}^{(2)} = \boldsymbol{x}^{(2)} \tag{32}$$

Substituting eq. (28) into eq. (32) and simplifying yields

$$\boldsymbol{F}_{\mathrm{kb}}^{(2)} = \boldsymbol{F}_{\mathrm{m}}^{(2)} = \boldsymbol{F}^{(2)} \tag{33}$$

Using eqs. (31) and (33) with $\boldsymbol{F}$ provided as an input, the quantities $\boldsymbol{F}_{\mathrm{kb}}$ and $\boldsymbol{F}_{\mathrm{m}}$ can be determined in terms of the unknown $\boldsymbol{F}_{\mathrm{m}}^{(1)}$ through the equilibrium equations as described in the following section.

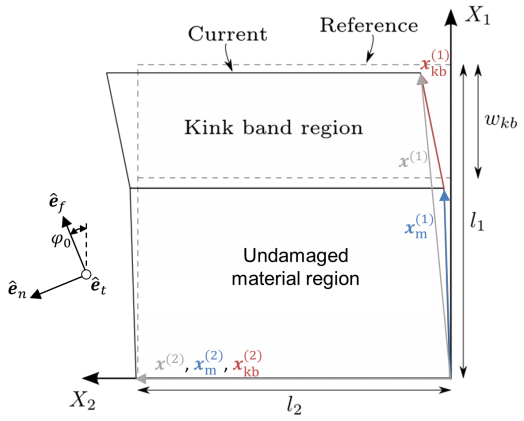

Figure 3. Schematic representation of the model: element decomposition into the kink band region and the undamaged material region.

2.4 Equilibrium and solution procedure

It is necessary to ensure that the tractions that arise in the kink band and the neighboring undamaged material are in equilibrium. Equilibrium is enforced between the kink band region and the neighboring undamaged material on the plane normal to $\hat{\mathbf{e}}_f$, where the current misaligned reference frame is

$$\boldsymbol{R} = \begin{bmatrix} \hat{\mathbf{e}}_f & \hat{\mathbf{e}}_n & \hat{\mathbf{e}}_t \end{bmatrix} \tag{34}$$

where the carrot indicates a unit vector, $\hat{\mathbf{n}} = \boldsymbol{n}/||\boldsymbol{n}||$, and

$$\boldsymbol{e}_f = \boldsymbol{F}_{\text{kb}} \begin{bmatrix} \cos\varphi_0 \\ \sin\varphi_0 \\ 0 \end{bmatrix} \tag{35}$$

$$\boldsymbol{e}_n = \boldsymbol{F}_{\text{kb}}^{-\top} \begin{bmatrix} -\sin\varphi_0 \\ \cos\varphi_0 \\ 0 \end{bmatrix} \tag{36}$$

$$\boldsymbol{e}_t = \boldsymbol{e}_f \times \boldsymbol{e}_n \tag{37}$$

The current fiber misalignment is obtained from eqs. (34) to (37) as

$$\varphi = \tan^{-1}\left(\frac{R_{21}}{R_{11}}\right) \tag{38}$$

Cauchy's stress theorem is used to obtain the stress vector acting on a plane defined by the fiber direction in the kink-band region

$$\boldsymbol{t}_{\text{kb}} = \boldsymbol{\sigma}_{\text{kb}} \cdot \hat{\mathbf{e}}_f \tag{39}$$

where $\boldsymbol{\sigma}_{\text{kb}}$ is calculated from eqs. (17) to (25). Likewise, in the undamaged material region

$$\boldsymbol{t}_{\text{m}} = \boldsymbol{\sigma}_{\text{m}} \cdot \hat{\mathbf{e}}_f \tag{40}$$

where $\boldsymbol{\sigma}_{\text{m}}$ is also calculated from eqs. (17) to (25) with the exception that the second term in eq. (18) is omitted. An iterative solution procedure is required to solve for the state of stress at equilibrium. A residual stress vector $\boldsymbol{t}_{\text{res}}$ is defined in terms of the stress vectors in eqs. (39) and (40) in the current misaligned coordinate system as

$$\boldsymbol{t}_{\text{res}} = \boldsymbol{R}^{\top}(\boldsymbol{t}_{\text{m}} - \boldsymbol{t}_{\text{kb}}) \tag{41}$$

Newton-Raphson iteration is used to solve eq. (41) for $\boldsymbol{F}_{\text{m}}^{(1)}$. The iterations are determined to be converged when $|\boldsymbol{t}_{\text{res}}|$ is less than a tolerance. Herein, 0.01% of the shear strength is used as the convergence tolerance.

2.5 Determination of the kink band width

While the model includes fiber rotation, bending of the fibers is ignored, which is one of the fundamental assumptions of FKT. As a result of this assumption, w_{kb} cannot be predicted by the model [3,4]. As such, w_{kb} is an input parameter for the model and must be obtained from micromechanical analysis or experimental measurements. Values reported in the literature for different carbon/epoxy composites are summarized in Table 3.

Budiansky [3] derived an expression for w_{kb} by accounting for rigid-perfectly plastic shear nonlinearity and inextensional bending of perfectly aligned fibers using a couple-stress formulation. Assuming $\beta = 0$, w_{kb} is

$$\frac{w_{\text{kb}}}{d} = \frac{\pi}{4}\left(\frac{E_1}{2\tau_Y}\right)^{1/3} \tag{42}$$

where d is the fiber diameter and τ_Y is the shear yield stress. Budiansky suggested a kink band width of about 12 fiber diameters for typical carbon/epoxy materials. Jelf and Fleck [24] fit an expression with the same form as eq. (42) to experimental data for AS4/PEEK and found that

$$\frac{w_{\text{kb}}}{d} = 0.68\left(\frac{E_1}{2\tau_Y}\right)^{0.37} \tag{43}$$

was in good agreement with the test data, which is very similar to Budiansky's expression, eq. (42). The kink band widths predicted using eq. (42) and eq. (43) for the materials analyzed in this work, AS4/8552 and IM7/8552, are shown in Table 3, with $\tau_Y = 95$ MPa determined from the Ramberg-Osgood shear curve using a 5% offset, and the fiber diameters reported in Table 6. Herein, the kink band width of the CDM model was set to 100 and 50 µm for AS4/8552 and IM7/8552, respectively, which is on the order of values reported in the literature, see Table 3.

Table 3: Values of w_{kb} reported in the literature.

Material system	w_{kb} [µm]	Method	Reference
AS4/8552	59	Analytical 2D, eq. (42)	Budiansky et al. [3]
AS4/8552	67	Experimental, eq. (43)	Jelf et al. [24]
AS4/8552	120	3-D micromechanical FE	Naya et al. [63]
IM7/8552	25	Microscopy	Laffan et al. [70]
IM7/8552	25	In situ X-Ray CT	Bergan and Garcea [71]
IM7/8552	45	Analytical 2D, eq. (42)	Budiansky et al. [3]
IM7/8552	50	Microscopy	Zobeiry et al. [72]
IM7/8552	51	Experimental, eq. (43)	Jelf et al. [24]
HTS/RTM6	200	Microscopy	Svensson et al. [73]
HTS40/977-2	80	Microscopy	Jumahat et al. [74]
T300/913	70	Microscopy	Pinho et al. [75]
T700/977-2	55	Microscopy	Hapke et al. [76]
T800/924C	55	Microscopy	Soutis [77]
T800/924	50	Microscopy	Gutkin et al. [58]
T800/924	250	Analytical 2D	Pimenta el al. [29]
AS4/3501	49	3-D micromechanical FE	Bai et al. [60]

2.6 Element deletion

Fiber kinking often occurs at or near collapse and may correspond with a substantial release of energy. As a result, difficulties including excessive mesh distortion, excessive deformation rate, or failure to find a converged solution to eq. (41) may occur in an analysis, especially for problems that fail by unstable collapse. When one of these errors occurs and the analysis terminates, the strength prediction is ambiguous because, while the analysis output indicates the type of error that occurs, no load drop is predicted. Consequently, it is unclear when structural failure occurs. To circumvent these runtime errors, element deletion can be enabled by specifying values for the following conditions

$$|\boldsymbol{F}_{\text{kb}}| < F_{\text{TOL}} \tag{44}$$

$$n_{\text{NR}} > n_{\max} \tag{45}$$

$$|\gamma_{12}| > \gamma_{\text{TOL}} \tag{46}$$

where $|\boldsymbol{F}_{\text{kb}}|$ is the determinant of $\boldsymbol{F}_{\text{kb}}$, n_{NR} is the number of Newton-Raphson iterations to solve eq. (41), and $|\gamma_{12}|$ is the absolute value of γ_{12}. When any of the conditions in eqs. (44) to (46) is satisfied, the element is deleted. Element deletion is disabled in the analyses discussed in the subsequent sections except where noted otherwise.

2.7 Model verification

The steps taken to verify the performance of the mesoscale model are described in this section. First, single element models were used to verify the constitutive response. The key characteristics of the constitutive response are noted and compared with predictions from FKT. Then, mesh objectivity is demonstrated. The verifications are performed using two common materials, IM7/8552 and AS4/8552, with the material properties listed in Table 4.

Table 4: Material properties for the CDM model.

Material	E_1 [GPa]	E_2 [GPa]	G_{12} [GPa]	ν_{12}	ν_{23}	α [MPa$^{1-\eta}$]	η	X_c [MPa]
AS4/8552 [79]	131.6	9.24	4.83	0.30	0.45	2.86 10^{-11}	6.49	1480
IM7/8552 [80]	152.7	8.7	5.16	0.32	0.45	4.06 10^{-9}	5.4	1731

The fiber-direction moduli, E_1, reported in Table 4 are the tensile values measured on the interval 0.1% and 0.3% strain. Often, separate values for E_1 are reported for tension and compression for a piecewise linear representation. A more elegant approach is to represent the elastic nonlinearity of the fibers as a continuous function. Herein, eq. (23) is used to represent the fiber nonlinearity, thereby adding the requirement to calibrate the fiber nonlinearity parameter, c^l. Test data from tension and compression tests of IM7/8552 unidirectional specimens reported by Peterson and Murphey [78] are shown in Fig. 4 as the light gray lines (one line for each test replicate). It is evident that the fiber nonlinearity occurring at large

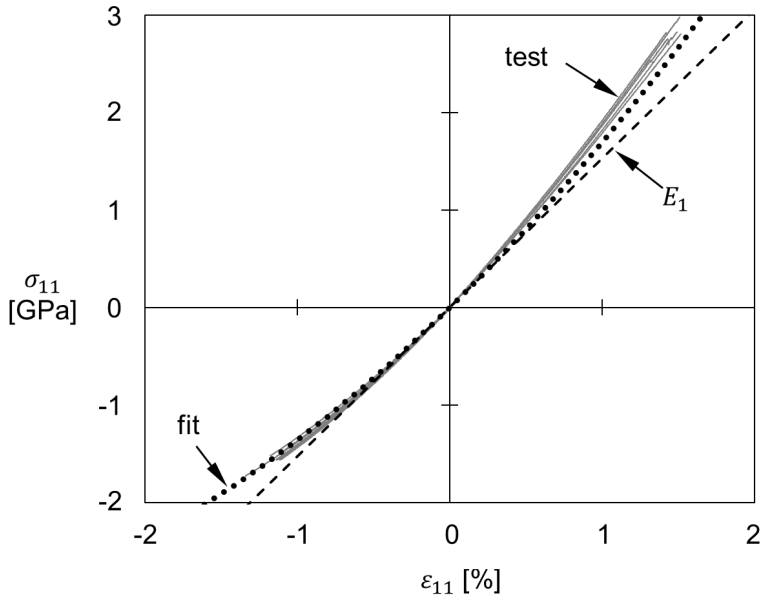

Figure 4. Fiber-direction stress-strain data for IM7/8552 lamina [78].

strains is not well captured by the stiffness on the interval between 0.1% and 0.3%. The dashed line in the figure corresponds to $E_1 = 152.7$ GPa. A least squares fit is used to obtain $c^l = 11$ with the resulting curve shown as the dotted back line in the figure. It is observed that accounting for fiber nonlinearity is important for large strains ($\varepsilon > 0.8\%$). While ply-scale test data was obtained from the literature for IM7/8552, no comparable data was available for AS4/8552. However, experimental single-fiber tests were conducted to obtain a fiber nonlinearity parameter at the fiber-scale, c^f, as described in Section 3.3.1. This value was related to the lamina through the rule of mixtures, $c^l = V^f \cdot c^f$, where $V^f = 60\%$ is the fiber volume fraction. Following this procedure, the value obtained for AS4/8552 was $c^l = 12.2$.

2.7.1 Verification of the constitutive response: single element model

Analyses were conducted using a model with a single C3D8R element subjected to uniform end shortening in the longitudinal direction in order to verify the constitutive behavior of the model. Boundary conditions were imposed to prevent hourglassing modes of deformation. The element had a uniform edge length of $l_1 = 0.15$ mm. A smooth-step was applied with a duration of 0.1 seconds and uniform mass scaling was applied with a factor of 10^4. Rayleigh damping was used to limit vibrations which occur as a result of the large load drop when the strength is reached. The value of the Rayleigh damping coefficient, α_R, was chosen so as to minimize the vibration without changing the overall response.

The stress vs. strain results predicted by the model for the IM7/8552 material system are shown in Fig. 5a. The compressive stress, σ_c, is calculated from the reaction force divided by the element cross-sectional area, $\sigma_c = F_1/(l_2 l_3)$. Likewise, the compressive strain is obtained from the end shortening displacement $\varepsilon_c = u_1/l_1$. The stress vs. strain results are shown as the solid black and gray lines that lay on top of each other, where the gray line is the result for the undamped model $\alpha_R = 0$ and the black line is the result for the damped model with $\alpha_R = 10^4$. The linear stiffness calculated using E_1 is denoted by the dotted line. The strength is shown on the plot as the horizontal line labeled X_c. The results from FKT, eqs. (6) and (7), are shown with cross symbols. The results show that the model reproduces the initial stiffness in good agreement with the linear stiffness at small strains. At larger strains, the model predicts that the stiffness degrades as the strength is approached. The stiffness reduction is primarily a result of the fiber nonlinearity, eq. (23). However, fiber rotation also contributes to the stiffness reduction. The strength from the model is in very good agreement with the input property, where it can be observed that the model just slightly over predicts the input value of X_c by 1.6%. Once the strength is reached, a snap-back phenomenon occurs as shown for the FKT results. Since the present model is not capable of predicting the snap-back behavior, the model response has an abrupt drop followed by vibration. The vibrations are mostly suppressed by damping in the case where $\alpha_R = 10^4$, with no other significant change in the response as compared with the undamped case. After the dynamic effects from the abrupt load drop dissipate at around 2% strain, the damped and undamped case suggest the same behavior where a residual stress level, σ_r, is approached asymptotically. A range of σ_r is calculated using eq. (12) with

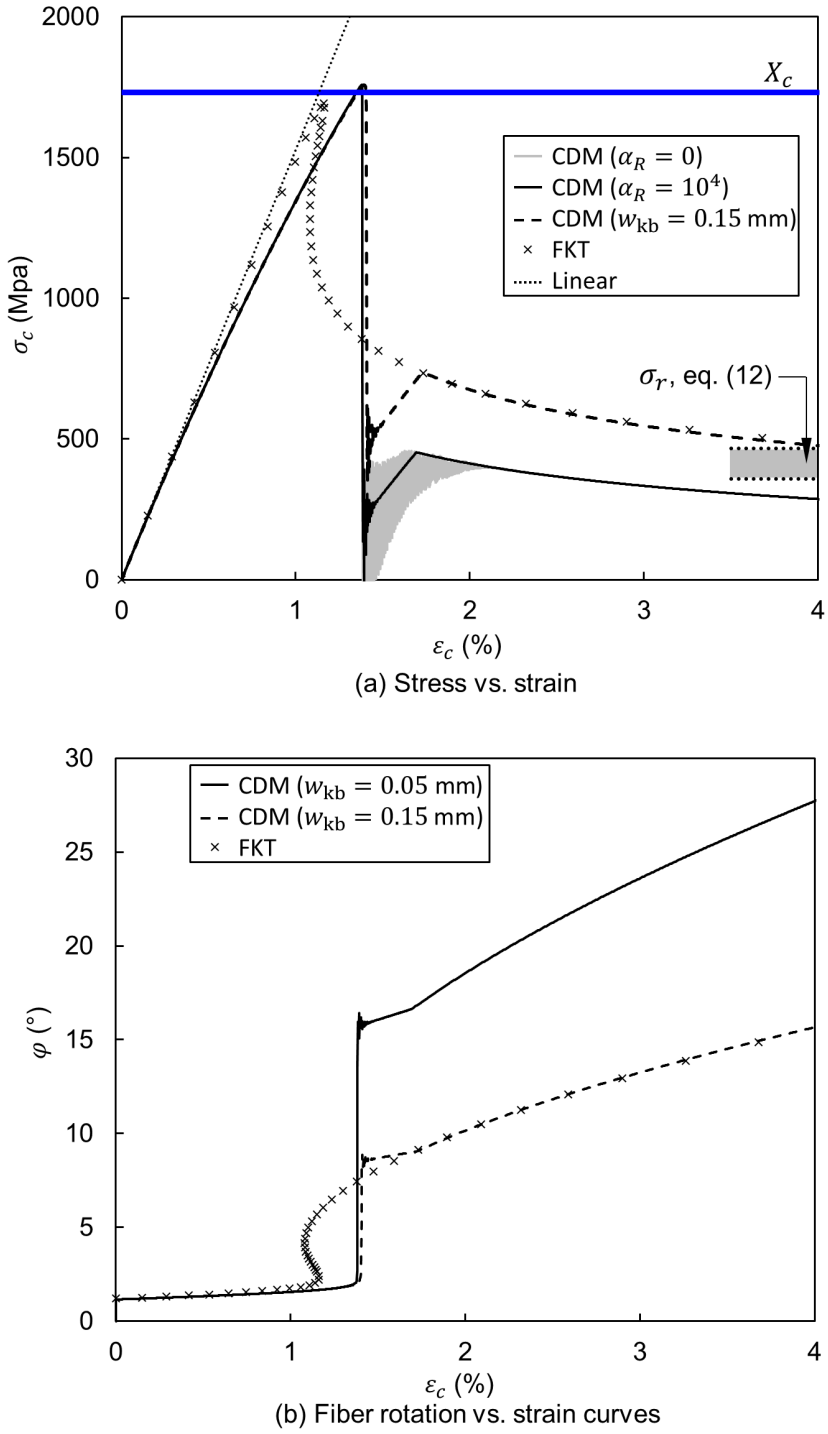

Figure 5. Constitutive response of the mesoscale model obtained from a single element analysis for IM7/8552.

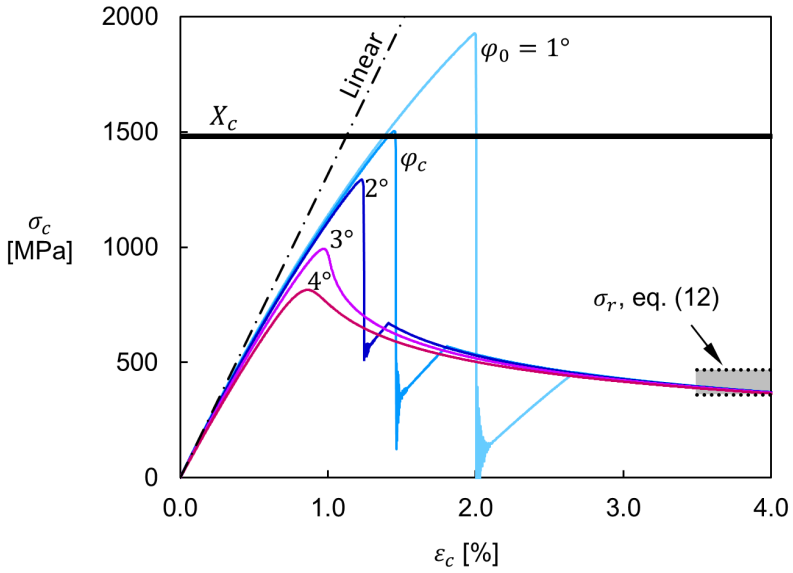

Figure 6. Constitutive response of the mesoscale model obtained from a single element analysis for AS4/8552 showing the effect of different values for φ_0.

shear stress $\tau_L = 95$ MPa (at 5% strain) and $\beta = 12°$ to $16°$ based on experimental measurements [71]. The present model predicts lower residual stress than FKT and eq. (12) when $w_{\text{kb}} = 0.05$ mm. The difference in σ_r is due to $\overline{w}_{\text{kb}} < 1$ in the CDM model. Since w_{kb} and l_1 are not accounted for in FKT, it is only expected that the CDM will agree with FKT for $\overline{w}_{\text{kb}} = 1$. When $w_{\text{kb}} = l_1$ such that $\overline{w}_{\text{kb}} = 1$ (thus, $w_{\text{kb}} = 0.15$ mm in this particular case), the CDM predicts the same residual stress as FKT.

The fiber rotation vs. strain response is shown in Fig. 5b. The current fiber rotation, φ, calculated using eq. (38) shows the initial misalignment at no load leads to slight rotation up to the point where the strength is reached. When the strength is reached, large fiber rotation occurs. The fiber rotation continues to grow as the model approaches the residual stress in the post-peak regime. Again, when $w_{\text{kb}} = l_1 = 0.15$ mm, the CDM predictions are in very good agreement with FKT throughout the loading history. For the realistic value of $w_{\text{kb}} = 0.05$ mm, the model predicts significantly more rotation, which explains the lower σ_r.

The constitutive response described in this section and the accompanying figures is an outcome of the model, not prescribed directly. As a result, the model has the ability to account for several aspects of FKT, such as the relationship between the initial misalignment angle (φ_0), compressive strength (X_c), and residual stress (σ_r).

The dependence of strength on the initial misalignment angle is shown in Fig. 6 for the AS4/8552 material system.[1] The results for $\varphi_0 = 1°$, $2°$, $3°$, and $4°$ are

[1]AS4 fibers are used to show a slightly different material response. The results for IM7 fibers are similar.

shown in addition to the nominal case where $\varphi_0 = \varphi_c = 1.6°$. As in Fig. 5, the strength, initial linear stiffness, and residual stress, eq. (12), are shown in Fig. 6. It is observed that the stiffness and residual stress results are mostly independent of φ_0, which is in good agreement with FKT. Furthermore, the strength is a function of φ_0, with increasing value of φ_0 yielding lower strengths. For the case where $\varphi_0 = \varphi_c$, the strength result from the model is in excellent agreement with the input strength with an error of 1.7%. These results suggest that the model has captured accurately the key features of the FKT.

2.7.2 Verification of the decomposition procedure: two element model

The decomposition approach described in Section 2.4 is verified in this section by comparing the results from the single element model described above to the results from a two element model. Schematic illustrations of the model configurations are shown in Fig. 7. In the single element model, the mesoscale kinking model is applied as described in Section 2.7.1 with the exception that several values for the parameter w_{kb} are considered. The two element model is designed as a reference for comparison to verify the results from the decomposition procedure in the single element model. In the two element model, one element, designated "Element 1" is defined with a length equal to w_{kb} in the X_1-direction. Thus, Element 1 is not decomposed since $\overline{w}_{\text{kb}} = w_{\text{kb}}/l_1 = 1$. The second element, designated "Element 2" is defined with the kinking model disabled and a linear stress-strain response in shear. The two element model was analyzed for the same set of values of w_{kb} as the single element model. Both models used C3D8R elements with an overall length in the X_1-direction of $l = 0.2$ mm and the IM7/8552 material properties defined in Table 4. The expectation of this verification exercise is that the single and two-element models should yield identical results if the decomposition procedure performs as designed.

The comparison of the compressive stress-strain response from the two models for $\overline{w}_{\text{kb}} = 0.4$, 0.5, 0.6, 0.7, 0.8, 0.9, and 1 is shown in Fig. 8. The compressive stress is normalized to the strength for IM7/8552. The results from the single element models are shown with dashed lines and the results from the two element models are shown with solid lines. The results for each value of $\overline{w}_{\text{kb}}$ are given a different color and labeled near the right of the figure. It is observed that the single element and two element model predictions are in excellent agreement for the range of $\overline{w}_{\text{kb}}$ considered. Furthermore, the decomposition and value of w_{kb} only play a role in the post-peak regime. These results verify that the decomposition implementation performs as expected. It is interesting to note that larger values of w_{kb} produce higher values of σ_r (observed in Fig. 5a also), which is a result that is discussed in more detail in Section 4.

While these results verify several aspects of the model, they do not fully demonstrate mesh objectivity. In order to verify mesh objectivity as well as applicability to larger-scale analyses, the mesoscale model is used to analyze an unnotched unidirectional compression specimen in the next section.

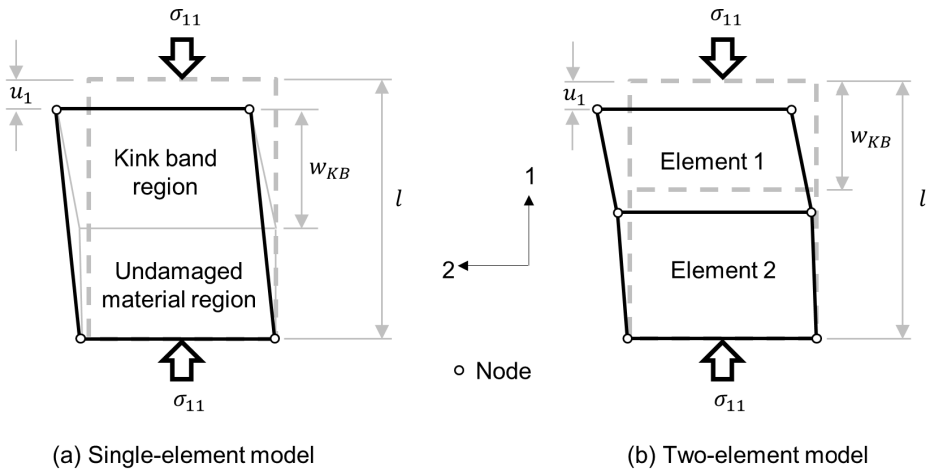

(a) Single-element model (b) Two-element model

Figure 7. Schematic illustration of the models used to verify the kink band decomposition procedure.

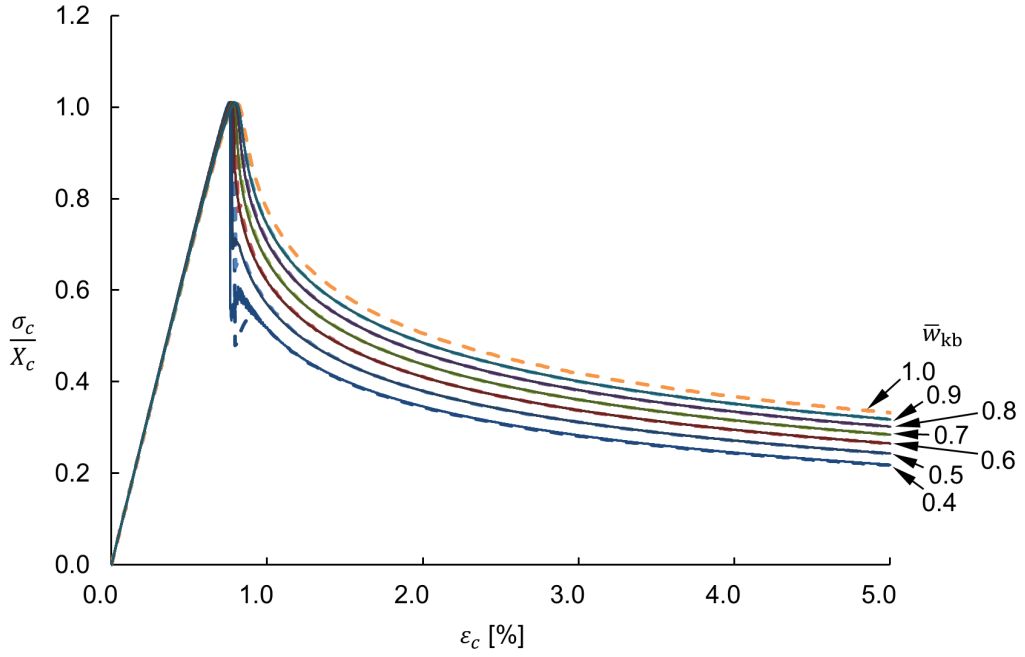

Figure 8. Compression stress vs. strain results for different values of $\overline{w}_{\mathrm{kb}}$ for single-element and two-element models. Dashed curves are single-element model predictions and solid curves are two-element model predictions.

2.7.3 Unnotched compression

The unnotched compression configuration was chosen to resemble the gauge section of test specimens often used to measure the longitudinal compression strength. The unidirectional specimen has a 5-mm width, 14-mm length, and 6 plies for a thickness of 1.1 mm. The IM7/8552 material system was used in the analysis. Damage was disabled in the regions of the specimen near the ends to force failure in the mid-section, as shown in Fig. 9a. The model was meshed with C3D8R elements with enhanced hourglass control enabled. Analyses were conducted with an Abaqus/Explicit step with a duration of 0.1 seconds. Automatic mass scaling was set with a target time increment of 10^{-6} seconds. Three mesh sizes, 0.05 mm, 0.1 mm, and 0.2 mm, were used to assess the mesh objectivity of the model predictions. On the top and bottom faces of the specimen at $X_1 = 0$ and $X_1 = l$, uniform end shortening is applied and displacements in the X_2 and X_3 directions are set to zero, as shown in Fig. 9b. End shortening is applied to both ends as opposed to displacing one end while holding the other fixed to reduce the overall dynamic energy in the model.

A difficulty in the progressive damage analysis of unnotched configurations is the need for a nonuniformity to trigger localization of damage. For fiber kinking, the initial fiber misalignment, φ_0, presents a possibility to achieve a physically based spatial variation that will trigger damage localization in unnotched specimens. Sutcliffe showed the use of random fiber misalignments as an initiation mechanism while studying the role of spatially varying fiber misalignments using a 2D plane strain finite element model [31,32]. It should also be recognized that if fiber misalignments in all elements are the same, an overall shearing occurs when the coupon is compressed due to the anisotropy induced by the misalignment. Such a response is a departure from reality since measured fiber misalignments have a random distribution with a mean misalignment near zero [81, 82]. While implementation of a 2-D or 3-D spatial variation of initial fiber misalignments is possible (although complex) using experimental measurements available in the literature [57, 83], a simple 1-D implementation is used herein. A 1-D variation of fiber misalignments has the advantages of simplicity and consistency with Budiansky's infinite band assumption, which is useful for verification. Thus, a uniform random distribution of fiber misalignments in the interval $[-\varphi_c, \varphi_c]$ is applied, where eq. (26) and the properties in Table 4 are used to obtain $\varphi_c = 1.15°$. The initial misalignment angle is assumed to vary only as a function of the longitudinal position, $\varphi_0^i = \varphi_0^i(x)$ where φ_0^i represents the initial misalignment distribution in the model, which is consistent with Budiansky's assumption. No wavelength is associated with the fiber misalignment. One realization of fiber misalignments used for verification is shown in Fig. 9c for $l_1 = 0.2$ mm. The location of the most severe misalignment, where a large positive misalignment is adjacent to a large negative misalignment is denoted with a black arrow. All realizations satisfy $\max(|\varphi_0^i|)/\varphi_c \geq 0.97$ and so it can be expected that the analysis should reproduce the input strength, X_c.

The normalized applied stress, σ_c/X_c, versus end shortening, Δ, results are shown in Fig. 10a. It is observed that the model reproduces the strength accurately with all three element sizes. Without element deletion, the analysis crashes at the peak load due to excessive mesh distortion. Using element deletion with the

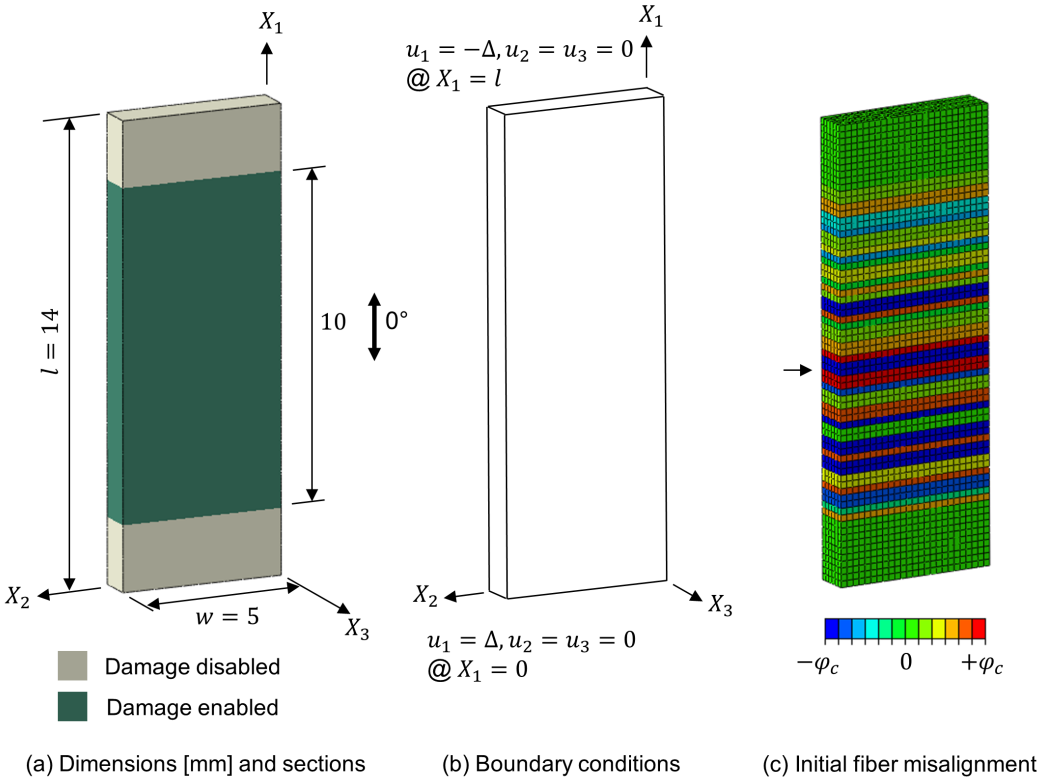

(a) Dimensions [mm] and sections (b) Boundary conditions (c) Initial fiber misalignment

Figure 9. Unnotched compression specimen for $l_e = 0.2$ mm.

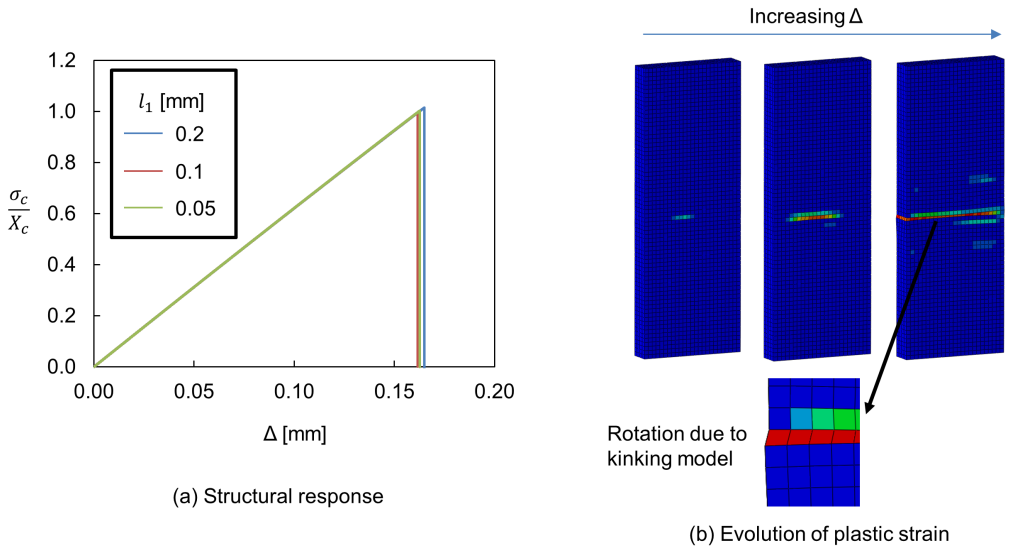

(a) Structural response (b) Evolution of plastic strain

Figure 10. Mesoscale model results for the unnotched compression specimen.

Table 5: Element deletion tolerances used in UNC analysis.

F_{TOL}	$n_{\max}$	γ_{TOL}
0.25	10^4	400%

tolerance values provided in Table 5 enables capturing the load drops shown in Fig. 10. It is noted that the tolerance values for element deletion are set to very large values and are only satisfied for very distorted elements. Therefore, the element deletion scheme is nothing more than a numerical convenience for this particular analysis. A better representation of the physical reality would require consideration of contact, which is beyond the scope of this work. The evolution of plastic strain just before collapse is shown in Fig. 10b and indicates that damage localizes in the band of elements where the most severe initial misalignment is located (as identified in Fig. 9c) and rapidly propagates across the width of the specimen in a direction corresponding to a kink band angle $\beta = 0$, which is consistent with the formulation of the model. The fiber rotation associated with the kink band is evident in the deformed mesh.

The unique relation between strength and φ_c given in eq. (5) may lead to the conclusion that a spatial distribution of φ_0 is no different from spatially distributing strength. However, it should be recognized that fiber misalignment measurements can be used to introduce a length scale associated with the wavelength of misaligned fibers. Although not addressed here, a length scale for material variability seems likely to be an important feature for overcoming the limitation of random distributions where strong elements neighboring weaker elements prevent damage propagation, especially when considering 2-D and 3-D spatial variations. Furthermore, as demonstrated by Wisnom [68], the spatial variation of misalignments has an important constraining effect where gradients in misalignment arrest rotation of the most severely misaligned fibers so that the strength is a function of the average misalignment instead of the maximum misalignment. These features should be accounted in future works in order to predict accurately longitudinal compression failure.

2.8 Summary of the mesoscale model developments

The mesoscale model described in this section is intended for use in prediction of failure in composite structures from the coupon scale to the component scale. The verification problems discussed in this section are a first step towards this goal. As a result of the requirement to scale up to large structures, several assumptions are made in the mesoscale model for both compatibility with existing progressive damage analysis techniques used to model matrix damage modes and for computational efficiency. In order to assess how well the mesoscale model captures the mechanisms of the fiber kinking process, a detailed micromechanical model is used. The micromechanical model is described in the following section.

3 Computational Micromechanics Model

A 3-D single-fiber computational micromechanics (CMM) model is used to assess the relative significance of various features and assumptions of the relatively coarse mesoscale model in order to improve the understanding of the mechanics of the fiber kinking process. In this section, the micromechanical finite element model is described including the geometry, discretization, and material properties. Experimental measurement and calibration undertaken to define some of the most critical material properties are described. This section concludes with verification examples that demonstrate the behavior of the CMM model.

3.1 3-D RVE for fiber kinking

During the last three decades, a variety of micromechanical models have been developed to represent the fiber kinking process. The aim of this work is to study the initiation and evolution of the fiber kinking process, including kink band residual stress [8, 25] in the post-failure regime. As such, there is no need to use a multiple-fiber model that could capture kink band propagation. Instead, a single-fiber 3-D model with periodic boundary conditions is employed based on [63], as shown in Fig. 11.

The model represents a 3-D single carbon fiber extruded in the longitudinal direction, z, along the half wavelength of a sine curve of length L, with an initial misalignment, φ_0

$$y(z) = L\ \frac{\varphi_0}{\pi} \cdot \left(1 - \cos\left(\pi \frac{z}{L}\right)\right) \tag{47}$$

Due to the anisotropic behavior of the carbon fiber, material orientations were defined according to the local misalignment along the fiber axis according to

$$y'(z) = \varphi_0 \cdot \sin\left(\pi \frac{z}{L}\right) \tag{48}$$

as shown in Fig. 11.

The fiber diameter was d and a fiber volume fraction $V^f = 60\%$ was assumed, leading to a square RVE of side length $w = d/2\ \sqrt{\pi/V^f}$. The model is discretized using finite elements in Abaqus/Standard [65]. Both, the matrix and the fiber are modeled with 8-node fully integrated isoparametric elements (C3D8). The in-plane mesh size is set such that there are six elements along the fiber diameter. In the longitudinal direction the element edge length is 10 µm and the model length is $L = 500$ µm. The partitions in the longitudinal direction are normal to the fiber axis to guarantee a good quality of the finite elements regardless of the initial fiber misalignment, as shown in Fig. 11.

A single-fiber model requires special definition of boundary conditions, as free boundaries would promote Euler buckling of the fiber, and the predicted strength would largely underestimate the strength of the composite. Periodic boundary conditions (PBC) appear to provide the most adequate solution. By comparing a single fiber model to a model with 100 fibers, Gutkin et al. [57] showed that PBC can be applied on single-fiber models for longitudinal compressive strength prediction (X_c)

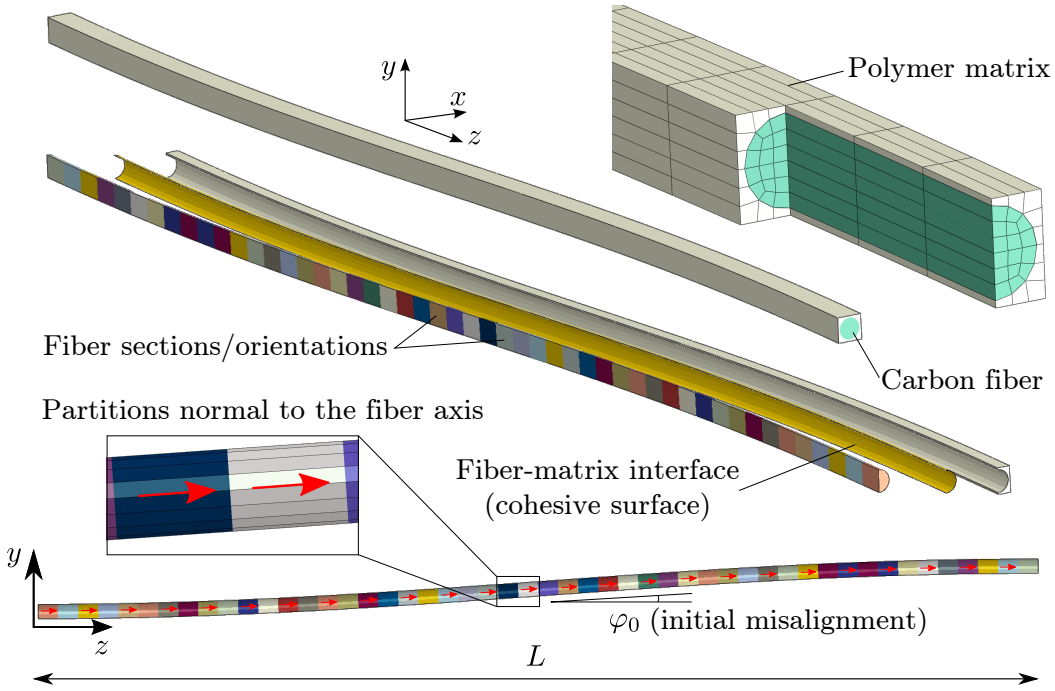

Figure 11. Illustration of the single-fiber 3-D CMM, detail of the mesh, exploded cut view of the model, and side view with detail of the longitudinal mesh and material orientation.

at the expense of inducing $\beta = 0°$. PBC are applied on the lateral faces of the model, while the model ends are subjected to isostrain conditions to introduce the longitudinal compressive load. PBC are imposed between opposite faces of the model such that $\vec{u}_i - \vec{u}_{i'} = \vec{u}_{\mathrm{MN}}$, where i and i' are twin nodes of opposite faces and MN is the master node governing the corresponding pair of faces' relative displacement. Preliminary analysis showed the ability of PBC combined with the partitions normal to the fiber direction, to achieve a meaningful representation of the fiber kinking mechanism (see Section 3.5).

A homogeneous thermal step with a temperature drop, ΔT, was applied without external loading prior to the loading step to consider the residual thermal stresses induced by the cool down from the curing temperature. This thermal step induces a residual thermal stress field as a result of the mismatch between the thermo-elastic constants of fibers and matrix. The magnitude ΔT is not easily determined since the residual stresses accumulate nonlinearly during the cool down. As a result, the value used for ΔT is determined as described in Section 3.4.

3.2 Material models for the fiber, matrix, and interface

The carbon fiber was modeled as a transversely isotropic material considering elastic nonlinearity and inelastic damage. Elastic nonlinearity of carbon fibers in the longitudinal direction is reported in the literature [84] and typically the longitudinal

elastic modulus is modeled as a linear function of the longitudinal strain [67,78,85] as considered herein with

$$E_1^f = E_1^{0f}(1 + c^f \varepsilon_{11}) \tag{49}$$

where c^f is the nonlinear parameter of the fiber and E_1^{0f} is the tangent modulus at $\varepsilon_{11} \to 0$.

Fiber failure is given by a maximum stress criterion either in longitudinal tension, $\sigma_{11}^f \geq X_t^f$, or compression, $|\sigma_{11}^f| \geq X_c^f$ and subsequent damage based on a CDM scheme [86]. The details of the numerical implementation of the user subroutine for the carbon fiber constitutive behavior can be found in Appendix B.

The thermoelastic constants of the carbon fibers analyzed are reported in Table 6. The longitudinal strengths, X_t^f and X_c^f, and the nonlinear parameter, c^f, were determined using novel tests, which are described and reported in Section 3.3 (numerical values are given in Table 9). The experimental procedure to characterize the fiber nonlinearity is described in Section 3.3.1. AS4 fiber tensile strength was obtained from single-fiber tensile tests, whereas the longitudinal compressive strength of AS4 carbon fiber was experimentally measured from in-situ microtests as shown in Section 3.3.2. The compressive strength of IM7 fiber was obtained from the literature [57].

The polymer matrix behavior is represented using the Lubliner damage-plasticity model included in Abaqus [65, 87]. This constitutive equation allows the material to behave as quasi-brittle when subjected to dominant tensile stress and models elasto-plastic behavior under pressure confinement and compressive loads. Hence, the tensile response is linear and elastic with elastic modulus and Poisson ratio, E^m and ν^m, until the tensile failure stress, $\sigma_{t_0}^m$, is reached. Beyond this point, a quasi-brittle softening is induced in the material, with G_t^m being the matrix fracture energy. Under uniaxial compression, the response is linear up to the initial yield limit, $\sigma_{c_0}^m$. Then, the matrix strain hardens until the ultimate stress value, $\sigma_{c_u}^m$, is reached. Finally, the model includes a dilation angle, ψ^m, which couples dilatancy with deviatoric deformation. The matrix was characterized by *in-situ* instrumented nano-indentation as described by Rodríguez et al. [88]. The material model parameters used in the simulations are reported in Table 7 [89,90]. The dilation parameter, ψ^m, was not obtained in the experimental characterization, so it was determined using the calibration procedure described in Section 3.4.

Fiber-matrix interface failure is taken into account using a cohesive crack approach. To this end, a cohesive interaction between the fiber and the matrix surfaces is governed by a mixed-mode traction-separation law where damage onset follows a

Table 6: Material properties of linear elastic model of AS4 and IM7 carbon fibers.

Fiber	d [µm]	E_1^f [GPa]	E_2^f [GPa]	ν_{12}^f	ν_{23}^f	G_{12}^f [GPa]	G_{23}^f [GPa]	α_1^f [K^{-1}]	α_2^f [K^{-1}]
AS4 [91]	7.2	Table 9	12.97	0.3	0.46	11.3	4.45	-0.9 10^{-6}	7.1 10^{-6}
IM7 [57]	5.1	Table 9	11.9	0.3	0.49	11.6	3.97	-0.6 10^{-6}	5.2 10^{-6}

Table 7: Parameters of the damage-plasticity model for the matrix [89, 90].

E^m [GPa]	ν^m	α^m [K^{-1}]	$\sigma^m_{t_0}$ [MPa]	G^m_t [J/m^2]	$\sigma^m_{c_0}$ [MPa]	$\sigma^m_{c_u}$ [MPa]
5.07	0.35	52 10^{-6}	121	90	176	180

quadratic stress criterion [65]

$$\left(\frac{\langle t_n \rangle}{N^c}\right)^2 + \left(\frac{t_s}{S^c}\right)^2 + \left(\frac{t_t}{S^c}\right)^2 = 1 \tag{50}$$

where $\langle\ \rangle$ stands for Macaulay brackets defined as $\langle x \rangle = \max(0, x)$, t_n is the normal traction and, t_s and t_t are the shear components of the traction vector. N^c is the normal strength and S^c is the shear strength assumed to be equal in both shear directions s and t. In addition, mixed-mode damage evolution is governed by a Benzeggagh-Kenane law [92] as

$$G^c = G^c_n + \left(G^c_s - G^c_n\right) \cdot \left(\frac{2G_s}{G_n + 2G_s}\right)^{\eta_{\mathrm{BK}}} \tag{51}$$

where η_{BK} is the Benzeggagh-Kenane power exponent, G^c_n and G^c_s are the normal and shear fracture energies respectively, and G_n and G_s are the reciprocal work under mixed mode propagation. Isotropic coulomb friction, ξ^c, is enabled at cohesive damage initiation after cohesive failure is included in the cohesive contact definition. The fiber-matrix interface parameters used in the simulations are presented in Table 8. It should be noted that interface properties were estimated based on the calibration of the in-plane shear model described in section 3.4, but are in agreement with experimental values reported in the literature [90]. Nevertheless, some of the mechanical properties of the fiber/matrix interface have never been experimentally measured, such as the normal strength (N^c) or the fracture energies ($G^c_n,\ G^c_s$), so they need to be estimated or calibrated [93]. Together with the mechanical properties of the matrix, interface properties also play a major role on the initiation and evolution of the fiber kinking phenomenon, as it will be shown in section 5.

Table 8: Material properties of fiber-matrix interface based on the calibration of the shear model in section 3.4 and [90].

N^c [MPa]	S^c [MPa]	k^c_n [GPa/µm]	k^c_s [GPa/µm]	G^c_n [J/m^2]	G^c_s [J/m^2]	η_{BK}	ξ^c
57	85	100	100	7	81	1.2	0.4

3.3 Experimental characterization

Experimental investigations were conducted to characterize several of the critical input properties of the CMM model as described in this section.

3.3.1 Carbon fiber non-linear elastic behavior

Various authors have reported the difference in elastic moduli of carbon fibers under tensile and compressive loading, e.g. [6]. Under tensile load, fibers become gradually stiffer until the tensile strength is reached, X_t^f, while in compression the modulus decreases until a critical compressive stress, X_c^f, is reached. This phenomenon is clearly observed in fibers under pure bending where the neutral axis shows an offset from the middle of the fiber cross section [94, 95]. The reduction in the compressive modulus with increasing compressive strain is explained on a microstructural basis by the local buckling of carbon crystallites promoted by the presence of needle-like pores [96]. This phenomenon is observed as elastic nonlinearity at the ply scale. For instance, the linear elastic modulus of CFRP was measured experimentally by Mujika [97] through a four point bending test carried out on a unidirectional laminate of AS4/8552, and showed a ratio of compressive to tensile moduli of 0.9. Nonlinear elastic response in the fiber direction of CFRP thin plies was observed experimentally by [78, 85] and modeled with a variable elastic modulus as shown in eq. (23).

Single-fiber tensile tests were performed on AS4 carbon fibers to obtain the stress-strain curve up to failure. Carbon fibers were first extracted carefully with mechanical tweezers from tows previously separated from woven fabrics. Special care was taken to avoid damage while handling and mounting fibers for testing. The fiber ends were bonded with cyanoacrylate adhesive on cardboard with 20 mm free-gauge length. A total of 70 fibers were tested to characterize the elastic nonlinearity parameters and the tensile strength. The ends of the fibers were directly connected to the mechanical grips of the tensile tester and then submitted to uniaxial straining up to failure under stroke control at 1 mm/min, leading to strain rates on the order of $\sim 10^{-3}\ s^{-1}$. The linear density of the fibers was determined by the fiber tester system through the frequency method according to the ASTM D1577 standard [98]. In this method, the fiber is pre-stressed to a given force in the range of 0.45-0.70 cN/tex. Then, the natural frequencies are extracted to determine the linear density and, subsequently, the cross-sectional area. These latter values were used to determine the individual tensile stress and strength of each fiber tested. As a uniaxial loading state, the longitudinal stress, σ_{11}, is obtained by integrating the elastic modulus in eq. (49) along the longitudinal strain, resulting in

$$\sigma_{11}(\varepsilon_{11}) = E_1^{0f} \cdot \left(\varepsilon_{11} + \frac{c^f}{2} \cdot \varepsilon_{11}^2 \right) \tag{52}$$

The red curves shown in Fig. 12 were obtained from single-fiber tensile tests of AS4 carbon fibers. Assuming that the nonlinearity can be defined by the same c^f parameter in tension and compression, the blue curves correspond to the extrapolation of the tensile side, previously fitted by means of eq. (52). The least squares fit of all the test data is plotted as the green curve with the following parameters: $E_1^{0f} = 211.5$ GPa and $c^f = 18.7$. The black line illustrates the elastic modulus from the traditional linear fitting, E_1^f. The compressive side curves are extended up to $\varepsilon_{cu}^f = -\varepsilon_{tu}^f$ just to illustrate the modulus loss during longitudinal compression. IM7 carbon fibers were not tested for availability reasons, so the ply-scale nonlinear

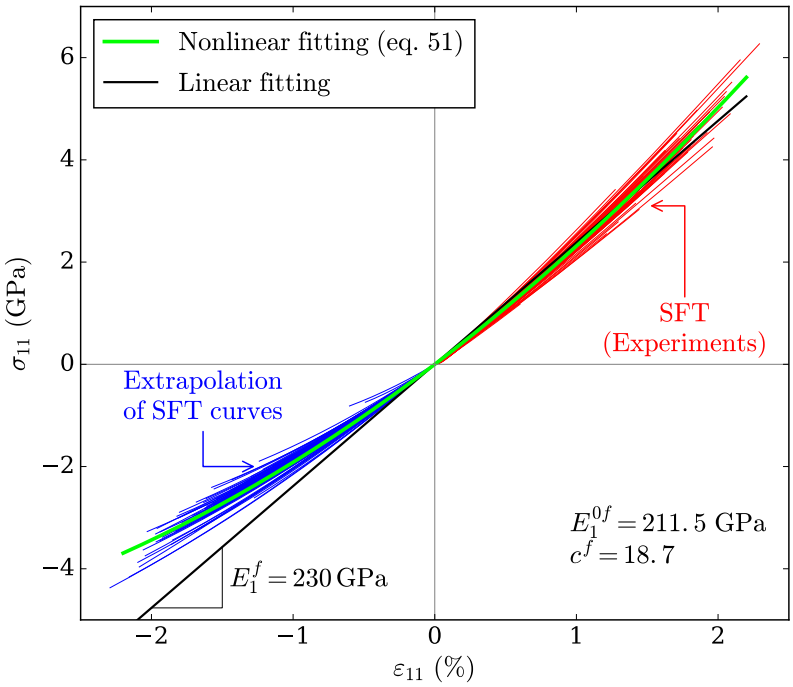

Figure 12. Stress-strain curves from single-fiber tests of AS4 carbon fibers and nonlinear fitting.

parameter from the literature, c^l [78], was scaled by means of the rule of mixtures to estimate the nonlinear parameter of the fiber, $c^f = c^l/V^f = 16.7$, and the initial elastic modulus was scaled with the modulus obtained for AS4 fibers resulting in $E_1^{0f} = 256$ GPa.

3.3.2 Fiber compression strength

A number of experimental techniques have been developed to measure the compressive strength of carbon fibers [6] including (i) the elastic loop test [99], (ii) the fiber recoil method [100], (iii) single fiber composites testing [101], (iv) bending of a micro-beam [102–104], and (v) direct fiber compression [96, 105]. In the elastic loop test (i) a fiber is bent into a loop and the ends of the loop are pulled until the fiber breaks. Although this method was originally developed as a means of determining the tensile strength of fibers [106], the compressive stress in the loop may induce compressive failure of the fiber first. The fiber recoil method (ii) was introduced by Allen [100] for the measurement of the compressive strength of polymeric fibers. This technique consists of stretching a fiber at a certain tensile stress and then cutting it in the middle. The resulting wave from the cut travels to the fixed ends of the specimen and is reflected inducing a compressive stress state along the fiber. The initial tensile stress is increased consecutively until damage is observed in the

fiber cut ends. This procedure is prone to induce buckling along the fiber as large gauge lengths are required and interpretation of the results is not direct. Hawthorne and Teghtsoonian [101] carried out uniaxial compression tests on single-carbon fiber epoxy composites (iii). They found an inverse relation between the elastic modulus and compressive strength of the carbon fibers, as occurs in longitudinal tension for rayon-based and PAN-based fibers. Compressive failure stress ranged from 0.8 to 2.5 GPa. The bending method includes different configurations to induce compressive loading in single fibers (iv). DeTeresa et al. [102] employed a cantilever beam-like design to induce a linear strain distribution along the beam-fiber until the fiber was damaged. A different scheme was taken by other authors [103, 104] setting up a single-fiber four point bending test producing a region of constant strain in carbon fibers. Direct compression of single carbon fibers (v) was accomplished by Macturk et al. [105] by fixing the fiber ends to the loading fixture with a gauge length of 200 µm. It was found that the fiber compressive strength determined using this method is sensitive to the fiber gauge length: if the fiber is too long it will buckle, while if it is too small the stress field will not be homogeneous and the strength measurement will be affected by the boundary conditions. Oya et al. [96] performed a similar test to measure the compressive strength of different types of carbon fibers and found the fixtures had an important effect on the fiber failure.

In this study, a novel technique for the compressive strength characterization of carbon fibers is presented. Longitudinal compressive strength of AS4 carbon fibers was measured through *in situ* micropillar compression tests. A FEI Helios NanoLab DualBeam 600i equipped with a Focused Ion Beam (FIB) was used to manufacture micropillars at the center of carbon fibers on the composite cross section (Fig. 13a). Pillars of 1.5 µm in diameter (d_p) and 3 µm in height (h_p) were fabricated using annular milling which resulted in pillars with a taper angle ($\theta \leq 3^\circ$) as shown schematically in Fig. 14a. Beam currents were selected in order to produce suitable pillar geometries while keeping reasonable milling times, starting with an initial current of 0.79 nA down to 80 pA for the last milling step. The pillar diameter must be sufficiently small compared to the fiber diameter such that pillar collapse occurs before fiber-matrix debonding due to the shear stress induced at the interface.

Samples were then mounted on a special holder for easy transfer between the FIB and the nanoindenter instrument. Compression tests were conducted using a Hysitron TI 950 TriboIndenter equipped with a 10 µm diameter flat punch. The experiments were carried out under displacement control at a constant displacement rate of 12 nm/s. Considering the height of the pillars was around 3 µm, the test speed guarantees quasi-static conditions ($\dot{\varepsilon} \approx 10^{-3}$ s^{-1}). A total of 13 fiber pillars were milled along the composite cross section and tested.

Typical stress-displacement curves obtained during the compression tests are plotted in Fig. 14b. All curves present the same features distinguishing three different regions. The initial nonlinear region corresponds to the contact stage between the indenter punch and the top face of the pillar, followed by a linear region during elastic deformation of the fiber pillar and the surrounding material. This second stage turns into a smooth softening of the stiffness promoted by fiber pillar splitting. Fiber compression strength is computed at this point, and is indicated by the red crosses in Fig. 14b. The splitting phenomenon was barely visible using the

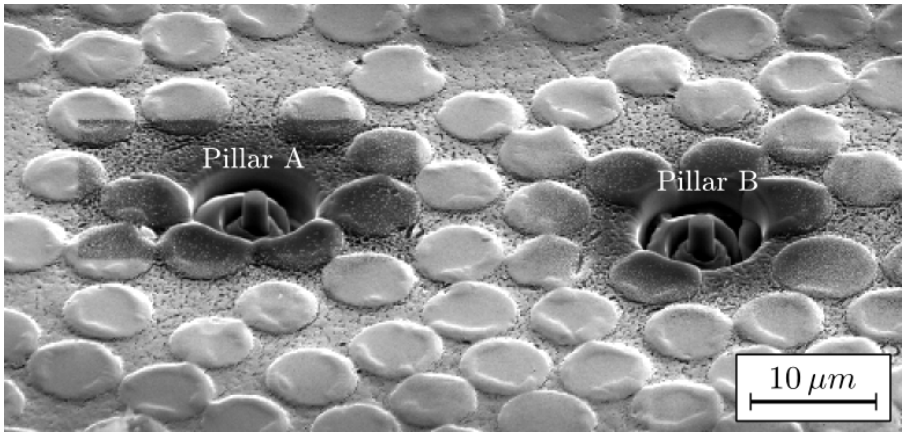

(a) Cross-section view of an AS4/8552 composite lamina

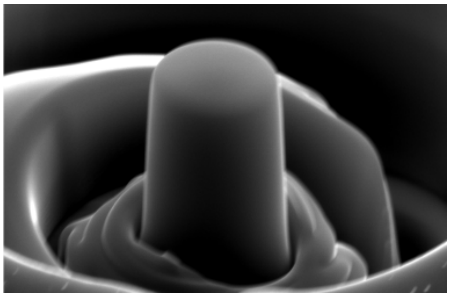

(b) Pillar A (pre-mortem)

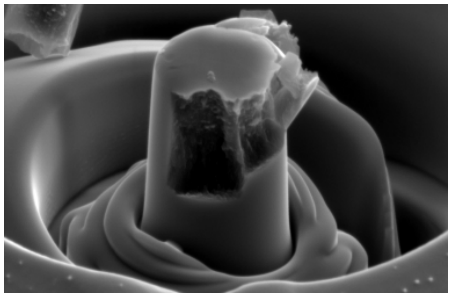

(c) Pillar A (post-mortem)

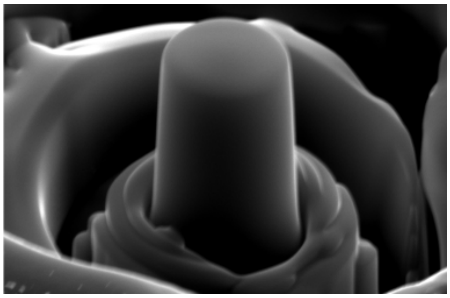

(d) Pillar B (pre-mortem)

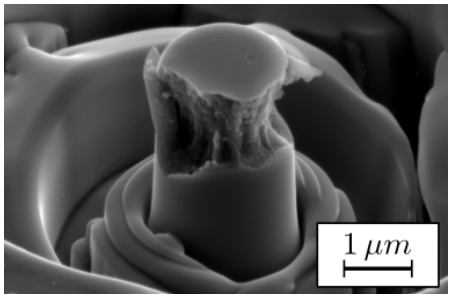

(e) Pillar B (post-mortem)

Figure 13. Pre and post-mortem views of two micropillars milled on AS4 carbon fibers.

SEM. If the load keeps increasing, eventual collapse of the micropillar takes place due to the transverse tensile stresses generated within the bulk of the pillar as in a Brazilian disc test of concrete, see Fig. 13(c) and Fig. 13(e). These images confirm fiber push-in phenomenon is prevented in favor of micropillar compression up to failure.

The pillar compressive strength was obtained based on the loss of linearity of the loading curve as in [107]. The stiffness of the system, k_0, was computed through least squares fitting of the linear stage of the curve. Then, this linear fitting was shifted to the right ($\Delta u = 2\%$) and the compressive strength of the fiber, X_c^f, was

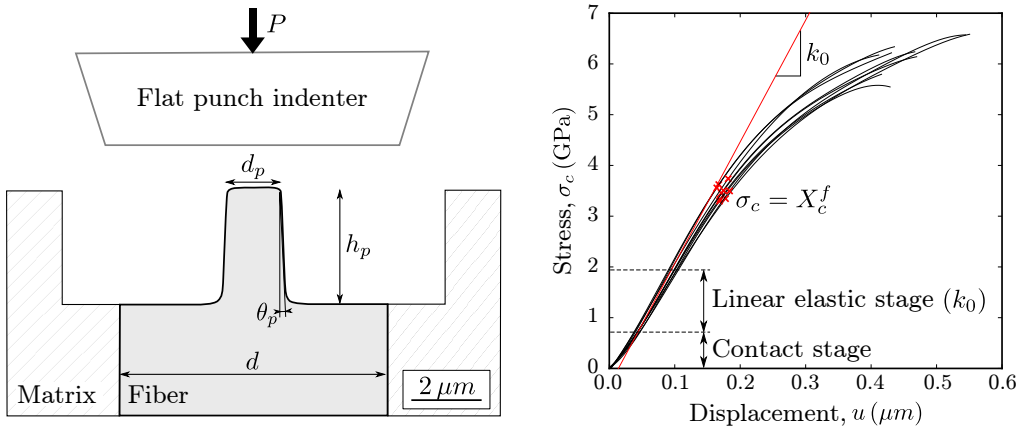

(a) Schematic view of the microtest

(b) Stress-displacement curves

Figure 14. Pillar compression test for compressive strength characterization of AS4 carbon fibers (red crosses denote initial fiber failure).

computed as the intersection between this line and the loading curve. The value of the displacement offset, Δu, was somewhat arbitrary, but provided good and repeatable estimations for the critical load at damage onset. This technique might be applied to other kind of fibers like glass, basalt, aramid, and poly-ethilene. As the micropillar milling requires minimal electrical conductivity of the sample, a common surface treatment, like gold sputtering, is enough for imaging purposes.

The average compressive strength obtained for AS4 carbon fibers was 3500 MPa with a standard deviation of 200 MPa. IM7 carbon fibers were not tested for availability reasons, therefore, the compressive strength value shown in Table 9 was obtained from the literature [57].

Table 9: Longitudinal properties of carbon fibers for the linear and nonlinear cases.

Fiber	Linear		Nonlinear			
	E_1^{0f} [GPa]	c^f	E_1^{0f} [GPa]	c^f	X_c^f [MPa]	X_t^f [MPa]
AS4	230	0	211.5	18.7	3500	4000
IM7 [57,78]	275	0	253	18.3	3200	5000

3.4 In-plane shear response

The mesoscale model requires the non-linear stress-strain relation under in-plane shear loading, $\tau_{12} = \tau_{12}(\gamma_{12})$, to derive the compressive strength of the composite. Ideally, the parameters that define the shear response of the ply are obtained from an experimental test that isolates the behavior of a single ply subjected to large shear deformations. However, in the absence of such test data, the ASTM D3518 test of a $\pm 45°$ laminate subjected to longitudinal tensile loading [108] is used to define the shear nonlinearity behavior. The $\pm 45°$ laminate test data smears a wide variety of damage mechanisms into a single stress-strain curve, including mechanisms

such as large fiber rotations and delamination, which are not desirable to include in the shear nonlinearity characterization. Nonetheless, the $\pm 45^\circ$ laminate is the best source of material input data available for the mesoscale model. Therefore, the micromechanical model was calibrated, in a similar fashion to the approach proposed by Yerramalli and Waas [18, 56], so that the RVE model produces an equivalent shear stress-strain response using a $\pm 45^\circ$ RVE. This approach facilitates a one-to-one comparison of the mesoscale and micromechanical models for the fiber kinking mechanism.

An RVE of a $\pm 45^\circ$ laminate, as shown in Fig. 15a, was developed with the parameters and modeling approach described in Sections 3.1 and 3.2. Under in-plane shear loading, the model is initially linear elastic until the interface begins degrading and plastic shear deformation of the matrix take place. Fig. 15b depicts the longitudinal fiber/matrix debonding (interface damage, D^c) and the maximum principal plastic strain of the matrix (ε_I^p) for high shear strains in the model ($\gamma_{12} \approx 6\%$). The two undefined input parameters, the dilation angle of the matrix, ψ^m, and the effective temperature drop, ΔT, were adjusted by trial-and-error to reproduce the experimentally measured stress-strain response. The final response produced from the $\pm 45^\circ$ micromechanical RVE, and the experimentally measured response of a $\pm 45^\circ$ laminate are nearly identical as shown in Fig. 15c. The parameters for the Ramberg-Osgood curves used to reproduce the experimental shear curve of the laminate are found in Table 4.

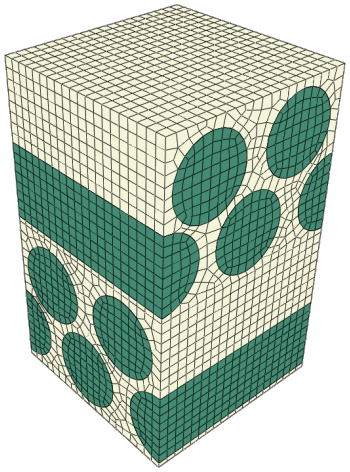

(a) RVE of a $\pm 45°$ laminate model

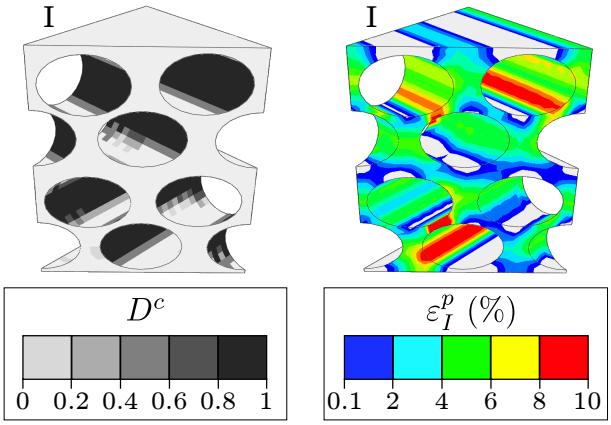

(b) Cut views of the RVE model displaying the damage of the interface (D^c) and the plastic strain field in the matrix (ε_I^p) at point I (see c)

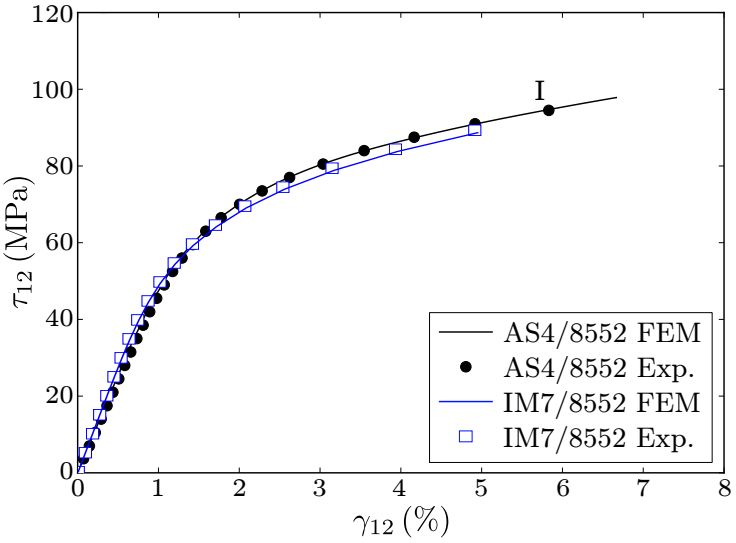

(c) Shear stress-strain curves: experimental and numerical

Figure 15. Numerical characterization of the non-linear shear response of the composite materials (AS4/8552 and IM7/8552). Experimental curves in c) are obtained from the literature for AS4/8552 [79] and IM7/8552 [80].

3.5 Model verification

This section describes several analyses that verify the CMM modeling parameters and demonstrate the characteristics of the model predictions. In this section, the behavior of the fiber is assumed as linear and elastic ($c^f = 0$) without damage consideration and the initial fiber misalignment is $\varphi_0 = 1.5°$.

3.5.1 Verification of model parameters

Verification studies were conducted to investigate the influence of the model length, element size, and periodic boundary conditions for the CMM model. These analyses were carried out for an AS4 carbon fiber.

To analyze the effect of the boundary conditions on the model representativity, two models were compared. The first model consists of the single-fiber model with periodic boundary conditions described at the beginning of Section 3. The second model consists of a vertical array of 3-D fibers extruded along a sine curve as in the single-fiber model, eq. (47), but in this case periodic boundary conditions are only on the lateral faces $x = 0, w$ of the model; the top and bottom faces are free [53,54,62]. An increasing number of fibers was considered in this latter model ranging from 50 up to 400. A schematic representation of the model is presented in Fig. 16a.

A 2-D model was also developed for comparison purposes, as shown in Fig. 16b, based on the work of other authors in the literature [7, 54, 59, 109]. Nevertheless, since the shear response was calibrated using a 3-D micromechanical model, the equivalence with a 2-D model is not guaranteed.

The results indicate that the predictions obtained with the single and multiple-fiber models for compressive strength are in good agreement with FKT, as shown in Fig. 17a. As the number of fibers increases in the multiple-fiber models, the

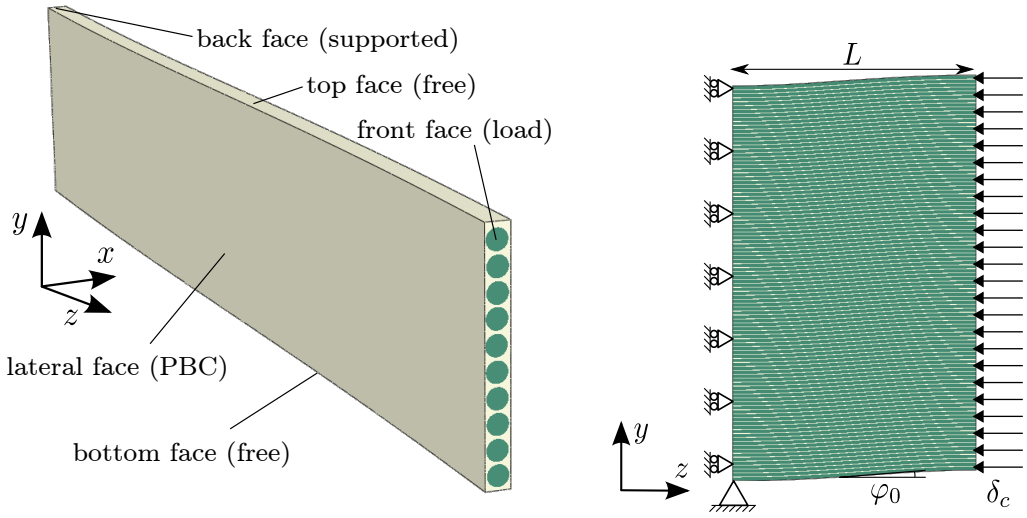

(a) Multiple-fiber 3-D model with 10 fibers (b) Multiple-fiber 2-D model

Figure 16. Schematic representation of the multiple-fiber FE models.

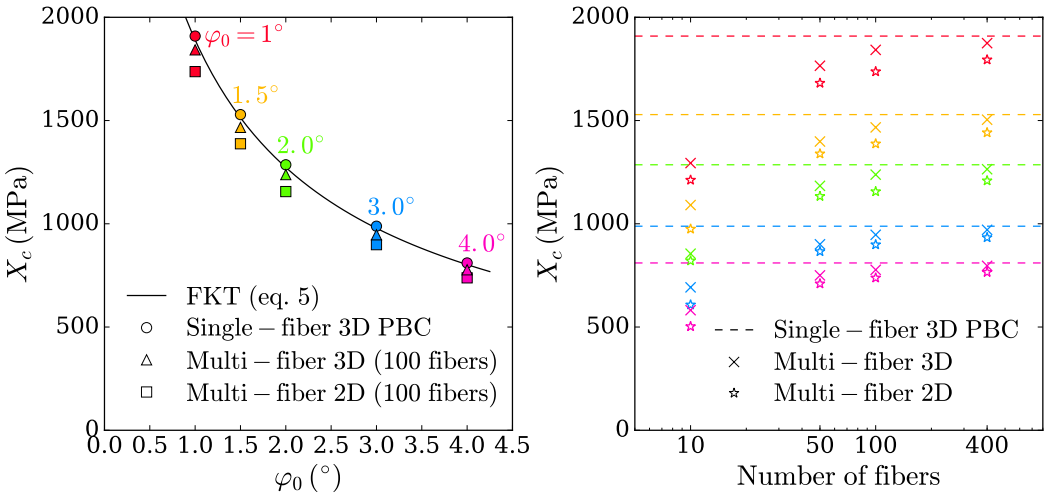

(a) Sensitivity curves (b) Effect of the number of fibers

Figure 17. Analysis of the multiple-fiber models comparing the numerical results from different FE models with the analytical solution from FKT, eq. (5).

strength approaches the strength predicted by the single-fiber model, as shown in Fig. 17b. The limiting case of an infinite number of fibers is equivalent to the single-fiber model with periodic boundary conditions, which is in excellent agreement with FKT.

The model length effect was assessed by analyzing single-fiber 3-D models with the following length values: 200, 300, 500, 700, 800 and 1000 µm. The longitudinal mesh size was kept constant at 10 µm and linear elastic behavior of the fibers was considered. The stress-strain curves for $\varphi_0 = 1.5°$ with the different length values are shown in Fig. 18a. A convergent trend towards the strength predicted by FKT is observed in Fig. 18a as the model length increases. The error between the CMM and FKT for strength is below 2% for $L \geq 500$ µm. The maximum fiber rotation in the CMM model takes place at $z = L/2$ and is denoted as $\varphi^{\max}$. The average rotation of the kinked fiber is calculated from the transverse deflection at the end of the fiber, u_y, and the kink band width, w_{kb}, as $\varphi^{\text{avg}} = \tan^{-1}(u_y/w_{\text{kb}})$. Comparing the kink band rotation in Fig. 18b, the kinematic behavior is equivalent regardless of the fiber length. In Fig. 18c, it is observed that the kink band width at fiber kinking initiation was very similar for all the model lengths analyzed, around 100 µm. The maximum band broadening increases with the model length, as the fiber is longer and fiber failure, which may limit band broadening, is not considered in these analyses. Nevertheless, the relative kink band size is identical in all cases, $w_{\text{kb}}/L = 0.7$, as shown in Fig. 18d. These results show that the kink band width at initiation does not depend on the length of the model, L, but the band broadening once the kink has formed is affected by the far-field boundary conditions.

Based on these analyses, the single-fiber 3-D model with periodic boundary conditions and $L = 500$ µm was selected as the most suitable and representative model to analyze the fiber kinking phenomenon in terms of stress-strain curve and

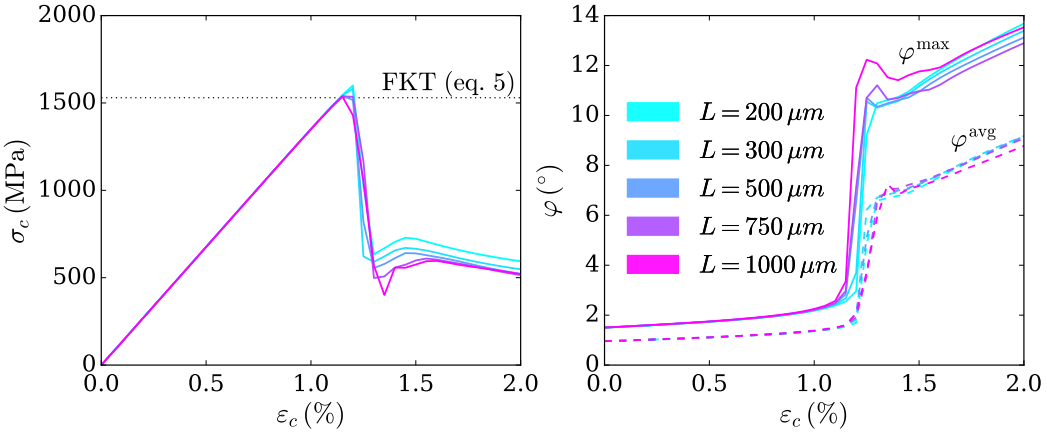

(a) Stress vs. strain curves

(b) Kink band rotation ($\varphi^{\max}$, φ^{avg})

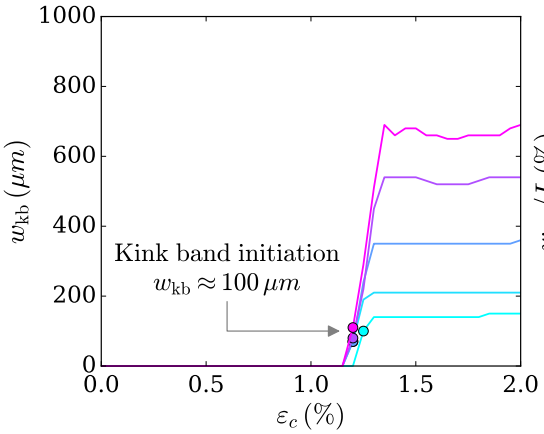

(c) Kink band width (w_{kb})

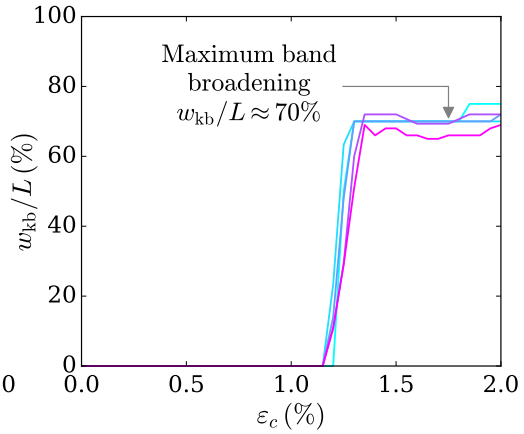

(d) Relative kink band size (w_{kb}/L)

Figure 18. Analysis of the single-fiber 3-D model length, L, for $\varphi_0 = 1.5°$ with $L = 200, 300, 500, 750$ and 1000 µm.

kink band kinematics. This version of the CMM model is used as the nominal configuration throughout the remainder of this report.

3.5.2 Sequence of events in the kinking process

The sequence of events observed in the CMM model is illustrated in Fig. 19. Critical points in the process are indicated by the points labeled i through iv on the predicted stress vs. strain response provided in Fig. 19a. As the compressive stress, σ_c, increases the shear stress along the matrix grows due to the fiber initial misalignment, eq. (A1). At point *i*, the matrix starts yielding along a narrow band at the center of the imperfection, as shown in Fig. 19b. The yielded region continues spreading in the longitudinal direction until the yield band is wide enough to promote local rotation of the fiber (point *ii*), leading to the formation of a kink band (point *iii*), as shown in Fig. 19b and c. The same sequence of events prior to fiber kinking was observed by Davidson and Waas [110]. Fiber rotation results in a sudden drop in load carrying capacity and produces the kink band, which corresponds to the region where the matrix has deformed plastically bounded by the fiber sections with the highest bending stresses, see Fig. 19d. The fiber/matrix interface also participates in triggering fiber kinking. When the interface is damaged (Fig. 19c), the fiber cannot transfer part of the shear load to the matrix, resulting in premature kinking failure.

Due to the single-fiber model design and the periodic boundary conditions, once the kink band appears, it is assumed that it has already propagated simultaneously through the whole composite, so transverse propagation cannot be observed with this model. Instead, as compressive strain increases, ε_c, the kink band keeps growing along the fiber direction. This phenomenon is known as band broadening, and can be observed experimentally once the kink band has fully propagated across the specimen (in the direction transverse to the loading) [25]. Band broadening is accompanied by progressive fiber rotation, while compressive stress decreases gradually (Fig. 19d). This sequence of events was also observed in the literature in periodic models including several fibers [63].

Neither the tensile strength nor the compressive strength of the fibers are reached for the model parameters considered here. Small values of initial misalignment do result in fiber damage, as discussed in Section 4.2. For small values of initial misalignment, $\varphi_0 < 1^\circ$, the fibers fail under pure compression yielding a constant compressive strength value, X_c, regardless of φ_0 [57]. However, fiber breakage was not observed in the models with initial misalignment higher than 1°, neither at fiber kinking initiation, nor during kink band broadening. Such predictions seem unrealistic since nearly all experimental observations of kink bands show broken fibers. More realistic failure models for the fibers are required to address this deficiency.

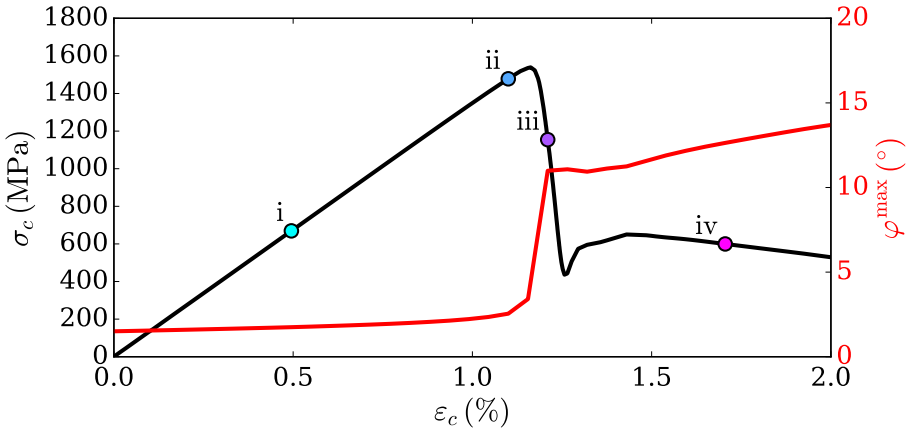

(a) Stress vs. strain curve including maximum fiber rotation ($\varphi^{\max}$)

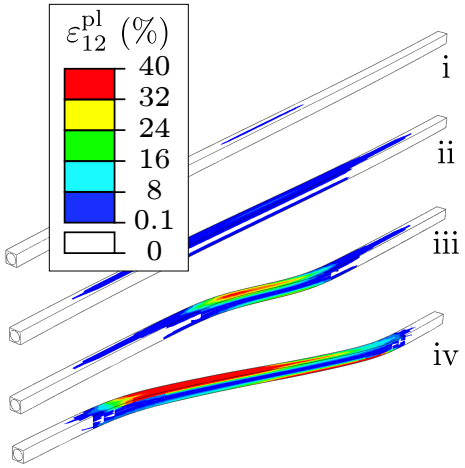

(b) Plastic shear strain of the matrix

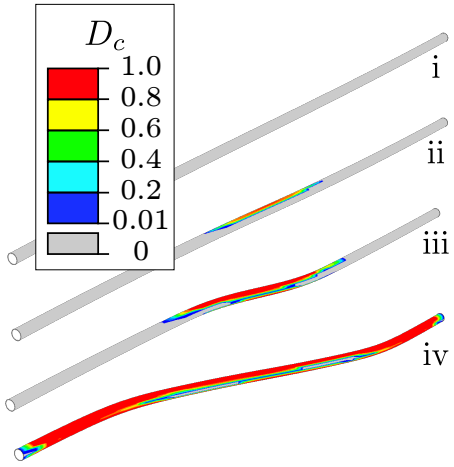

(c) Fiber/matrix interface damage evolution

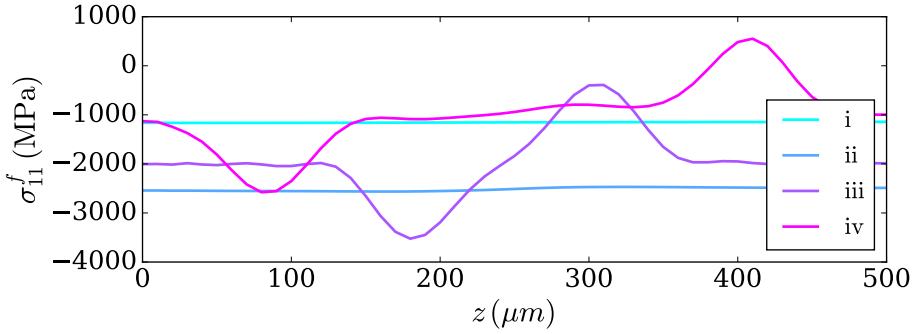

(d) Longitudinal stress along the upper section of the fiber

Figure 19. Summary of the sequence of events prior to and after fiber kinking for AS4/8552 with $\varphi_0 = 1.5°$.

3.5.3 Kink band angle

The use of periodic boundary conditions in the CMM single-fiber model forces the kink angle, β, to be zero [57]. Since the model predicts the residual stress, σ_r, the kink band angle can be estimated from by rearranging eq. (12) as

$$\beta = \frac{1}{2} \arcsin\left(\frac{2\tau_L}{\sigma_r}\right) \tag{53}$$

Using eq. (53) with the residual stress values from the CMM model ranging between 600 and 500 MPa from fiber kinking initiation up to 2% strain (as shown in Fig. 18a) and assuming a shear yield stress $\tau_L = 95$ MPa (at 5% strain in Fig. 15b), the resulting effective kink angle is found to be between 9° and 12°. This range for β agrees well with values reported in an experimental study carried out in parallel through X-Ray computed tomography observation of fiber kinks in IM7/8552 [71].

For the sake of completeness, the 3-D multiple fiber model was used to obtain the kink band angle, β. The model was similar to the 3-D multiple-fiber model described in Section 3.5.1, but included an inhomogeneous initial misalignment to trigger fiber kinking from one of the edges following the approach of Vogler et al. [54]. To improve the stability of the problem, loading is applied in two steps [54]. First, a constant compressive stress, σ_c, in the fiber direction is applied up to a subcritical level. Then, an in-plane shear load, τ_{12}, is increased until fiber kinking takes place. The kink band initiates on the free edge where the larger initial misalignment is located and propagates across the model with a β angle of 12° and a constant band width, $w_{\text{kb}} = 100$ µm, as shown in Fig. 20. The values for β and w_{kb} are in good agreement with the values obtained from the single-fiber models and with values reported in the literature. Some kink band angle values reported in the literature for carbon reinforced composites are shown in Table 10. Although a variety of experimental techniques were employed to promote the fiber kinking failure mechanism, it is observed that typical values of β are found between 10° to 20° in most cases.

From the shear stress-strain curve, Moran's energy-based analytical model [25] is able to predict σ_r and β for fiber kinking assuming there is no change of volume in the material, thus $\varphi = 2\beta$. The values obtained from Moran's model using the Ramberg-Osgood shear stress-strain curve (substituting eq. (4) in eq. (13) and minimizing with respect to β) are similar for both AS4/8552 and IM7/8552, due to the similar shear curves. The σ_r predicted is around 300 MPa with $\beta = 40°$. Although the estimation for σ_r is reasonable compared to the results of the models presented in this work, the kink band angle is not in good agreement with the CMM model. The mismatch in β is likely a result of the fact that the CMM model includes compressibility of the matrix and is therefore not restricted to Moran's assumption of $\varphi = 2\beta$. Vogler et al. [54] showed that β is a function of pressure sensitivity and dilatancy of the matrix, which may explain the difference between the present model and Moran's model. It also should be noted that using the residual stress from the CMM model predictions $\sigma_r = 400$ MPa in Moran's model results in $\beta \approx 18°$, which is in much better agreement.

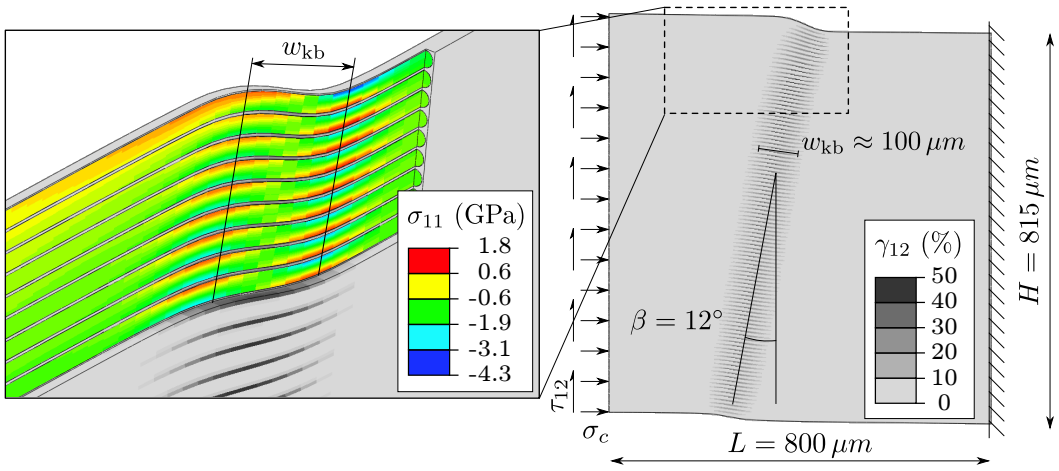

(a) Stress field along the kink band (b) Plastic deformation of the matrix

Figure 20. Multiple-fiber 3-D model based on [54] to obtain the kink angle, β, of AS4/8552. Kink band width, w_{kb}, is highlighted.

Table 10: Kink band angle values reported in the literature from experiments and numerical models.

Material system	β [°]	Method	Reference
IM7/8552	5–30	Experimental	Lee and Soutis [111]
IM7/8552	15–25	Experimental	Bergan and Garcea [71]
IM7/8551-7	17	Numerical	Bishara et al. [62]
AS4/8551-7	15	Numerical	Bishara et al. [62]
AS4/PEEK	16	Experimental	Jelf and Fleck [24]
AS4/PEEK	20–30	Experimental	Couque et al. [112]
AS4/PEEK	12–16	Experimental	Kyriakides et al. [5]
AS4/PEEK	12–15	Experimental	Vogler et al. [55]
AS4/PEEK	5–17	Numerical	Vogler et al. [54]
T300/913	22–28	Experimental	Pinho at al. [75]
T800/924C	10–15	Experimental	Fleck et al. [23]
T800/924	8–10	Numerical	Pimenta et al. [7]
APC-2/PEEK	12–22	Experimental	Moran et al. [25]

4 Comparison of the mesoscale and micromechanical models

The predictions from the micromechanical model were compared with the predictions from the mesoscale model to understand the role of the simplifying assumptions in the mesoscale model. In both analyses, an end shortening displacement in the longitudinal direction was prescribed. In this section, the micromechanical model

assumes the fiber behaves as a nonlinear elastic solid ($c^f \neq 0$) and considers tensile and compressive failure, except where noted. The mesoscale finite element model is composed of one cubic C3D8R element with an edge length $l_1 = 0.15$ mm as described in Section 2.7.1. The material properties used in the mesoscale analysis are provided in Table 4.

Additionally, analytical models from the literature, including Argon's model, Pimenta's model, and Budiansky's FKT are compared with the CMM and CDM model results where applicable. The assumptions followed to characterize the shear response of the material are fundamental to the prediction of fiber kinking for all of the analytical models considered. The characteristic shear curves for the different models are shown in Fig. 21. Argon's expression, eq. (2), considers the matrix as a rigid perfectly-plastic solid [13]. A value of 80 MPa was assumed as the yield limit of the matrix under shear. On the other hand, Pimenta's model [29] assumes an elastic-perfectly plastic (EPP) matrix shear response and is based upon micromechanical features such as fibers packing and cross section. The shear modulus is defined as $G^m_{2\mathrm{D}} = G^m/(1 - V^f_{2\mathrm{D}}) = 10.06$ GPa, and the shear yield limit is set to $\tau_Y = 80$ MPa. Budiansky's FKT does not require a simplified shear response, and so a more representative constitutive nonlinear response can be used. For comparison

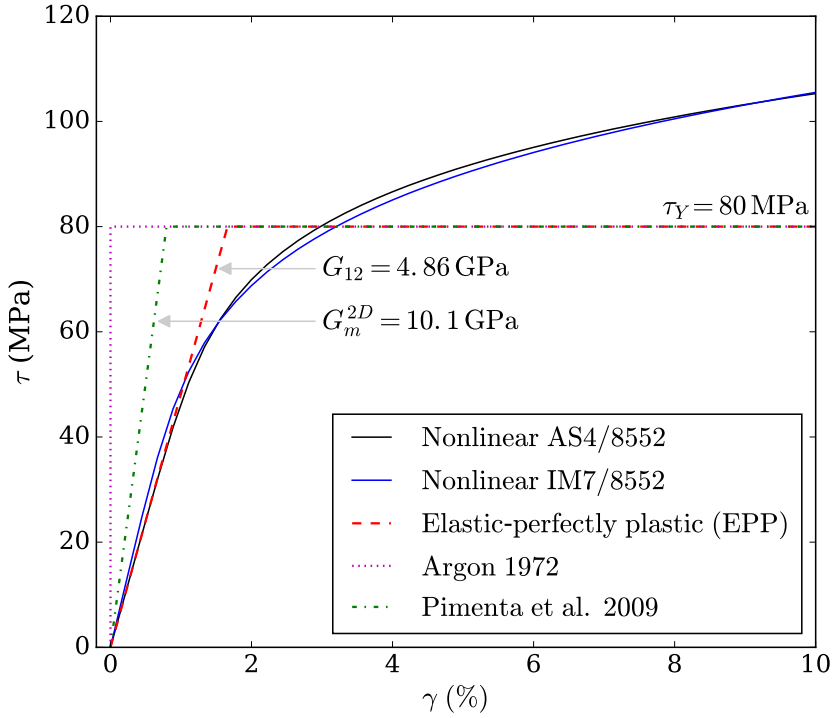

Figure 21. Experimental nonlinear shear curves for AS4/8552 and IM7/8552 and simplified curves of other models: perfectly-plastic of Argon's model [13], elastic perfectly plastic (EPP) and Pimenta's model with a modified shear modulus, $G^m_{2\mathrm{D}}$ [29].

with the other models, both the Ramberg-Osgood and EPP shear responses are used with the FKT approach.

4.1 Stress vs. strain response

The predicted stress-strain curves indicate excellent agreement between the two models (CDM and CMM) for a variety of initial fiber misalignments, φ_0 of 1.5, 2, 2.5, 3, and 4°, as shown in Fig. 22a for AS4/8552. The compressive stress, σ_c, is the nominal stress calculated as the reaction force divided by the original area, and the compressive strain, ε_c, is the end shortening divided by the original length. Both models predict the initial elastic response, strength, subsequent collapse, and finally a non-zero residual stress. Since the energy released during instability is large for small values of φ_0, some vibrations are predicted by both models immediately after the instability. The transition from a strong instability (snap-back) to a smooth response is predicted by both models to occur between $\varphi_0 = 2.5°$ and 3°. The value of φ_0 at which the transition to snapback occurs can be estimated from FKT as the smallest value of φ_0 for which there exists a local maximum of eq. (7). The results in Fig. 22a illustrate that both models predict a dependence of the peak load on φ_0 whereas the predicted residual stress, σ_r, is independent of φ_0, which is consistent with fiber kinking theory. Moran et al. [25] and others proposed the residual stress to be a material property. A range of values of σ_r, calculated using eq. (12), is superimposed on Fig. 22 showing very good agreement with the model predictions. The range of σ_r was calculated using the shear strength at 5% strain $\tau_L = 95$ MPa and β was varied from 12° to 16°, as reported from an experimental investigation on IM7/8552 [71], in eq. (12). The residual stress is expected to follow an asymptotic trend at large compressive strain ($\varepsilon_c > 20\%$) as shown in the material model developed by Gutkin et al. [51], which yields an asymptotic value around 230 MPa for another carbon fiber reinforced epoxy resin (HTS45/LY556). The excellent agreement between the two models for strength, subsequent instability, and residual stress suggests that the most significant features of the kinking process are captured by the relatively simple mesoscale model. Further, the agreement between the two models demonstrates that ignoring fiber bending appears to be a reasonable assumption for relatively small carbon fibers with large wavelength misalignments. Similar results were obtained from both the CDM and CMM models for the IM7/8552 material system.

Of the analytical models, only Hsu's augmentation of FKT, eqs. (6) and (7), and Pimenta's, eq. (14), provide a complete stress vs. strain response. The results obtained from these two models are plotted next to the CMM and CDM curves in Fig. 22b for $\varphi_0 = 2.0°$. The stiffness predicted by Pimenta's model is constant up to the peak-load because it does not include the fiber nonlinear elastic behavior. The strength predicted by this model is different from the other models in the figure in that it considers a linear elastic perfectly plastic response of the composite lamina under shear, instead of the more realistic strain-hardening shear response employed by the CMM and CDM models. During fiber kinking, the snap-back phenomenon is captured by Pimenta's model because the model is not displacement-controlled. A lower σ_r is predicted by Pimenta's model compared to the other models. The main

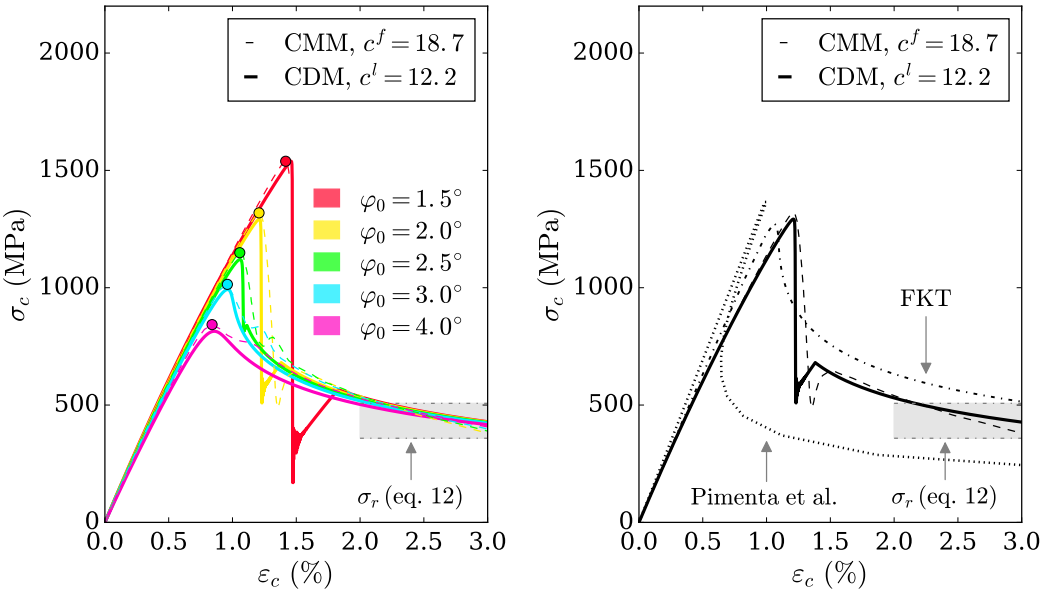

(a) Different initial fiber misalignments (b) Comparison with analytical models

Figure 22. Stress vs. strain curves for the CMM and CDM models of AS4/8552 including nonlinear response of the fibers ($c^f,\ c^l \neq 0$). Comparison with analytical models of the literature (FKT [18] and Pimenta et al. [29]). Residual stress, σ_r, is estimated from eq. (12).

feature responsible for the difference in σ_r is the shear curve shape. The absence of strain hardening in Pimenta's model results in the lower prediction for residual stress level. The effect of not considering strain hardening in the shear response is also noticed in the predictions for fiber rotation, as discussed in Section 4.3. On the other hand, FKT predicts the same compressive strength as the CMM and CDM models, since it is based on the same nonlinear shear curve. However, the stiffness of the composite up to collapse is slightly higher in the FKT result since the fiber modulus is assumed to be constant. The residual stress predicted agrees very well with the CDM and CMM models.

4.2 Strength sensitivity curves

The compressive strength, X_c, for AS4/8552 and IM7/8552 predicted by FKT, eq. (5), and by the CMM single-fiber model are shown in Fig. 23a as a function of φ_0 . Very good agreement is observed between the two models for $\varphi_0 \geq 1°$, which is attributed to the similarity of the nonlinear shear response in the two models (Fig. 15). Though not shown, the predictions by the mesoscale model are identical to the FKT results, as is expected since the mesoscale model is based on FKT. The strength sensitivity curve provides a one to one relation between X_c and φ_0, such that, for the typical compressive strengths of the materials addressed in this work

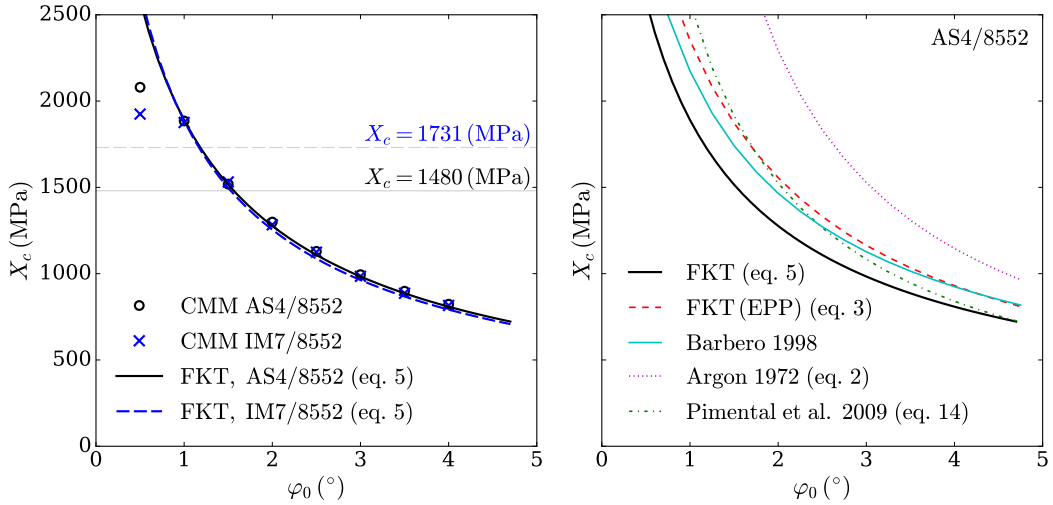

(a) Comparison of the CMM results and FKT predictions

(b) Comparison of the strength predicted by various analytical models [3, 13, 19, 29] and FKT [18]

Figure 23. Compressive strength sensitivity curves.

(horizontal lines in Fig. 23a), a representative value of φ_0 is obtained: 1.2° and 1.6° for IM7/8552 and AS4/8552, respectively.

For very small values of initial misalignment, $\varphi_0 < 1°$, the CMM model predicts fiber failure due to pure longitudinal compression, instead of fiber kinking. A cut-off strength point is found at $X_c = V^f \cdot X_c^f$, yielding 2100 and 1920 MPa for AS4/8552 and IM7/8552 respectively.

The strength sensitivity curves predicted by other analytical models are shown in Fig. 23b. All the models predict a critical effect of the initial misalignment, φ_0, on the compressive strength, X_c, of the unidirectional fiber-reinforced composite. The effect of the misalignment, $\partial X_c/\partial\varphi_0$, is more pronounced for low initial misalignment angles. Argon's model predicts the highest strength for the misalignment range considered, going to infinity for the limit $\varphi_0 = 0°$. The two FKT predictions show the effect of the Ramberg-Osgood shear curve as compared with the EPP shear curve: the EPP shear curve produces higher strengths for the same misalignment angle. In both cases, FKT has an upper limit $X_c(\varphi_0 = 0) = G_{12}$. Pimenta's model predictions are very close to the FKT results obtained using the same EPP shear curve. The assumptions and strategy followed by Pimenta could be extended for different nonlinear shear curves as proposed by the author [29]. Finally, Barbero's analytical model predicts a similar strength-misalignment trend [19]. For the results presented, a half-normal statistical distribution of the fiber misalignment was assumed with zero mean and standard deviation of φ_0.

4.3 Fiber rotation

The fiber rotation angle, φ, as a function of the longitudinal strain for AS4/8552 is shown in Fig. 24a for φ_0 ranging from 1.5° to 4°. Since $\varphi = \varphi(z)$ in the CMM model, two definitions for φ are plotted for comparison with the fiber rotation, φ_{CDM}, predicted by the CDM model in eq. (38). The maximum fiber rotation in the CMM model takes place at $z = L/2$ and is denoted as $\varphi^{\text{max}}_{\text{CMM}}$. The average rotation of the kinked fiber is calculated from the transverse deflection at the end of the fiber, u_y, and the kink band width, w_{kb}, as $\varphi^{\text{avg}}_{\text{CMM}} = \tan^{-1}(u_y/w_{\text{kb}})$. In all cases, the fiber misalignment shows slight rotation ($\varphi \approx \varphi_0$) prior to the strain at which the peak load is attained. When the critical strain corresponding to the peak load is reached, the fiber rotates rapidly into the kinked configuration, which is seen as the abrupt change in φ in Fig. 24a at $\varepsilon_c \approx 1\%$. The rotation is much more rapid for small initial fiber misalignments than for large initial fiber misalignments. Under yet higher strains (in the strain regime that corresponds with the residual stress, $\varepsilon_c \geq 1.5\%$) the fibers continue to rotate at a constant rate with increasing ε_c. The fiber rotation predicted by the CDM is bounded by the average and maximum φ from the CMM model. It could be argued that φ_{CDM} should match $\varphi^{\text{max}}_{\text{CMM}}$ since both represent the critical or maximum fiber misalignment. The difference between φ_{CDM} and $\varphi^{\text{max}}_{\text{CMM}}$ is most likely due to considerations of fiber bending and periodic

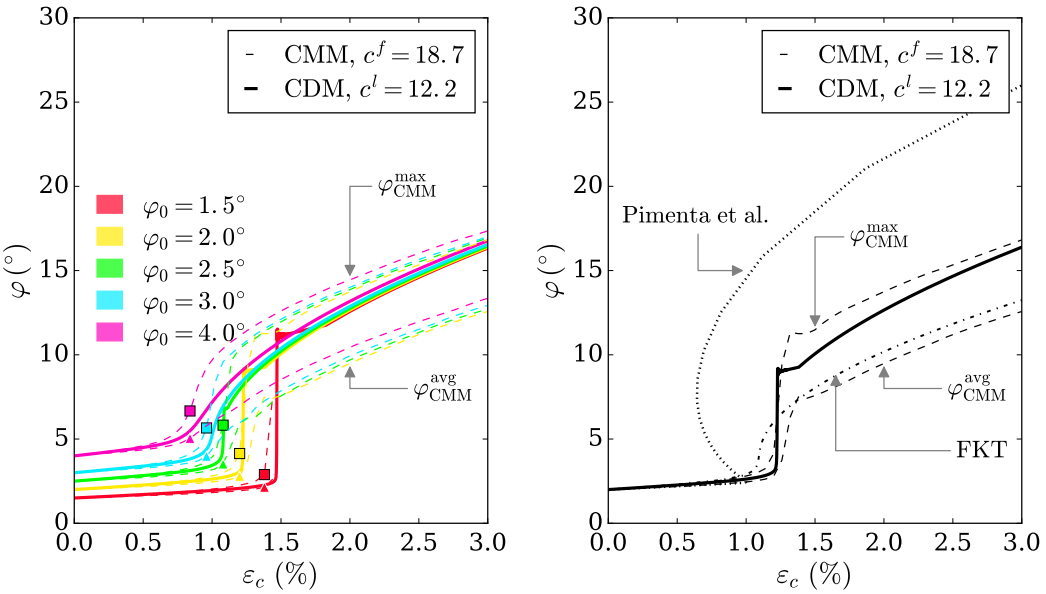

(a) Different initial fiber misalignments

(b) Comparison with analytical models for $\varphi_0 = 2°$

Figure 24. Fiber rotation curves for AS4/8552 obtained from the CMM and CDM models, and compared with analytical models from the literature (FKT [18] and Pimenta et al. [29]).

boundary conditions in the CMM model, both of which affect the fiber rotation and are not included in the CDM. It should be noted that different material systems may be more sensitive to fiber bending, in which the agreement between the two models would be limited. Nonetheless, the agreement between the two models is quite good and thus highlights further efficacy of the relatively low-fidelity mesoscale model at representing the large rotations associated with the fiber kinking process as predicted by the high-fidelity micromechanical model.

Results from the model proposed by Pimenta et al. [29] are included in Fig. 24b displaying the maximum rotation of the fiber during kinking. In qualitative terms, the same features are represented: fiber rotation is negligible up to the point when the fiber kinking mechanism is triggered. Then, sudden rotation of the fibers happens during snap-back. Finally, under large compressive strains, the fibers continue to rotate gradually. However, quantitatively, the predictions for φ rise beyond 20° at $\varepsilon = 2\%$, which is noticeably higher than $\varphi \approx 14^\circ$ predicted by the mesoscale and micromechanical models for the same strain level. By ignoring strain-hardening, the model underestimates the shear stiffness at large strain and therefore over predicts φ. Nevertheless, Hsu's [18] analytical estimate, based upon FKT theory, of the fiber rotation is equivalent to the average fiber rotation obtained from the micromechanical model, $\varphi^{\text{avg}}_{\text{CMM}}$, see Fig. 24b. It is important to notice that this analytical model employs the characteristic Ramberg-Osgood nonlinear shear curve which is introduced in the CDM model, see Fig. 15c.

4.4 Fiber nonlinearity

The effect of fiber nonlinearity on the mechanical response of the CMM and CDM models is illustrated in Fig. 25. Both models account for fiber nonlinearity and therefore show a pre-peak reduction in stiffness. The resulting compressive strength, X_c, is not affected. However, fiber nonlinearity increases the strain to failure from 1% to 1.2% for AS4/8552 with $\varphi_0 = 2^\circ$ in both models. Kink band rotation is not affected once the fiber kinking phenomenon is triggered, following the same rotation rate ($\partial\varphi/\partial\varepsilon_c$).

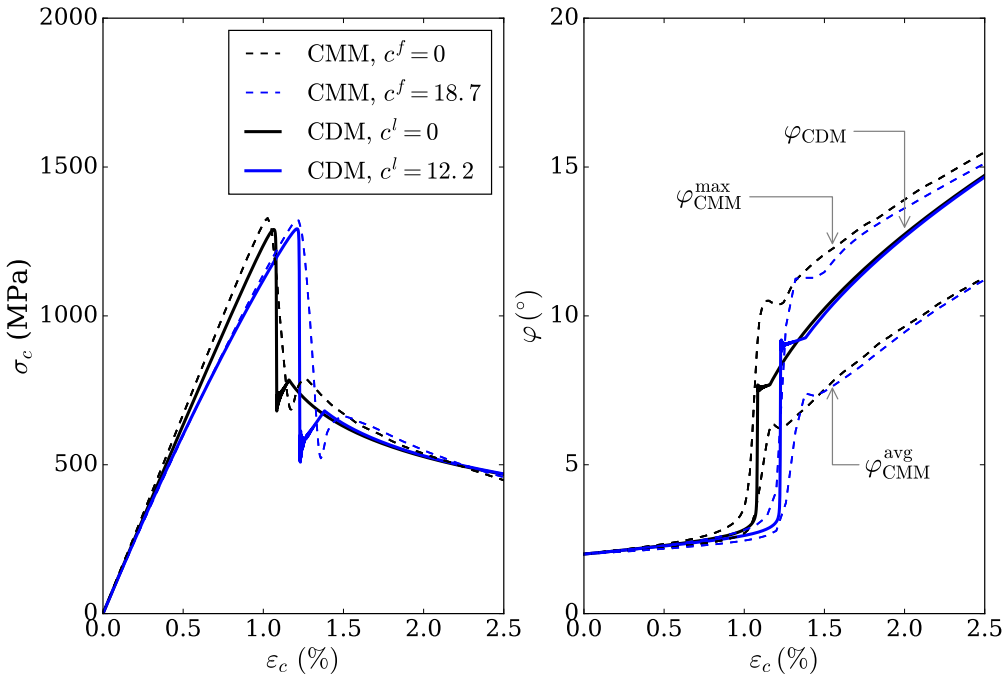

(a) Stress vs. strain curves

(b) Fiber rotation

Figure 25. Comparison of the CMM and CDM models for AS4/8552 with and without nonlinearity of the fibers.

4.5 Kink band width

The kink band width, w_{kb}, was computed in the micromechanical model as the distance between the points with the highest bending stress along the fiber occurring at the peak stress following [29]. The CMM model shows $w_{\text{kb}} \propto d$, as reported in the literature [3, 24]. The results for w_{kb} of the CMM model as well as other analytical models from the literature considering fiber bending [3, 23, 29] are presented in Table 11.

The CDM model does not consider fiber bending, as detailed in Section 2, so a kink band width value must be specified as input to the model. The values employed in the CDM model are reported in Table 11 and are based on the CMM results and analytical models from the literature [3, 23]. The selection of w_{kb} has an important effect on the post-peak response of the model as shown in Fig. 26. Wider kink bands arrest kink band rotation (see Fig. 26b and d), thus enhancing the residual stress sustained by the material during the softening regime for both material systems, as shown in see Fig. 26a and c. Most of the kink band rotation occurs abruptly during the load drop right after the peak stress is reached. The sensitivity of the residual stress to the kink band width is an important consideration for application of the CDM. In the event that experimental evidence of the kink band width is not available, the CMM provides an important utility for use of the CDM in that the

kink band width input parameter for the CDM can be determined from the CMM.

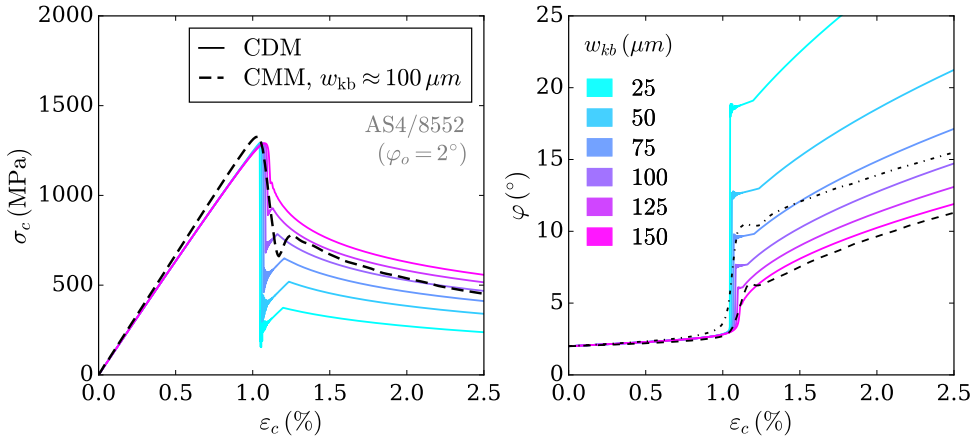

(a) Stress vs. strain curves (AS4/8552)

(b) Fiber rotation (AS4/8552)

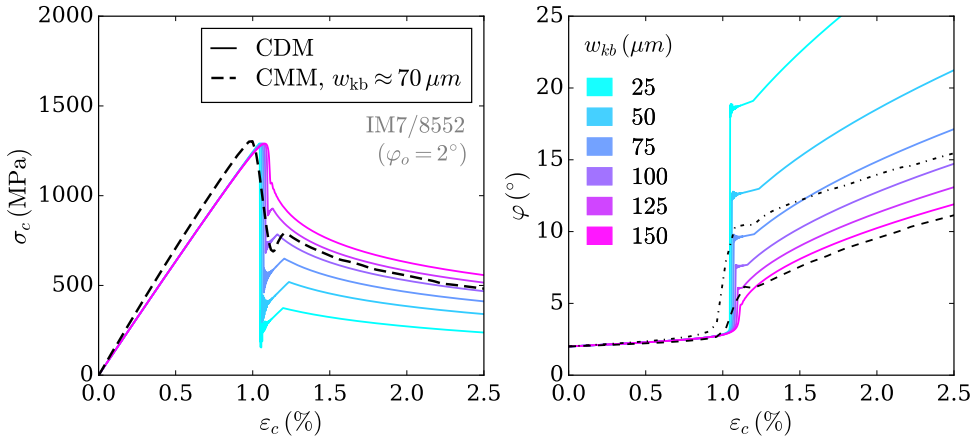

(c) Stress vs. strain curves (IM7/8552)

(d) Fiber rotation (IM7/8552)

Figure 26. Effect of the kink band width, w_{kb}, on the CDM constitutive model. Curves obtained for $\varphi_0 = 2°$ and $c^l = c^f = 0$.

Table 11: Values for w_{kb}.

Material	CDM [µm]	CMM [µm]	eq. (42) [µm]	Fleck et al. [23] [µm]	Pimenta et al. [29] [µm]
AS4/8552	100	90 – 120	50	85	62 – 118
IM7/8552	50	50 – 80	38	70	48 – 93

5 Parametric studies with the micromechanical model

Taking advantage of the CMM single-fiber model presented in Section 3, two parametric studies were carried out: the first one analyzes the effect of the fiber-matrix interface strength on the fiber kinking mechanism, and the second tests the potential of the fiber cross section to improve the mechanical performance of the composite material under longitudinal compressive loads. For simplicity, the results shown in this section do not include fiber nonlinearity (i.e. $c^f = 0$) or fiber failure.

5.1 Fiber-matrix cohesive interface analysis

A parametric study of the fiber-matrix cohesive interface strength was carried out to analyze its effect on the fiber kinking mechanism. To this end, the single-fiber CMM model with an initial misalignment of $\varphi_0 = 2^\circ$ was simulated for different interface shear strengths, $S^c = 21$, 63, 85 and 300 MPa. The baseline case with $S^c = S^c_0 = 85$ MPa corresponds to the results presented in Section 4 and the interface properties of Table 8. For the rest of the interface shear strength cases, the normal strength and fracture energies were scaled accordingly. The case where $S^c = 300$ MPa, represents a perfect interface model. The fiber-matrix friction coefficient was kept constant, $\xi^c = 0.4$, except where noted.

The results of this analysis are summarized in Fig. 27. A low interface strength triggers fiber kinking earlier, reducing the compressive strength as shown in Fig. 27a for the cases with $S^c = 21$ and 63 MPa. On the other hand, when the interface shear strength is higher than the shear yield limit of the matrix, $S^m = 80$ MPa, fiber kinking is activated by matrix shear instability regardless of the interface strength. For this reason, a perfect interface does not increase the compressive strength of the material.

The residual stress is not only dependent on the matrix yield limit in shear, S^m, but also on the ability of the interface to transfer load between the matrix and the fiber. A strong interface is able to sustain the shear loads on the interface and promotes the plastic shear deformation of the matrix as shown in Fig. 27c for the case with $S^c = 85$ MPa. On the other hand, if the interface is weak, it fails prematurely and the matrix slips along the fiber when the interface shear stress overcomes the interface shear strength, preventing plastic deformation of the matrix. In Fig. 27d, it is observed the interface longitudinal slippage, δ^c_z, is much higher for the weak interface case going up to 1.4 µm, compared to 0.5 µm over a larger fiber section. According to this hypothesis, the perfect interface case can be employed as an upper bound of σ_r as it further exploits the potential of the matrix to dissipate plastic energy through shear deformation.

The effect of a frictionless interface was observed after the load drop due to fiber kinking. Although, friction does not participate until the fiber-matrix interface is damaged, it plays a role arresting fiber rotation during the post peak regime. In absence of friction, fiber rotation can only be arrested by fiber bending and matrix hardening due to the hydrostatic pressure induced by φ, thus fiber rotation in the CMM model with $\xi^c = 0$ is higher as shown in Fig. 27b. The additional fiber rotation results in a reduction in σ_r by about 150 MPa.

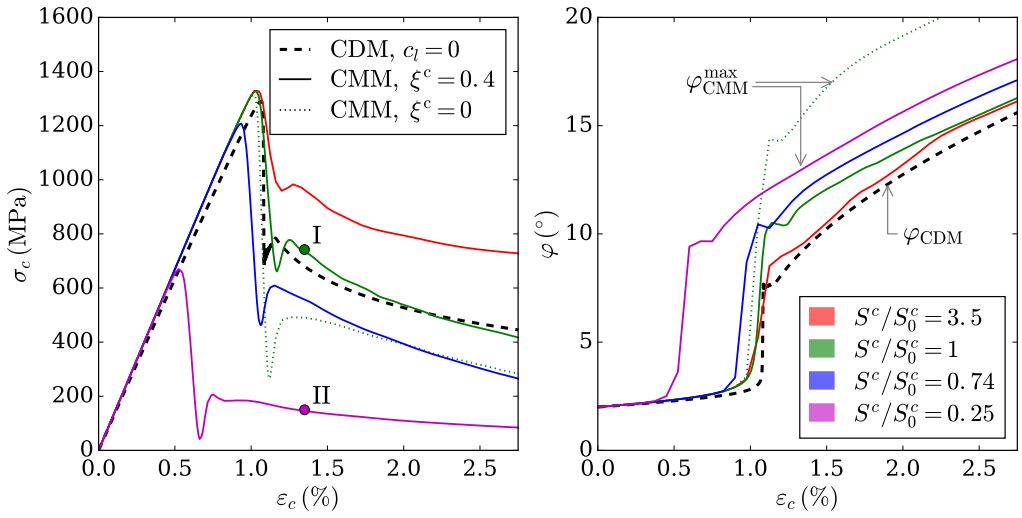

(a) Stress vs. strain curves

(b) Fiber rotation

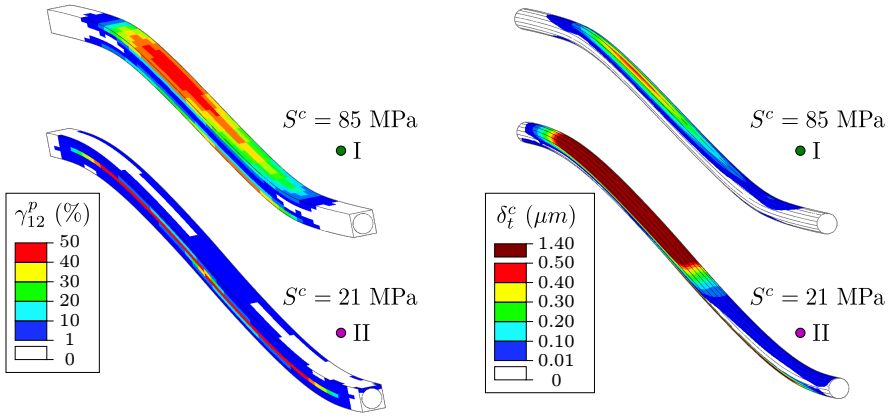

(c) Plastic shear strain (γ^p_{12}) at I and II

(d) Interface slippage (δ^c_t) at I and II

Figure 27. Effect of fiber-matrix interface shear strength of AS4/8552 with $\varphi_0 = 2°$.

5.2 Non-conventional fiber cross sections

While conventional carbon fibers are circular, some research groups have been able to produce non-conventional carbon fiber cross sections using different techniques [113]. A wide variety of carbon fiber sections produced at lab-scale can be found in the literature: lobular [114], ribbon-shaped [115], with complex patterns and hollow sections [116], to cite some of them. An especially attractive fiber pattern for the design and production of lightweight structures are hollow fibers. In this regard, the research work carried out by Kumar [117] on the manufacturing of hollow honey-comb carbon fibers should be highlighted. Using the cross section geometry developed by Kumar, a short study on the potential of hollow fibers to provide

higher specific strength to fiber kinking was performed. Two fiber cross sections were tested: a hollow tube-like fiber (HT), and a honeycomb hollow fiber (HC). AS4 carbon fiber properties were assumed, with a fiber diameter, d, see Table 6. For simplicity, the fiber is a linear elastic transversely isotropic solid without any failure criterion. The matrix volume fraction was kept constant to $V^m = 40\%$ while varying the void volume fraction, V^v, as reported in Fig. 28e. Hollowness is controlled by the diameter, d^v, of the channels or "islands", see Fig. 28c–d.

The results of the parametric study are summarized in Fig. 28. The loss in stiffness can be estimated from the rule of mixtures, nevertheless, as the hollowness fraction increases ($V^v \geq 24\%$), HC fibers stiffness is slightly higher compared to the HT fibers due to their higher bending stiffness as observed in Fig. 28a and in the last column of Fig. 28e where the relative second moment of area compared to the baseline cross section are shown, I_x^f / I_x^{f0}. The compressive strength, X_c, is not significantly affected by the reduction in the longitudinal stiffness from the fiber hollowness. The HT and HC designs preserve the fiber bending stiffness efficiently, providing an important increase of the specific compressive strength per unit mass compared to the solid baseline fiber as shown in Fig. 28b. The residual stress level remains unaffected by the fiber hollowness as it is mainly governed by the matrix shear yielding.

Some variables that were not considered are the fiber failure due to higher compressive stress levels that would promote premature collapse of the material, and the higher fiber waviness and defects which arise from the more complex fiber architecture and may degrade the strength of the composite material. Although this parametric study is missing important variables that will play a role on the final mechanical response of the virtual composite material, the preliminary results are promising in terms of lightweight structural designs in the near future. Potential applications are found in woven configurations, where fiber waviness is very high and the longitudinal stresses sustained by the fibers are not as high as in the unidirectional ply case.

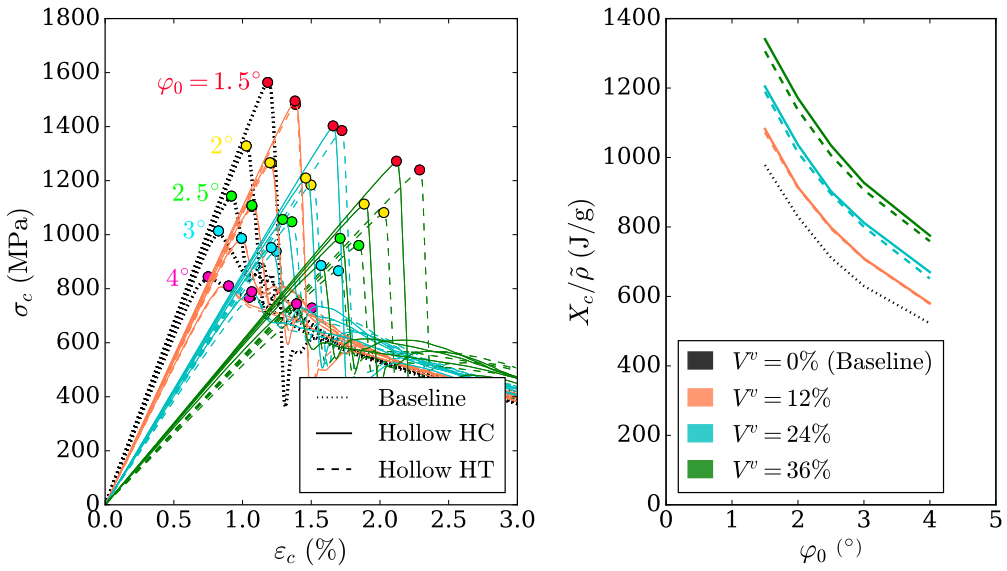

(a) Stress vs. strain curves

(b) Specific strength (X_c/ρ)

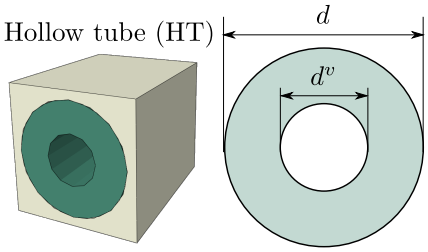

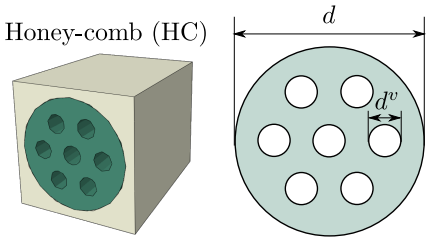

(c) Hollow-tube fiber design (HT)

(d) Honey-comb fiber design (HC)

Case	V^v [%]	V^f [%]	V^m [%]	$\tilde{\rho}$ [g/cm^3]	I_x^f/I_x^{f0} (HT − HC)
Baseline	0	60	40	1.58	1
Case 1	12	48	40	1.36	0.96 − 0.94
Case 2	24	36	40	1.15	0.84 − 0.85
Case 3	36	24	40	0.93	0.64 − 0.73

(e) Geometrical features of the hollow-fiber cross sections

Figure 28. Parametric study of the effect of hollow fibers cross section on the mechanical response under longitudinal compressive loading.

6 Concluding Remarks

A mesoscale continuum damage mechanics (CDM) model based on fiber kinking theory has been developed. This model has a stress-strain response that includes a sharp drop due to the onset of fiber kinking, followed by a nonzero residual stress. Furthermore, the mesoscale model tracks the fiber rotation through the kinking response such that longitudinal shortening deformation is coupled with shearing deformations. These characteristics arise from consideration of material nonlinearity in the shear stress-strain behavior and large fiber rotations. Thus, the constitutive response is not prescribed directly. Rather, it is a result of the fundamental material and geometric nonlinearities that contribute to the fiber kinking process. Verification studies demonstrated that the mesoscale model reproduces strength, fiber rotation, and residual stress in excellent agreement with fiber kinking theory.

The mesoscale model makes use of the deformation gradient decomposition (DGD) technique to enable mesh objectivity. Analyses of an unnotched compression configuration with three mesh sizes suggest that the model results are objective with respect to the mesh size. The initial fiber misalignment angle φ_0 provides a means of introducing stochastic variations into the model with a physical basis. Introducing spatial variation in φ_0 is necessary for accurate structural simulation so that the mean value φ_0 is near zero. Additionally, variation in φ_0 is useful to trigger localization of damage in structures with a uniform stress field.

A high-fidelity computational micromechanics (CMM) model was developed to further understanding of the fiber kinking mechanism and to assess the extent to which the mesoscale model captures the key features of fiber kinking. The CMM model was a 3-D single-fiber finite element model that considered nonlinearity in the fiber, matrix plasticity, and fiber/matrix interface debonding as well as geometric nonlinearity. The most significant difference between the CMM and CDM models as related to fiber kinking is that the CMM model includes fiber bending whereas the mesoscale model does not. The CMM model predicts that fiber kinking occurs with the following sequence of events: a) yielding in the matrix begins in a narrow band near the maximum misalignment well before peak load; b) then, under increasing load, yielding in the matrix spreads in the longitudinal direction until the yielded region is large enough to promote local rotation of the fiber; c) next, instability between fiber rotation and matrix yielding leads to the formation of the kink band; and d) finally, the rotation of the fibers is arrested once the angle becomes large. The kinking process predicted by the CMM model is in good agreement with other micromechanical models in the literature [110].

Comparisons between the mesoscale and microscale model serve as a basis for assessing how well the relatively coarse mesoscale model captures the key features of the fiber kinking process. To focus the comparisons on the characteristics of the two models instead of differences in input properties, the CMM model was calibrated with the same shear nonlinearity response used in the mesoscale model. The comparison between the mesoscale and microscale models was made through the analysis of the corresponding stress-strain curves (σ_c vs. ε_c) and the kinematics of fiber kinking (φ vs. ε_c). Analyses were also conducted to study the influence of the kink band width w_{kb} and the kink band angle β. The following conclusions are

drawn from the comparative study of the two models:

1. The stiffness of the microscale and mesoscale models showed very good agreement both with and without consideration for elastic nonlinearity in the fibers. It was noted that the coefficients of fiber nonlinearity for the microscale and mesoscale models are related by the rule of mixtures.

2. The strength predicted by the two models is a function of the initial misalignment angle and is nearly identical for $1^\circ < \varphi_0 < 4^\circ$. Small values of φ_0 lead to fiber compression failure, which is only accounted for in the CMM model.

3. Fiber kinking occurs as an instability due to interaction between fiber rotation and shear nonlinearity. The two models predict similar values of strain for the onset of the instability.

4. The residual stress σ_r predicted by the two models is in excellent agreement, with both models showing a slight decay under increasing compressive strain. The value of σ_r is a function of the width of the kink band and fiber rotation.

5. Despite the fact that mesoscale model does not include fiber bending, the results for fiber rotation (φ vs. ε_c) show excellent agreement throughout the kinking process. Both models show a jump in the fiber rotation at the onset of fiber kinking, followed by the progressive rotation of the fiber as the compressive strain increases.

6. The kink angle β is assumed to be zero in both models. While experimental measurements uniformly show nonzero values for β (Table 10), the two models are nonetheless able to capture the residual stress level in good agreement with models in the literature that account for $\beta \neq 0$. An effective $\tilde{\beta}$ angle can be estimated through eq. (12) yielding 10 to 15°, which is in agreement with an experimental study carried out through X-ray CT in IM7/8552 [71]. A multi-fiber micromechanical 3-D model based on [54] was employed to verify the β angle estimation. The multi-fiber model yielded $\beta = 12^\circ$ supporting the estimation using eq. (12) and in good agreement with the experimental measurements.

7. The mesoscale CDM model requires the kink band width w_{kb} as an input parameter. This value may be estimated from analytical models that consider fiber bending like [3, 23], measured experimentally [71] or computed numerically using micromechanical models like the CMM model presented.

The comparison between the results of the mesoscale and micromechanical models show a remarkable correlation in strength, post-peak residual stress, and fiber rotation. The quality of the correlation indicates that the significant features of the kinking process are included in the relatively simple mesoscale model.

Parametric analyses were conducted using the CMM model to explore opportunities to improve longitudinal compression strength. It was shown that the fiber-matrix interface properties (stress transfer between the fibers and the matrix) not

only controls the compressive strength, X_c, but also plays a major role on the residual stress, σ_r. If the interface is very weak, the fiber slides during kinking and the matrix is not deformed plastically. Fiber-matrix friction only has a positive effect on σ_r, reducing fiber rotation through the additional interface shear stress introduced by the friction coefficient. Additionally, it was shown that nonconventional hollow and honeycomb fibers provide improvements in specific strength if fiber breakage can be avoided.

While many developments in modeling fiber kinking at the micro and mesoscale have been described in this report, many questions remain unanswered. Further development at both scales in conjunction with detailed experimental investigations are needed to achieve predictive capability for failure by fiber kinking.

References

1. Schultheisz, C. R. and Waas, A. M., "Compressive failure of composites, Part I: Testing and micromechanical theories," *Progress in Aerospace Sciences*, Vol. 32, No. 1, Jan. 1996, pp. 1–42.

2. Piggott, M. R. and Harris, B., "Factors Affecting the Compression Strength of Aligned Fibre Composites," *Advances in Composite Materials*, 1980, pp. 305–312.

3. Budiansky, B., "Micromechanics," *Computers & Structures*, Vol. 16, No. 1-4, 1983, pp. 3–12.

4. Budiansky, B. and Fleck, N. A., "Compressive failure of fibre composites," *Journal of the Mechanics and Physics of Solids*, Vol. 41, No. 1, Jan. 1993, pp. 183–211.

5. Kyriakides, S., Arseculeratne, R., Perry, E. J., and Liechti, K. M., "On the compressive failure of fiber reinforced composites," *International Journal of Solids and Structures*, Vol. 32, No. 6-7, 1995, pp. 689–738.

6. Waas, A. M. and Schultheisz, C. R., "Compressive failure of composites, Part II: Experimental studies," *Progress in Aerospace Sciences*, Vol. 32, No. 1, 1996, pp. 43–78.

7. Pimenta, S., Gutkin, R., Pinho, S. T., and Robinson, P., "A micromechanical model for kink-band formation: Part I – Experimental study and numerical modelling," *Composites Science and Technology*, Vol. 69, No. 7-8, June 2009, pp. 948–955.

8. Budiansky, B., Fleck, N. A., and Amazigo, J. C., "On kink-band propagation in fiber composites," *Journal of the Mechanics and Physics of Solids*, Vol. 46, 1998, pp. 1637–1653.

9. Vogler, T. J. and Kyriakides, S., "On the axial propagation of kink bands in fiber composites : Part I experiments," *International Journal of Solids and Structures*, Vol. 36, No. 4, Feb. 1999, pp. 557–574.

10. Camponeschi, E. T., "Compression of composite materials: A review." Tech. rep., US Navy AD-A189 272, David Taylor Research Center, Bethesda, MD, 1987.

11. Naik, N. K. and Kumar, R. S., "Compressive strength of unidirectional composites: evaluation and comparison of prediction models," *Composite Structures*, Vol. 46, No. 3, Nov. 1999, pp. 299–308.

12. Rosen, B. W., "Mechanics of composite strengthening," *Fibre Composite Materials*, edited by Am. Soc. Metals Seminar, chap. 3, 1965.

13. Argon, A. S., "Fracture of composites," *Treatise on Materials Science & Technology*, Vol. 1, 1972, pp. 79–114.

14. Chaplin, C. R., "Compressive fracture in undirectional glass-reinforced plastics," *Journal of Materials Science*, Vol. 12, No. 2, 1977, pp. 347–352.

15. Wisnom, M. R., "The effect of fibre misalignment on the compressive strength of unidirectional carbon fibre/epoxy," *Composites*, Vol. 21, No. 5, 1990, pp. 403–407.

16. Ramberg, W. and Osgood, W. R., "Description of stress-strain curves by three parameters," Tech. rep., NACA Technical Note 902, National Advisory Committee for Aeronautics, Washington, DC, 1943.

17. Pinho, S. T., Dávila, C. G., Camanho, P. P., Iannucci, L., and Robinson, P., "Failure models and criteria for FRP under in-plane or three-dimensional stress states including shear non-linearity," Tech. Rep. February, NASA/TM-2005-213530, NASA Langley Research Center, 2005.

18. Hsu, S. Y., Vogler, T. J., and Kyriakides, S., "Compressive strength predictions for fiber composites," *Journal of Applied Mechanics*, Vol. 65, No. 1, 1998, pp. 7.

19. Barbero, E. J., "Prediction of compression strength of unidirectional polymer matrix composites," *Journal of Composite Materials*, Vol. 32, No. 5, 1998, pp. 483–502.

20. Smoot, M. A., "Compressive response of Hercules AS1 3501-6 graphite epoxy composites," Tech. rep., Center for Composite Materials, University of Delaware, Newark, DE, 1982.

21. Lagoudas, D. C. and Saleh, A. M., "Compressive failure due to kinking of fibrous composites," *Journal of Composite Materials*, Vol. 27, No. 1, 1993, pp. 83–106.

22. Wisnom, M. R. and Atkinson, J. W., "Constrained buckling tests show increasing compressive strain to failure with increasing strain gradient," *Composites Part A: Applied Science and Manufacturing*, Vol. 28, No. 11, Jan. 1997, pp. 959–964.

23. Fleck, N. A. and Jelf, P. M., "Deformation and failure of a carbon fibre composite under combined shear and transverse loading," *Acta Metallurgica Et Materialia*, Vol. 43, No. 8, 1995, pp. 3001–3007.

24. Jelf, P. M. and Fleck, N. A., "Compression failure mechanisms in unidirectional composites," *Journal of Composite Materials*, Vol. 26, No. 18, 1992, pp. 2706–2726.

25. Moran, P. M., Liu, X. H., and Shih, C. F., "Kink band formation and band broadening in fiber composites under compressive loading," *Acta Metallurgica Et Materialia*, Vol. 43, No. 8, 1995, pp. 2943–2958.

26. Schapery, R. A., "Prediction of compressive strength and kink bands in composites using a work potential," *International Journal of Solids and Structures*, Vol. 32, No. 6-7, March 1995, pp. 739–765.

27. Hahn, H. T. and Williams, J. G., "Compression failure mechanisms in unidirectional composites," Tech. rep., NASA TM-85834, NASA Langley Research Center, Hampton, VA, 1984.

28. Effendi, R. R., Barrau, J. J., and Guedra-Degeorges, D., "Failure mechanism analysis under compression loading of unidirectional carbon/epoxy composites using micromechanical modelling," *Composite Structures*, Vol. 31, No. 2, 1995, pp. 87–98.

29. Pimenta, S., Gutkin, R., Pinho, S. T., and Robinson, P., "A micromechanical model for kink-band formation: Part II – Analytical modelling," *Composites Science and Technology*, Vol. 69, No. 7-8, June 2009, pp. 956–964.

30. Wisnom, M. R., "Analysis of shear instability in compression due to fibre waviness," *Journal of Reinforced Plastics and Composites*, Vol. 12, No. 11, Nov. 1993, pp. 1171–1189.

31. Lemanski, S. L. and Sutcliffe, M. P. F., "Compressive failure of finite size unidirectional composite laminates with a region of fibre waviness," *Composites Part A: Applied Science and Manufacturing*, Vol. 43, No. 3, March 2012, pp. 435–444.

32. Sutcliffe, M. P. F., "Modelling the effect of size on compressive strength of fibre composites with random waviness," *Composites Science and Technology*, Vol. 88, Nov. 2013, pp. 142–150.

33. Zhang, L., Zhang, S., Jiang, Y., Tao, J., and Chen, X., "Compressive behaviour of fibre reinforced plastic with random fibre packing and a region of fibre waviness," *Journal of Reinforced Plastics and Composites*, 2016.

34. Fleck, N. A. and Shu, J. Y., "Microbuckle initiation in fibre composites : A finite element study," *Journal of the Mechanics and Physics of Solids*, Vol. 43, No. 12, Dec. 1995, pp. 1887–1918.

35. Shu, J. Y. and Fleck, N. A., "Microbuckle initiation in fibre composites under multiaxial loading," *Proceedings of the Royal Society A: Mathematical, Physical and Engineering Sciences*, Vol. 453, No. 1965, Oct. 1997, pp. 2063–2083.

36. Fleck, N. A. and Liu, D., "Microbuckle initiation from a patch of large amplitude fibre waviness in a composite under compression and bending," *European Journal of Mechanics - A/Solids*, Vol. 20, No. 1, Jan. 2001, pp. 23–37.

37. Liu, D., "Compressive strength of fibre composites with random fibre waviness," *Journal of the Mechanics and Physics of Solids*, Vol. 52, No. 7, July 2004, pp. 1481–1505.

38. Hasanyan, A. and Waas, A. M., "Compressive failure of fiber composites: a homogenized, mesh independent model," *59^{th} AIAA/ASCE/AHS/ASC Structures, Structural Dynamics, and Materials Conference*, Kissimmee, FL, 2018.

39. McGregor, C., Zobeiry, N., Vaziri, R., and Poursartip, A., "A constitutive model for progressive compressive failure of composites," *Journal of Composite Materials*, Vol. 42, No. 25, Dec. 2008, pp. 2687–2716.

40. Pinho, S., Darvizeh, R., Robinson, P., Schuecker, C., and Camanho, P., "Material and structural response of polymer-matrix fibre-reinforced composites," *Journal of Composite Materials*, Vol. 46, No. 19-20, Oct. 2012, pp. 2313–2341.

41. Joseph, A., Davidson, P., and Waas, A. M., "Intra-inter crack band model (I2CBM) for progressive damage and failure analysis of bolted joints," *58th AIAA/ASCE/AHS/ASC Structures, Structural Dynamics, and Materials Conference*, Grapevine, TX, 2017.

42. Joseph, A., Davidson, P., and Waas, A. M., "Failure analysis of composite multi-bolt joints using intra-inter crack band model (I2CBM)," *59th AIAA/ASCE/AHS/ASC Structures, Structural Dynamics, and Materials Conference*, Kissimmee, FL, 2018.

43. Davidson, P., Joseph, A., and Waas, A. M., "Multi scale progressive damage and failure analysis of bolted joints," *59th AIAA/ASCE/AHS/ASC Structures, Structural Dynamics, and Materials Conference*, Kissimmee, FL, 2018.

44. Basu, S., Waas, A. M., and Ambur, D., "A macroscopic model for kink banding instabilities in fiber composites," *Journal of Mechanics of Materials and Structures*, Vol. 1, No. 6, 2006, pp. 979–1000.

45. Schapery, R. A., "A theory of mechanical behavior of elastic media with growing damage and other changes in structure," *Journal of the Mechanics and Physics of Solids*, Vol. 38, No. 2, Jan. 1990, pp. 215–253.

46. Feld, N., Allix, O., Baranger, E., and Guimard, J.-M., "A micromechanics-based mesomodel for unidirectional laminates in compression up to failure," *Journal of Composite Materials*, Vol. 46, No. 23, Nov. 2012, pp. 2893–2909.

47. Davidson, P. and Waas, A. M., "The effects of defects on the compressive response of thick carbon composites: An experimental and computational study," *Composite Structures*, Vol. 176, Sep. 2017, pp. 582–596.

48. Bergan, A. C. and Leone, F. A., "A continuum damage mechanics model to predict kink-band propagation using deformation gradient tensor decomposition," *American Society for Composites 31st Technical Conference*, Williamsburg, Virginia, Sep. 2016.

49. Leone, F. A., "Deformation gradient tensor decomposition for representing matrix cracks in fiber-reinforced materials," *Composites Part A: Applied Science and Manufacturing*, Vol. 76, 2015, pp. 334–341.

50. Gutkin, R. and Pinho, S. T., "Combining damage and friction to model compressive damage growth in fibre-reinforced composites," *Journal of Composite Materials*, Vol. 49, No. 20, Aug. 2015, pp. 2483–2495.

51. Gutkin, R., Costa, S., and Olsson, R., "A physically based model for kink-band growth and longitudinal crushing of composites under 3D stress states accounting for friction," *Composites Science and Technology*, Vol. 135, Oct. 2016, pp. 39–45.

52. Costa, S., Gutkin, R., and Olsson, R., "Mesh objective implementation of a fibre kinking model for damage growth with friction," *Composite Structures*, Vol. 168, 2017, pp. 384–391.

53. Hsu, S. Y., Vogler, T. J., and Kyriakides, S., "On the axial propagation of kink bands in fiber composites : Part II analysis," *International Journal of Solids and Structures*, Vol. 36, No. 4, Feb. 1999, pp. 575–595.

54. Vogler, T. J., Hsu, S. Y., and Kyriakides, S., "On the initiation and growth of kink bands in fiber composites. Part II: Analysis," *International Journal of Solids and Structures*, Vol. 38, 2001, pp. 2653–2682.

55. Vogler, T. J. and Kyriakides, S., "On the initiation and growth of kink bands in fiber composites. Part I: Experiments," *International Journal of Solids and Structures*, Vol. 38, No. 15, 2001, pp. 2639–2651.

56. Yerramalli, C. S. and Waas, A. M., "The effect of fiber diameter on the compressive strength of composites - A 3D finite element based study," *Computer Modeling in Engineering and Sciences*, Vol. 6, No. 1, 2004, pp. 1–16.

57. Gutkin, R., Pinho, S. T., Robinson, P., and Curtis, P. T., "Micro-mechanical modelling of shear-driven fibre compressive failure and of fibre kinking for failure envelope generation in CFRP laminates," *Composites Science and Technology*, Vol. 70, No. 8, Aug. 2010, pp. 1214–1222.

58. Gutkin, R., Pinho, S. T., Robinson, P., and Curtis, P. T., "On the transition from shear-driven fibre compressive failure to fibre kinking in notched CFRP laminates under longitudinal compression," *Composites Science and Technology*, Vol. 70, No. 8, 2010, pp. 1223–1231.

59. Prabhakar, P. and Waas, A. M., "Interaction between kinking and splitting in the compressive failure of unidirectional fiber reinforced laminated composites," *Composite Structures*, Vol. 98, 2013, pp. 85–92.

60. Bai, X., Bessa, M. A., Melro, A. R., Camanho, P. P., Guo, L., and Liu, W. K., "High-fidelity micro-scale modeling of the thermo-visco-plastic behavior of carbon fiber polymer matrix composites," *Composite Structures*, Vol. 134, 2015, pp. 132–141.

61. Bishara, M., Vogler, M., and Rolfes, R., "Revealing complex aspects of compressive failure of polymer composites Part II: Failure interactions in multidirectional laminates and validation," *Composite Structures*, Vol. 169, June 2017, pp. 116–128.

62. Bishara, M., Rolfes, R., and Allix, O., "Revealing complex aspects of compressive failure of polymer composites Part I: Fiber kinking at microscale," *Composite Structures*, Vol. 169, June 2017, pp. 105–115.

63. Naya, F., Herráez, M., Lopes, C. S., González, C., Van der Veen, S., and Pons, F., "Computational micromechanics of fiber kinking in unidirectional FRP under different environmental conditions," *Composites Science and Technology*, Vol. 144, May 2017, pp. 26–35.

64. Leone, F., Bergan, A. C., and Dávila, C. G., "CompDam - Deformation Gradient Decomposition (DGD)," 2018, https://github.com/nasa/CompDam_DGD.

65. Simulia, editor, *Abaqus Analysis User's Guide. Version 6.13*, 2013.

66. Barbero, E. J., *Introduction to Composite Materials Design*, CRC Press, Boca Raton, 2nd ed., 2011.

67. Kowalski, I. M., "Characterizing the tensile stress-strain nonlinearity of polyacrylonitrile-based carbon fibers," *Composite Materials: Testing and Design (Eighth Conference)*, edited by J. Whitcomb, American Society for Testing and Materials, Philadelphia, 1988, pp. 205–216.

68. Wisnom, M. R., "Finite element modeling of shear instability under compression in unidirectional carbon fibre composites," *Journal of Thermoplastic Matrix Composite Materials*, Vol. 7, 1994, pp. 352–363.

69. Bažant, Z. P. and Oh, B. H., "Crack band theory for fracture of concrete," *Matériaux et Construction*, Vol. 16, 1983, pp. 155–177.

70. Laffan, M. J., Pinho, S. T., Robinson, P., Iannucci, L., and McMillan, A. J., "Measurement of the fracture toughness associated with the longitudinal fibre compressive failure mode of laminated composites," *Composites Part A: Applied Science and Manufacturing*, Vol. 43, No. 11, Nov. 2012, pp. 1930–1938.

71. Bergan, A. C. and Garcea, S. C., "In-situ observations of longitudinal compression damage in carbon-epoxy cross-ply laminates using fast Synchrotron radiation computed tomography," *American Society for Composites 32nd Technical Conference*, West Lafayette, Indiana, Oct. 2017.

72. Zobeiry, N., Vaziri, R., and Poursartip, A., "Characterization of strain-softening behavior and failure mechanisms of composites under tension and compression," *Composites Part A: Applied Science and Manufacturing*, Vol. 68, 2015, pp. 29–41.

73. Svensson, D., Alfredsson, K. S., Stigh, U., and Jansson, N. E., "Measurement of cohesive law for kink-band formation in unidirectional composite," *Engineering Fracture Mechanics*, Vol. 151, No. 1960, 2016, pp. 1–10.

74. Jumahat, A., Soutis, C., Jones, F. R., and Hodzic, A., "Fracture mechanisms and failure analysis of carbon fibre/toughened epoxy composites subjected to compressive loading," *Composite Structures*, Vol. 92, No. 2, 2010, pp. 295–305.

75. Pinho, S. T., Robinson, P., and Iannucci, L., "Fracture toughness of the tensile and compressive fibre failure modes in laminated composites," *Composites Science and Technology*, Vol. 66, No. 13, Oct. 2006, pp. 2069–2079.

76. Hapke, J., Gehrig, F., Huber, N., Schulte, K., and Lilleodden, E. T., "Compressive failure of UD-CFRP containing void defects: In situ SEM microanalysis," *Composites Science and Technology*, Vol. 71, No. 9, 2011, pp. 1242–1249.

77. Soutis, C., "Failure of notched CFRP laminates due to fibre microbuckling: A topical review," *Journal of the Mechanical Behavior of Materials*, Vol. 6, No. 4, Jan. 1996.

78. Peterson, M. E. and Murphey, T. W., "High strain flexural characterization of thin CFRP unidirectional composite lamina," *American Society for Composites 31st Technical Conference*, Williamsburg, Virginia, 2016.

79. Marlett, K., Ng, Y., and Tomblin, J., "Hexcel 8552 AS4 unidirectional prepreg at 190 gsm & 35 % RC qualification material property data report," Tech. rep., CAM-RP-2010-002 Rev A, NIAR, 2011.

80. Wanthal, S., Schaefer, J. D., Justusson, B., Hyder, I., Englestad, S., and Rose, C., "Verification and validation process for progressive damage and failure analysis methods in the NASA Advanced Composites Consortium," *American Society for Composites 32nd Technical Conference2*, West Lafayette, Indiana, Oct. 2017.

81. Czabaj, M. W., Riccio, M. L., and Whitacre, W. W., "Numerical reconstruction of graphite/epoxy composite microstructure based on sub-micron resolution X-ray computed tomography," *Composites Science and Technology*, Vol. 105, Dec. 2014, pp. 174–182.

82. Fast, T., Scott, A. E., Bale, H. A., and Cox, B. N., "Topological and Euclidean metrics reveal spatially nonuniform structure in the entanglement of stochastic fiber bundles," *Journal of Materials Science*, Vol. 50, No. 6, March 2015, pp. 2370–2398.

83. Barbero, E. J. and Tomblin, J., "A damage mechanics model for compression strength of composites," *International Journal of Solids and Structures*, Vol. 33, No. 29, Dec. 1996, pp. 4379–4393.

84. Montagnier, O. and Hochard, C., "Compression characterization of high-modulus carbon fibers," *Journal of Composite Materials*, Vol. 39, No. 1, 2005, pp. 35–49.

85. Le Goff, E., Bois, C., and Wargnier, H., "A progressive intra- and inter-laminar damage model to predict the effect of out-of-plane confinement on pin-bearing behaviour of laminated composites," *Journal of Composite Materials*, Vol. 51, No. 4, Feb. 2017, pp. 433–450.

86. Maimí, P., Mayugo, J. A., and Camanho, P. P., "A three-dimensional damage model for transversely isotropic composite laminates," *Journal of Composite Materials*, Vol. 42, No. 25, Dec. 2008, pp. 2717–2745.

87. Lubliner, J., Oliver, J., Oller, S., and Oñate, E., "A plastic-damage model for concrete," *International Journal of Solids and Structures*, Vol. 25, No. 3, 1989, pp. 299–326.

88. Rodríguez, M., Molina-Aldareguía, J. M., González, C., and Llorca, J., "Determination of the mechanical properties of amorphous materials through instrumented nanoindentation," *Acta Materialia*, Vol. 60, No. 9, May 2012, pp. 3953–3964.

89. Canal, L. P., Llorca, J., González, C., and Segurado, J., "Intraply fracture of fiber-reinforced composites: Microscopic mechanisms and modeling," *Composites Science and Technology*, Vol. 72, No. 11, June 2012, pp. 1223–1232.

90. Naya, F., González, C., Lopes, C. S., Van der Veen, S., and Pons, F., "Computational micromechanics of the transverse and shear behavior of unidirectional fiber reinforced polymers including environmental effects," *Composites Part A: Applied Science and Manufacturing*, Vol. 92, Jan. 2017, pp. 146–157.

91. Herráez, M., Mora, D., Naya, F., Lopes, C. S., González, C., and Llorca, J., "Transverse cracking of cross-ply laminates: A computational micromechanics perspective," *Composites Science and Technology*, Vol. 110, Feb. 2015, pp. 196–204.

92. Benzeggagh, M. L. and Kenane, M., "Measurement of mixed-mode delamination fracture toughness of unidirectional glass/epoxy composites with mixed-mode bending apparatus," *Composites Science and Technology*, Vol. 56, No. 4, 1996, pp. 439–446.

93. Herráez, M., *Computational micromechanics models for damage and fracture of fiber-reinforced polymers*, Ph.D. thesis, Universidad Politécnica de Madrid. E.T.S. Caminos, Canales y Puertos, 2018.

94. Loidl, D., Paris, O., Bughammer, M., Riekel, C., and Peterlik, H., "Direct observation of nanocrystallite buckling in carbon fibers under bending load," *Physical Review Letters*, Vol. 95, 2005.

95. López Jiménez, F. and Pellegrino, S., "Failure of carbon fibers at a crease in a fiber-reinforced silicone sheet," *Journal of Applied Mechanics*, Vol. 80, No. 1, 2012, pp. 011020.

96. Oya, N. and Johnson, D. J., "Longitudinal compressive behaviour and microstructure of PAN-based carbon fibres," *Carbon*, Vol. 39, No. 5, April 2001, pp. 635–645.

97. Mujika, F., Carbajal, N., Arrese, A., and Mondragon, I., "Determination of tensile and compressive moduli by flexural tests," *Polymer Testing*, Vol. 25, No. 6, 2006, pp. 766–771.

98. "ASTM Standard D1577. Standard test methods for linear density of textile fibers," *Annual Book of ASTM Standards*, ASTM Int., 2013.

99. Jones, W. R. and Johnson, J. W., "Intrinsic strength and non-hookean behaviour of carbon fibres," *Carbon*, Vol. 9, No. 5, Oct. 1971, pp. 645–655.

100. Allen, S. R., "Tensile recoil measurement of compressive strength for polymeric high performance fibres," *Journal of Materials Science*, Vol. 22, No. 3, March 1987, pp. 853–859.

101. Hawthorne, H. M. and Teghtsoonian, E., "Axial compression fracture in carbon fibres," *Journal of Materials Science*, Vol. 10, No. 1, Jan. 1975, pp. 41–51.

102. DeTeresa, S. J., Porter, R. S., and Farris, R. J., "A model for the compressive buckling of extended chain polymers," *Journal of Materials Science*, Vol. 20, No. 5, May 1985, pp. 1645–1659.

103. Ohsawa, T., Miwa, M., Kawade, M., and Tsushima, E., "Axial compressive strength of carbon fiber," *Journal of Applied Polymer Science*, Vol. 39, No. 8, April 1990, pp. 1733–1743.

104. Miwa, M., Tsushima, E., and Takayasu, J., "Axial compressive strength of carbon fiber with tensile strength distribution," *Journal of Applied Polymer Science*, Vol. 43, No. 8, Oct. 1991, pp. 1467–1474.

105. Macturk, K. S. S., Eby, R. K. K., and Adams, W. W. W., "Characterization of compressive properties of high-performance polymer fibres with a new micro-compression apparatus," *Polymer*, Vol. 32, No. 10, Jan. 1991, pp. 1782–1787.

106. Sinclair, D., "A bending method for measurement of the tensile strength and Young's modulus of glass fibers," *Journal of Applied Physics*, Vol. 21, No. 5, May 1950, pp. 380–386.

107. Rodríguez, M., Molina-Aldareguía, J. M., González, C., and Llorca, J., "A methodology to measure the interface shear strength by means of the fiber push-in test," *Composites Science and Technology*, Vol. 72, No. 15, Oct. 2012, pp. 1924–1932.

108. "ASTM Standard D3518. Standard test method for in-plane shear response of polymer matrix composite materials by tensile test of a $\pm 45^\circ$ laminate," *Annual Book of ASTM Standards*, ASTM Int., 2013.

109. Wind, J. L., Steffensen, S., and Jensen, H. M., "Comparison of a composite model and an individually fiber and matrix discretized model for kink band formation," *International Journal of Non-Linear Mechanics*, Vol. 67, 2014, pp. 319–325.

110. Davidson, P. and Waas, A. M., "Mechanics of kinking in fiber-reinforced composites under compressive loading," *Mathematics and Mechanics of Solids*, Vol. 21, No. May, 2014, pp. 1–18.

111. Lee, J. and Soutis, C., "A study on the compressive strength of thick carbon fibre-epoxy laminates," *Composites Science and Technology*, Vol. 67, No. 10, 2007, pp. 2015–2026.

112. Couque, H., Albertini, C., and Lankford, J., "Failure mechanisms in a unidirectional fibre-reinforced thermoplastic composite under uniaxial, in-plane biaxial and hydrostatically confined compression," *Journal of Materials Science Letters*, Vol. 12, No. 24, 1993, pp. 1953–1957.

113. Liu, Y. and Kumar, S., "Recent progress in fabrication, structure, and properties of carbon fibers," *Polymer Reviews*, Vol. 52, No. 3, July 2012, pp. 234–258.

114. Edie, D. D., Fox, N. K., Barnett, B. C., and Fain, C. C., "Melt-spun noncircular carbon fibers," *Carbon*, Vol. 24, No. 4, Jan. 1986, pp. 477–482.

115. Edie, D. D., Fain, C. C., Robinson, K. E., Harper, A. M., and Rogers, D. K., "Ribbon-shape carbon fibers for thermal management," *Carbon*, Vol. 31, No. 6, Jan. 1993, pp. 941–949.

116. Hunt, M. A., Saito, T., Brown, R. H., Kumbhar, A. S., and Naskar, A. K., "Patterned functional carbon fibers from polyethylene," *Advanced Materials*, Vol. 24, No. 18, May 2012, pp. 2386–2389.

117. Kumar, S., "Gel Spun PAN/CNT based carbon fibers with honey-comb cross-section," Tech. rep., AFRL-OSR-VA-TR-2013-0595, Arlington, VA, 2013.

Appendix A

Compressive strength: Fiber kinking theory

The fiber kinking theory (FKT) was initially proposed by Budiansky in 1983 [3] for an elastic-perfectly plastic composite material under in-plane shear. Later, it was generalized for a non-linear response [4], in particular, deriving the closed-form solution for a Ramberg-Osgood nonlinear shear type (see eq. (5) and incorporated the effect of additional shear loading (τ_{12}). Pinho et al. [17] extended this approach to any non-linear shear response and a 3-D stress state.

FKT is founded on the assumption of an initial, infinitely-wide, fiber misalignment φ_0, consideration for large rotation of the fiber axis, and a nonlinear response when subjected to shear stresses. Under compressive stress, the initially misaligned fiber rotates thereby introducing shear strain. Due to shear nonlinearity, shear stiffness decreases with shear strain, thereby reducing the resistance to rotation of the fiber with increasing compressive stress. When the critical point is reached (the lamina strength), an unstable feedback loop develops resulting in large local rotation of the fibers.

The shear stress in the rotated fiber frame is

$$\tau'_{12} = \frac{\sigma_c}{2}\sin(2\varphi) \tag{A1}$$

where σ_c is the longitudinal compressive stress and φ the sum of an initial misalignment, φ_0, with the rotation due to loading, γ'_{12}

$$\varphi = \varphi_0 + \gamma'_{12} \tag{A2}$$

From the constitutive law, the shear stress-strain relationship is represented as

$$\tau'_{12} = f_{CL}(\gamma'_{12}) \tag{A3}$$

where f_{CL}, in the case of a Ramberg-Osgood expression is the inverse function, $\gamma = (\tau + \alpha\tau^{\eta})/G = f_{CL}^{-1}(\tau)$.

In summary, eq. (A3) represents the material response, while eq. (A1) embodies the load applied. The graphical representation of each term is shown in Fig. A29a, where the black line stands for the constitutive law of the material in shear and the blue line depicts the loading term. For the loading case shown in Fig. A29a, the loading curve intersects the material curve revealing the shear strain in the rotated fiber frame, γ^m. However, as σ_c increases, the slope of the blue curve grows proportionally and eventually it becomes tangent to the black curve, as illustrated in Fig. A29b. At this point, instability is reached and the the material is unable to sustain higher compressive load, $\sigma_c = X_c$. The analytical solution can be analytically expressed as

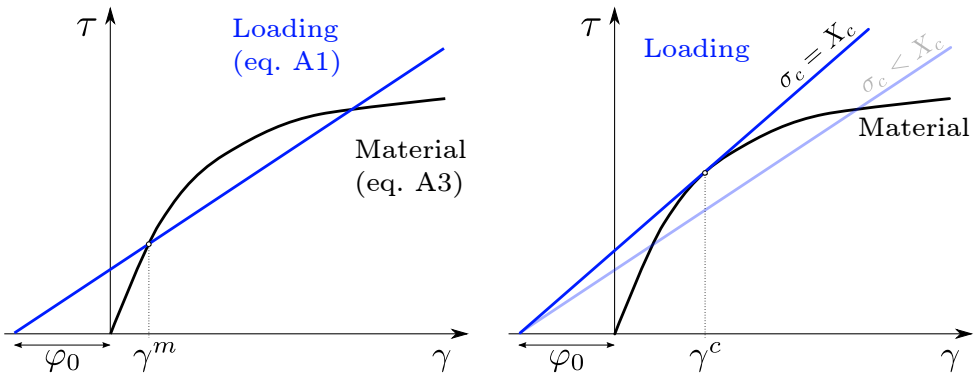

(a) Stable compressive stress loading (b) Instability point, $\sigma_c = X_c$

Figure A29. Shear stress vs. strain curves representing the non-linear material response (eq. A3) and the induced shear stress due to compressive loading (eq. A1). Adapted from Pinho et al. [17].

$$f_{CL}(\gamma^C) = \frac{1}{2} X_c \sin[2(\varphi_0 + \gamma^{\mathrm{C}})] \tag{A4}$$

$$\frac{\partial f_{CL}}{\partial \gamma}\Big|_{\gamma^C} = X_c \cos[2(\varphi_0 + \gamma^{\mathrm{C}})] \tag{A5}$$

where the unknowns are the compressive strength, X_c, and the shear strain to failure, γ^C. See [17] for the extension to handle 3-D states of stress.

Appendix B

Continuum Damage Mechanics model for fiber failure

To consider the fiber failure under longitudinal loading and the nonlinear elastic response in the longitudinal direction, a 3-D continuum damage mechanics model (CDM) was developed. This model is based on the work of Maimí et al. [86] and is implemented as a UMAT in Abaqus/Standard. The material is considered transversely isotropic with a compliance matrix as,

$$\mathbf{S}^f = \begin{bmatrix} \frac{1}{(1-D)E_1^f} & \frac{-\nu_{12}^f}{E_1^f} & \frac{-\nu_{12}^f}{E_1^f} & 0 & 0 & 0 \\ & \frac{1}{(1-D)E_2^f} & \frac{-\nu_{23}^f}{E_2^f} & 0 & 0 & 0 \\ & & \frac{1}{(1-D)E_2^f} & 0 & 0 & 0 \\ & & & \frac{1}{(1-D)G_{12}^f} & 0 & 0 \\ & \text{sym} & & & \frac{1}{(1-D)G_{12}^f} & 0 \\ & & & & & \frac{1}{(1-D)G_{23}^f} \end{bmatrix} \tag{B6}$$

where E_1^f and E_2^f are the longitudinal and transverse elastic moduli respectively, ν_{12}^f and ν_{23}^f are the longitudinal and transverse Poisson ratios, G_{12}^f and G_{23}^f are the longitudinal and transverse shear moduli. Transverse isotropy of the material is verified with $G_{23}^f = E_2^f/2/(1+\nu_{23}^f)$.

Nonlinear elasticity in the longitudinal direction of the fiber is included in the constitutive model including a material parameter, c^f, as shown in Equation (B7).

$$E_1^f = E_1^{0f} \cdot (1 + c^f \cdot \varepsilon_{11}) \tag{B7}$$

where E_1^{0f} is the tangent longitudinal elastic modulus of the fiber when $\varepsilon_{11} \to 0$, and $c^f > 0$ is the nonlinear parameter. These parameters were obtained fitting experimental curves from single-fiber tensile tests. Under uniaxial loading, the expression for the longitudinal stress results from integrating Equation (B7).

$$\sigma_{11}(\varepsilon_{11}) = \int_0^{\varepsilon_{11}} E_1^f(\varepsilon) d\varepsilon = E_1^{0f} \cdot \left(\varepsilon_{11} + \frac{c^f}{2} \cdot \varepsilon_{11}^2 \right) \tag{B8}$$

Care must be taken when selecting the compressive strength of the fiber, X_c^f, as eq. (B8) is a concave quadratic function and its lower bound is $X_c^f > E_1^{0f}/2\ c^f$.

The damage variable, D, lumps longitudinal damage distinguishing between tensile, D_{1+}, and compressive loading, D_{1-}.

$$D = \begin{cases} D_{1+} & ,\ \varepsilon_{11} \geq 0 \\ D_{1-} & ,\ \varepsilon_{11} < 0 \end{cases} \tag{B9}$$

Two damage activation functions are required to represent longitudinal damage under tensile:

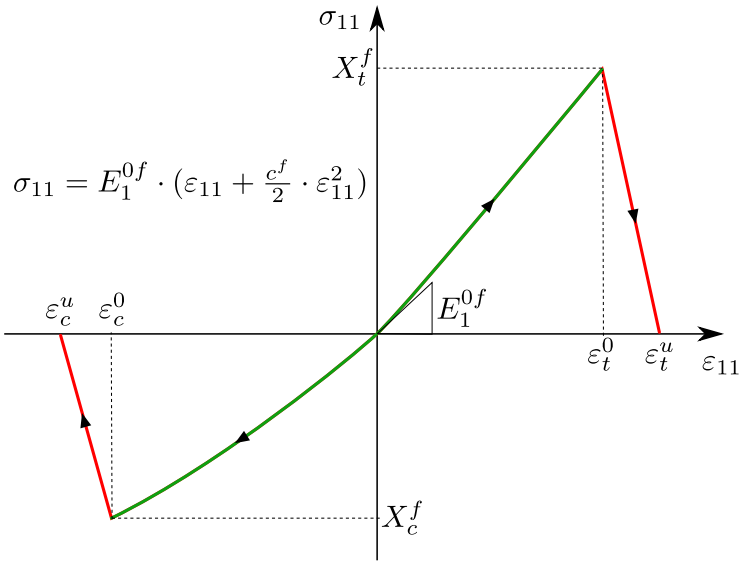

Figure B30. Stress-Strain curve for longitudinal loading of the fiber constitutive model: nonlinear elastic response (green line) until damage onset followed by linear softening (red lines).

$$\begin{aligned} F_{1+} &= \phi_{1+} - r_{1+} \leq 0 \\ F_{1-} &= \phi_{1-} - r_{1-} \leq 0 \end{aligned} \tag{B10}$$

where ϕ_M are the loading functions under longitudinal tension ($M = 1+$) and compression ($M = 1-$), and r_M are the elastic domain thresholds, initially they are set to 1 (undamaged) and increase with damage. A maximum stress criterion governs damage initiation either in tension or compression as:

$$\begin{aligned} \phi_{1+} &= \frac{\tilde{\sigma}_{11}}{X_t^f} \\ \phi_{1-} &= -\frac{\tilde{\sigma}_{11}}{X_c^f} \end{aligned} \tag{B11}$$

The evolution of the elastic domain thresholds, r_M, is expressed by the Kuhn-Tucker conditions preventing damage healing of the material.

$$\dot{r}_M \geq 0;\ F_M \leq 0;\ \dot{r}_M F_M = 0 \tag{B12}$$

This conditions are guaranteed updating the thresholds as,

$$\begin{aligned} r_{1+}^i &= \max(r_{1+}^{i-1},\ r_{1-}^{i-1},\ \phi_{1+}) \\ r_{1-}^i &= \max(r_{1-}^{i-1},\ \phi_{1-}) \end{aligned} \tag{B13}$$

where i represents the current increment and $i-1$ is the previous increment.

The damage evolution laws are defined to implement linear strain softening either under tensile or compressive loads.

$$\begin{aligned} \bar{\varepsilon}_M &= r_M \frac{X_M^f}{E_1} \\ D_M &= \frac{\varepsilon_M^u \cdot (\bar{\varepsilon}_M - \varepsilon_M^0)}{\bar{\varepsilon}_M \cdot (\varepsilon_M^u - \varepsilon_M^0)} \end{aligned} \tag{B14}$$

where $\bar{\varepsilon}_M$ is the equivalent longitudinal strain for tension ($M = 1+$) or compression ($M = 1-$), ε_M^u is the ultimate strain, ε_M^0 is the strain at damage initiation for tension or compression.

Mesh objectivity is achieved through a crack band regularization by selecting the ε_M^u as a function of the element size, l_e, following Bažant's scheme [69] as,

$$\varepsilon_M^u = \frac{2G_M}{X_M \cdot l_e} \tag{B15}$$

where G_M is the fracture energy in longitudinal tension or compression, X_M is the tensile or compressive strength and l_e is the characteristic length of the element.

The convergence of the solving algorithm requires the computation of the material tangent constitutive tensor, $\mathbf{C}_T$, as:

$$\mathbf{C}_T = \mathbf{H}^{-1} : (\mathbf{I} - \mathbf{M}) \tag{B16}$$

where $\mathbf{H}$ is the compliance constitutive tensor, $\mathbf{I}$ is the identity tensor and the tensor $\mathbf{M}$ is:

$$\mathbf{M} = \frac{1}{(1-D)^2} \frac{\partial D}{\partial \varepsilon_{11}} \begin{bmatrix} \frac{\sigma_{11}}{E_1^f} & 0 & 0 & 0 & 0 & 0 \\ \frac{\sigma_{22}}{E_2^f} & 0 & 0 & 0 & 0 & 0 \\ \frac{\sigma_{33}}{E_2^f} & 0 & 0 & 0 & 0 & 0 \\ \frac{\tau_{12}}{G_{12}^f} & 0 & 0 & 0 & 0 & 0 \\ \frac{\tau_{13}}{G_{12}^f} & 0 & 0 & 0 & 0 & 0 \\ \frac{\tau_{23}}{G_{23}^f} & 0 & 0 & 0 & 0 & 0 \end{bmatrix} \tag{B17}$$

where the damage variable derivative is,

$$\frac{\partial D}{\partial \varepsilon_{11}} = \frac{\varepsilon_M^u \cdot \varepsilon_M^0}{\bar{\varepsilon}_M^2 \cdot (\varepsilon_M^u - \varepsilon_M^0)} \tag{B18}$$

The integration of the constitutive model is equivalent to the algorithm presented by Maimí et al. [86]:

1. Read the strain and the strain increment tensors. $\varepsilon^i,\ \Delta\varepsilon^i$
2. Compute the effective stress tensor. $\tilde{\sigma}^i = \mathbf{H}_0^{-1} : \varepsilon^i$
3. Compute the loading functions. $\phi_M^i(\tilde{\sigma}^i)$
4. Compute the threshold values. $r_M^i(r_M^{i-1}, \phi_M^i)$
5. Compute the damage variables. $D_M^i(r_M^i)$

6. Compute the nominal stress tensor. $\sigma^i = (\mathbf{H}^i)^{-1} : (\varepsilon^i + \Delta\varepsilon^i)$

7. Compute the tangent constitutive tensor. $\mathbf{C}_T^i = (\mathbf{H}^i)^{-1} : (\mathbf{I} - \mathbf{M}^i)$

REPORT DOCUMENTATION PAGE

Form Approved
OMB No. 0704–0188

1. REPORT DATE *(DD-MM-YYYY)*	2. REPORT TYPE	3. DATES COVERED *(From - To)*
01-10-2018	Technical Publication	

4. TITLE AND SUBTITLE

Modeling Fiber Kinking at the Microscale and Mesoscale

5a. CONTRACT NUMBER

5b. GRANT NUMBER

5c. PROGRAM ELEMENT NUMBER

6. AUTHOR(S)
M. Herráez and A.C. Bergan

5d. PROJECT NUMBER

5e. TASK NUMBER

5f. WORK UNIT NUMBER
826611.04.07.01

7. PERFORMING ORGANIZATION NAME(S) AND ADDRESS(ES)
NASA Langley Research Center
Hampton, Virginia 23681-2199

8. PERFORMING ORGANIZATION REPORT NUMBER
L–20964

9. SPONSORING/MONITORING AGENCY NAME(S) AND ADDRESS(ES)
National Aeronautics and Space Administration
Washington, DC 20546-0001

10. SPONSOR/MONITOR'S ACRONYM(S)
NASA

11. SPONSOR/MONITOR'S REPORT NUMBER(S)
NASA/TP–2018–220105

12. DISTRIBUTION/AVAILABILITY STATEMENT
Unclassified-Unlimited
Subject Category 24
Availability: NASA STI Program (757) 864-9658

13. SUPPLEMENTARY NOTES
An electronic version can be found at http://ntrs.nasa.gov.

14. ABSTRACT

A computational micromechanics (CMM) model is employed to interrogate the assumptions of a recently developed mesoscale Continuum Damage Mechanics (CDM)model for fiber kinking. The CMM model considers an individually discretized three dimensional fiber and surrounding matrix accounting for nonlinearity in the fiber, matrix plasticity, fiber/matrix interface debonding, and geometric nonlinearity. Key parameters of the CMM model were measured through experiments. In particular, a novel experimental technique to characterize the in situ longitudinal compressive strength of carbon fibers through indentation of micropillars is presented. The CDM model is formulated on the basis of Budiansky's fiber kinking theory (FKT) with a constitutive deformation-decomposition approach to alleviate mesh size sensitivity. In contrast to conventional mesoscale CDM models that prescribe a constitutive response directly, the response of the proposed model is an outcome of material nonlinearity and large rotations of the fiber direction following FKT. Comparison of the predictions from the CMM and CDM models shows remarkable correlation in strength, post-peak residual stress, and fiber rotation, with less than 10% difference between the two models in most cases. Additional comparisons are made with several fiber kinking models proposed in the literature to highlight the efficacy of the two models. Finally, the CMM model is exercised in parametric studies to explore opportunities to improve the longitudinal compression strength of a ply through the use of nonconventional microstructures.

15. SUBJECT TERMS

Fiber kinking; compression; continuum damage mechanics; kink band; micromechanics

16. SECURITY CLASSIFICATION OF:			17. LIMITATION OF ABSTRACT	18. NUMBER OF PAGES	19a. NAME OF RESPONSIBLE PERSON
a. REPORT	b. ABSTRACT	c. THIS PAGE			STI Information Desk (help@sti.nasa.gov)
U	U	U	UU	85	19b. TELEPHONE NUMBER *(Include area code)* (757) 864-9658